ESTABLISHMENT OF ANALYTICAL METHOD FOR SPATIOTEMPORAL METABOLOMIC DYNAMICS AND ITS APPLICATION TO DISEASE MODELS

入江, 美穂

https://doi.org/10.15017/1441323

出版情報：九州大学, 2013, 博士（農学）, 課程博士
バージョン：

ESTABLISHMENT OF ANALYTICAL METHOD FOR SPATIOTEMPORAL METABOLOMIC DYNAMICS AND ITS APPLICATION TO DISEASE MODELS

Miho Irie

Kyushu University

2014

ACKNOWLEDGEMENTS

I would like to express my deep sense of gratitude and appreciation to my research supervisor, Professor Hiroyuki Wariishi for his guidance, support, advice, encouragement and patience during my period of study and providing me the great opportunity to participate in an exciting research on metabolomics. I am deeply indebted to Assistant Professor Hirofumi Ichinose, Assistant Professor Daisuke Miura, and Assistant Professor Yoshinori Fujimura for their support and advices.

I also wish to express my special thanks to all members in the Metabolic Architecture Design Laboratory and Innovation Center for Medical Redox Navigation who have provided a wonderful research environment and have helped with their advices on many occasions.

To mom and dad who inspired me to get PhD. Deeply thanks to sister for your supports, love and believing in me.

DEDICATION

TO MY BELOVED MOM AND DAD.

ABBREVIATIONS

2', 3'-Cyclic GMP	Guanosine-2', 3'-cyclic monophosphate
2PG	2-Phosphoglycerate
3PG	3-Phosphoglycerate
5MeTHF	5-Methyl tetrahydrofolate
6PG	6-Phosphoglycerate
9-AA	9-Aminoacridine
ADP	Adenosine diphosphate
ADP-ribose	Adenosine diphosphate ribose
AICAR	5-Aminoimidazole-4-carboxamide ribonucleotide
AKI	Acute kidney injury
AMP	Adenosine monophosphate
Arg	Arginine
Asn	Asparagine
Asp	Aspartate
ATP	Adenosine triphosphate
BHBA	3-Hydroxybutyrate
BUN	Blood urea nitrogen
CDP	Cytidine diphosphate
CDP-choline	Cytidine diphosphocholine
Cisplatin	*cis*-Diamminedichloroplatinum (II)

CMP	Cytidine monophosphate
CMP-Neu5Ac	Cytidine monophosphate-*N*-acetylneuraminate
Con.	Contralateral
CPu	Corpus striatum
Creatine-P	Phosphocreatine
CTP	Cytidine triphosphate
CTX	Cortex
Cys	Cysteine
dAMP	Deoxyadenosine monophosphate
dCDP	Deoxycytidine diphosphate
dCMP	Deoxycytidine monophosphate
dCTP	Deoxycytidine triphosphate
dGDP	Deoxyguanosine diphosphate
dGMP	Deoxyguanosine monophosphate
DNA	Deoxyribonucleic acid
dTDP	Thymidine diphosphate
dUDP	Deoxyuridine diphosphate
dUMP	Deoxyuridine monophosphate
F16P	Fructose-bisphosphate
F6P	Fructose 6-phosphate
FAD	Flavin adenine dinucleotide
FAICAR	5-Formamidoimidazole-4-carboxamide ribotide
G1P	Glucose 1-phosphate

G6P	Glucose 6-phosphate
GC	Gas chromatography
GDP	Guanosine diphosphate
GlcNAc	*N*-Acetylglucosamine
Gln	Glutamine
Glu	Glutamate
Glycerol-3P	Glycerol 3-phosphate
GMP	Guanosine monophosphate
GPC	Glycero phosphoryl choline
GSH	Glutahione, reduced
GSSG	Glutathione, oxidized
HI	Hippocampus
HILIC	Hydrophilic interaction chromatography
His	Histidine
IMP	Inosine monophosphate
Isc.	Ischemic
IT	Ion trap
L-DOPA	3-(3, 4-Dihydroxyphenyl)-L-alanine
L-Saccharopine	*N*6-(L-1,3-Dicarboxypropyl)-L-lysine
LC	Liquid chromatography
Leu / Ile	Leucine / Isoleucine
Lys	Lysine
m/z	Mass to charge ratio

MALDI-TOF	Matrix-assisted laser desorption and ionization time of flight
MCA	Middle cerebral artery
MCAO	MCA occlusion
Met	Methionine
MS	Mass spectrometry
MS/MS	Tandem mass spectrometer
MSI	MS imaging
MTA	5-Methylthioadenosine
NAA	*N*-Acetyl aspartate
NAAG	*N*-Acetylaspartylglutamate
NAD^+	Nicotinamide adenine dinucleotide
NADH	Nicotinamide adenine dinucleotide
$NADP^+$	Nicotinamide adenine dinucleotide phosphate
NADPH	Nicotinamide adenine dinucleotide phosphate
NAG	*N*-Acetylglutamate
Neu5Ac	*N*-Acetylneuraminate
NO	Nitric oxide
PARG	Poly ADP-ribose glycohydrolase
PARP	Poly ADP-ribose polymerase
PCA	Principal component analysis
PE	Phosphoethanolamine
PEP	Phosphoenolpyruvate

PFPP	Pentafluorophenyl propyl
Phe	Phenylalanine
PLA	Phenyllactate
Pro	Proline
PRPP	Phosphoribosyl pyrophosphate
PYR	Pyruvate
Q	Quadrupole
QIT	Quadrupole ion trap
R5P	Ribose 5-phosphate
ribose-5P	Ribose 5-phosphate
Ribu5P	Riburose 5-phosphate
ROS	Reactive oxygen species
S7P	Sedoheptulose 7-phosphate
SAH	*S*-Adenosyl-L-homocysteine
SAM	*S*-Adenosylmethionine
Ser	Serine
TCA cycle	Tricarboxylate cycle
Thr	Threonine
TOF	Time-of-flight
Trp	Tryptophan
Tyr	Tyrosine
UDP	Uridine diphosphate
UDP-GlcNAc	Uridine diphosphate *N*-acetylglucosamine

UDP-glucose	Uridine diphosphate glucose
UMP	Uridine monophosphate
UTP	Uridine triphosphate
Val	Valine
X5P	Xylulose 5-phosphate
XMP	Xanthosine monophosphate

TABLE OF CONTENTS

Acknowledgements **I**

Dedication **II**

Abbreviations **III**

Table of Contents **IX**

List of Table **XIII**

List of Figure **XIV**

Chapter 1

Introduction 1

1.1 Metabolomics 2

1.1.2 Sample preparation 7

1.1.2.1 Clamping 7

1.1.2.2 Homogenization and Extraction 8

1.1.3 Analytical technologies 9

1.1.3.1 GC-MS 10

1.1.3.2 LC-MS 12

1.1.4 Data analysis 16

1.1.5 Concluding Remarks 18

1.2 Mass spectrometry imaging 19

1.2.1 Matrix assisted laser desorption ionization (MALDI)-MS 21

1.2.2 Sample preparation 23

1.2.2.1 Matrix selection and deposition 23

1.2.2.2 Data acquisition and analysis 25

1.2.3 Concluding Remarks 26

1.3 The aim of this study 29

Chapter 2

Integrated MALDI-MS imaging and LC–MS techniques for visualizing spatiotemporal metabolomic dynamics in a rat stroke model 30

2.1 Introduction 31

2.2 Material and Method 34

2.2.1 Materials 34

2.2.2 Analytical condition of LC-MS 34

2.2.3 Animal protocol 35

2.2.4 MSI analysis of brain sections 37

2.2.5 Metabolomic analysis of brain extracts by LC-MS 39

2.2.6 Multivariate statistical analysis 40

2.3 Results and Discussion 41

2.3.1 Construction of LC-MS based standard metabolites library 41

2.3.2 Experimental Flow 42

2.3.3 Global Investigation of Region-Specific Metabolic Dynamics during Infarct Formation 44

2.3.4 Comparison of the Metabolic Variations between the Whole Tissue Region and its Micro-regions in the MCAO Rat Brain after Ischemia-Reperfusion 52

2.3.5 Spatiotemporal Metabolomic Dynamics and Metabolic Pathway analysis by Combing MSI and LC-MS 57

2.4 Concluding Remarks 67

Chapter 3

Metabolic Analysis of Cisplatin-induced Acute Kidney Injury 68

3.1 Introduction 69

3.2 Material and Method 74

3.2.1 Materials 74

3.2.2 Animals and drug treatment 74

3.2.3 Blood urea nitrogen analysis 75

3.2.4 Metabolomic analysis of kidney extracts by LC-MS 75

3.2.5 MSI analysis of kidney sections 77

3.2.6 Statistical analysis 78

3.3 Results 79

3.3.1 Body weight and blood analyses 79

3.3.2 Global investigation of metabolic dynamics during disease formation 79

3.3.3 Spatiotemporal metabolic variance in kidney visualized by MSI 92

3.4 Discussion 96

3.5 Concluding Remarks 102

Chapter 4

Final remarks 103

Reference 106

Appendix 121

Vita 146

LIST OF TABLES

TABLE	PAGE
1-1 Advantages of analyzing the metabolome	4
1-2 Strategies for metabolomic analysis	6
2-1 Mass-to-charge ratio, molecular species and fragments observed on tissue sections.	55
3-1 List of significantly changed putative metabolites in kidney tissue. Fold-change between drug-treated and control group, with their corresponding *p* values.	83
3-2 List of putative metabolites in kidney tissue. Fold-change between drug-treated and control group.	89

LIST OF FIGURES

FIGURE	PAGE
1-1 The flow of the “omics” sciences	3
1-2 Overview of electron impact	11
1-3 Overview of electrospray ionization	13
1-4 Overview of matrix-assisted laser desorption ionization	22
1-5 Summary of spatiotemporal metabolic dynamics	28
2-1 A schematic diagram of the middle cerebral artery occlusion (MCAO) model rat.	36
2-2 A schematic diagram of the sampling areas for the MSI and LC-MS analyses.	38
2-3 Experimental procedures for the LC-MS and MSI analyses.	43

LIST OF FIGURES

FIGURE	PAGE
2-4 The multivariate analysis of cerebral metabolomic changes induced by reperfusion following 1 h MCAO.	45
2-5 The multivariate analysis of cerebral metabolomic changes in contralateral hemisphere induced by reperfusion following 1 h MCAO.	46
2-6 The multivariate analysis of cerebral metabolomic changes in ischemic hemisphere induced by reperfusion following 1 h MCAO.	47
2-7 Heat map visualization of the common metabolites identified in two brain components during ischemia-reperfusion.	48
2-8 Schematic illustrations of the functional regions in the cortex.	51
2-9 A comparison of the average intensity between the whole tissue regions and partial tissue regions.	54
2-10 The integrated MSI and LC-MS techniques allow the visualization of drastic changes in the spatiotemporal metabolite distribution.	58

LIST OF FIGURES

FIGURE	PAGE
2-11 The LC-MS analysis of region-specific metabolomic changes during reperfusion.	60
2-12 The LC-MS analysis of region-specific metabolomic changes during reperfusion.	61
2-13 The LC-MS analysis of region-specific metabolomic changes during reperfusion.	62
2-14 The LC-MS analysis of region-specific metabolomic changes during reperfusion.	64
3-1 Interaction of cisplatin with DNA nucleobases.	70
3-2 Biochemical cell death pathways induced by cisplatin.	72
3-3 Change of BUN and body weight after cisplatin injection.	80

LIST OF FIGURES

FIGURE	PAGE
3-4 The multivariate analysis of kidney metabolomic changes induced by cisplatin administration.	81
3-5 Time-dependent metabolic variance after cisplatin injection	88
3-6 Visualization of spatiotemporal distribution of renal metabolites related to nucleotide metabolism after cisplatin injection by MSI.	93
3-7 Visualization of spatiotemporal distribution of renal metabolites related to amino acid, glycolysis and lipid metabolism after cisplatin injection by MSI.	94
3-8 Integrated LC-MS and MSI technique visualizes drastic changes of spatiotemporal metabolite distribution in mouse kidney after cisplatin injection.	95
3-9 Catalytic activity of poly ADP-ribose polymerase (PARP) and role in DNA damage.	98
3-10 Metabolism of poly ADP-ribose during DNA damage and repair.	99

CHAPTER 1

INTRODUCTION

1.1 Metabolomics

Dramatic technological advances in the biological sciences over the past few years have forged a new era of research including the emerging field of systems biology. Although the understanding of living organisms at the molecular system level is still in its infancy, it is evident that comprehensive investigations of the ‘‘omics cascade’’ with genomics, transcriptomics, proteomics, and metabolomics are important building blocks and will play a central role in this new science (Dettmer et al. 2007) (Fig. 1-1).

Metabonomics has been defined as the “the quantitative measurement of the dynamic multiparametric response of a living system to pathophysiological stimuli or genetic modification” (Nicholson et al. 1999). The study of metabonomics depends on the production of global metabolite profiles that enable diagnostic changes in the concentrations, or proportions, of low-molecular-weight organic metabolites in samples, such as biofluids and organ extracts, to be determined. Such investigations thus generate metabolic phenotypes and, by studying these, it may well be possible to obtain new and unexpected insights into biological processes (e.g., ageing, onset and progression of disease, toxicity, and response to therapy) (Theodoridis et al. 2008). Table 1-1 provides an overview of the advantages of studying the metbolome in comparison to the transcriptome or proteome (Dunn and Ellis 2005).

Metabolites constitute a diverse set of atomic arrangements when compared to the proteome (arrangement of 20 amino acids) and transcriptome (arrangement of four nucleotide bases bonded with sugar and phosphate backbone) and this provides wide variations in

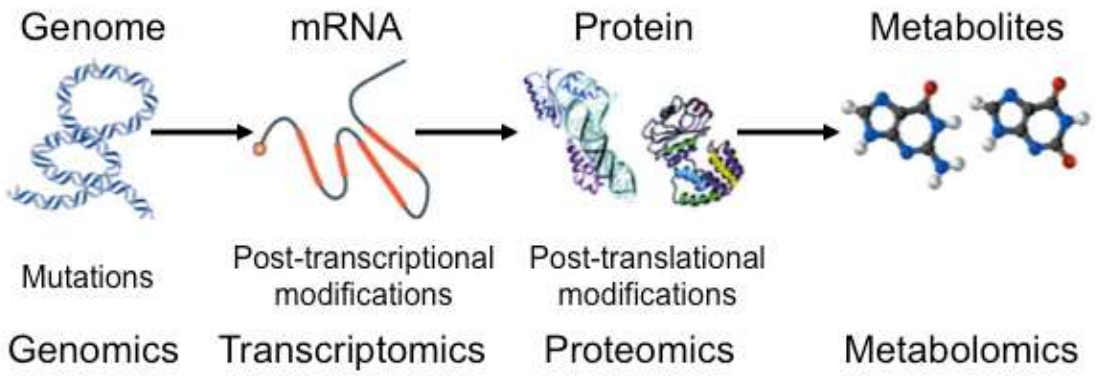

Fig. 1-1 The flow of the "omics" sciences (Patti et al. 2012)**.**

Table 1-1 Advantages of analyzing the metabolome (Theodoridis et al. 2008)**.**

The number of metabolites should be lower than the number of genes and proteins in a cell.
Although the concentration of enzyme and metabolic flux may not significantly change during a biochemical reaction, the concentration of metabolites can significantly change.
The metabolome is the down stream product of gene expression so reflects the functional level of the cell more appropriately and changes in the metabolome are expected to be amplified relative to proteome or transcriptome.
Research is showing that metabolic fluxes are regulated not only by gene expression but also by environmental stresses (phenotype) and hence measurement of the down stream products (metabolites) is appropriate
It is estimated that metabolomics experiments cost two to three times less than proteomic and transcriptomic experiments.

chemical (molecular weight, polarity, solubility) and physical (volatility) properties. The degree of diversity is indicated by the analysis of low molecular weight (MW), polar, volatile organic metabolites, such as ethanol or isoprene to the higher MW, polar (carbohydrates) and non-polar (terpenoids and lipids) metabolites. The metabolome also extends over an estimated 7–9 magnitudes of concentration (pM–mM). In genomics, pleiotropic effects cause seemingly unrelated biochemical pathways to be affected (e.g., by genetic alterations). Therefore, to be able to analyze all metabolites in a single analysis would be preferred (metabolomics). Technologically, this is not currently possible. Therefore, different analytical approaches have been designed in order to answer specific types of questions (Dunn and Ellis 2005). These approaches are defined as Table 1-2 (Ellis et al. 2007; Dettmer et al. 2007; Dunn and Ellis 2005; Dunn, Bailey, et al. 2005).

The most common technologies currently employed for metabolomics are nuclear magnetic resonance (NMR) and mass spectrometry (MS), both of which allow for the phenotyping of a response (Bouhifd et al. 2013). MS-based metabolomics appears the more suitable technology as it allows better deduction of a substance represented by a feature in the recorded spectrum, higher sensitivity and precision compared with NMR, and the ability to measure nearly the whole metabolome. These advances of MS have only been available for a few years (Bouhifd et al. 2013). Therefore, MS-based metabolomics is now being widely used for the study of determination of metabolic biomarkers that change as an indicator of the presence of a disease or in response to drug-based intervention; and, determination of the effect of biochemical or environmental stresses on plants or microbes, which include genetically modified (GM) plants (Ollins and Erhoeyen 2003), bacterial characterizations (Vaidyanathan et al. 2002) and human health assessments (Watkins and German 2002).

Table 1-2 Strategies for metabolomic analysis.

Metabolite target analysis: Qualitative and quantitative analysis of one, or several, metabolites related to a specific metabolic reaction. Extensive sample preparation and separation from other metabolites is required. Metabolite target analysis is mainly used for screening purposes.
Metabolite profiling (metabolic profiling): Identification and quantification of a selective number of predefined metabolites, which are generally related to a specific metabolic pathway. Sample preparation, cleanup and data acquisition can be focused on the chemical properties of these compounds so as to reduce matrix effects. The term metabolic profiling is frequently used in the specific context of drug research in the description of catabolic degradation of an applied chemical.
Metabolomics: The nonbiased identification and quantification of all metabolites in a biological system. Metabolomic approaches must aim at avoiding exclusion of any metabolite by using well conceive sample preparation procedures and analytical techniques.
Metabolic finger printing: Global, high-throughput, rapid analysis to provide sample classification. Also utilized as a screening tool to discriminate between samples from different biological status or origin (e.g., case/control, disease/healthy). Quantification and metabolic identification are generally not employed. Sample preparation is simple.
Metabonomics: Quantitative analysis of metabolites in response to biological perturbation (e.g., disease or therapeutic treatment).

1.1.2 Sample preparation

In the metabolomics experiment, sampling provides a picture or snapshot of the metabolome at one point in time (Dunn and Ellis 2005). When aiming at the simultaneous detection of the full suite of metabolites in biological samples, the applied methods cannot be restricted to the technical question which type of data acquisition might be most suitable but also must seriously consider adequate methods for sample preparation (Fiehn 2002).

1.1.2.1 Clamping

While processing biological samples, special care must be taken to minimize the formation or degradation of metabolites after sampling due to remaining enzymatic activity or oxidation processes. Several techniques have been used to inhibit metabolism such as freezing in liquid nitrogen, freeze clamping, acid treatment or quenching in salt containing aqueous methanol at low temperatures (Theobald et al. 1993; Maharjan and Ferenci 2003; Dettmer et al. 2007). However, acidic treatments pose severe problems for many analytical methods that follow. Usually, freezing in liquid nitrogen is regarded as the best way to stop enzymatic activity, but if this treatment is used, great care must be taken not to partially thaw tissues before extracting metabolites. This issue can be circumvented using lyophilization (which prevents both enzyme and transporter function), or by immediately adding organic solvents and applying heat, thereby also inhibiting the recovery of enzymatic activity (Fiehn 2001). Tissues

cultures are often directly infused into cold organic solvents, keeping temperatures below –20°C at all times during sample preparation (Gonzalez et al. 1997; Fiehn 2001).

1.1.2.2 Homogenization and Extraction

Prior to sample extraction, different types of sample homogenization can be used, depending on the number of samples to be treated, and on the type of tissue. Animal tissue can be ground under liquid nitrogen simply using mortar and pestle, or using a ball mill with pre-chilled holders (Fiehn et al. 2000), or together with the extraction solvent by ultraturrax devices (Fiehn 2002).

Polar/non-polar extractions are the most frequently applied method and are performed by physical/chemical disruption of the cells, removal of the cell pellet by centrifugation and distribution of metabolites to polar (methanol/water) and non-polar (chloroform) solvents (Dunn and Ellis 2005).

1.1.3 Analytical method

Metabolomics requires highly analytical instruments because it is dealing with thousands of small molecules with a diversity of a wide range of chemical and physical species, from low molecular weight polar volatiles such as ethanol, to high molecular weight polar glucosides, non-polar lipids and inorganic species. The range of metabolite concentrations can vary over nine orders of magnitude (pM-mM). Therefore, it is the need for the analysis technologies of metabolomics that enable detection of unbiased and wide-dynamic range (sensitive) with the high-throughput, reproducible and accurate.

As an analytical tool, MS is widely employed and standard texts detailing theory and applications are available. In metabolomic applications MS provides both sensitive detection and metabolite identification via mass spectrum interpretation and comparison or molecular formulae determination via accurate mass measurements (Dunn, Bailey, et al. 2005).

As biological samples can be introduced to the ion-source MS either via direct-injection or after chromatographic separation, two major methods, hyphenated method and direct injection method, have been used in MS-based metabolomics. Direct-injection, especially when used on high-resolving MS, provides an effective way to detect and quantify large numbers of metabolites, and was extensively utilized for metabolome analysis (Bouhifd et al. 2013). The major drawback of the direct-injection technique is the presence of matrix effects, which resulted in the failure to detect some metabolite ions with low ionization efficiencies (Bouhifd et al. 2013).

Coupling chromatography to MS offers an excellent solution to complex mixture analyses

and has been extensively used in metabolomics. Chromatographic separation of metabolites prior to MS analyses has several advantages: (1) reduction of matrix effects, (2) separation of isomers, (3) provides additional and orthogonal data (e.g., retention time) valuable for metabolite annotation, and (4) allows for more accurate quantification of individual metabolites. Currently, two predominant chromatographic techniques have been incorporated in MS based metabolomics (Lei et al. 2011).

1.1.3.1 GC-MS

GC combined with electron ionization (EI) MS is ideally suited for the analyses of both volatile and nonvolatile compounds following derivatization. The high resolution and reproducible chromatographic separations offered by modern capillary GC make it an excellent tool for complex metabolic mixture analyses (Lei et al. 2011).

During electro-ionization, analyte molecules are ionized and fragmented in the gas phase (10^{-1} to 10^{-4} Pa) by interaction with 70 eV electrons generated from a hot filament and accelerated through a 70V electric field (Beran and Kevanl 1969). As the fragmentation is reproducible, these fragment ions form the 'chemical fingerprints' ('features') of the analyte. Therefore, many commercially available libraries such as NIST with thousands of standard EI spectra can be used for rapid identification of analytes (Bouhifd et al. 2013). One prerequisite for GC-MS analysis is the need of volatile analytes that are stable at high temperature during the whole analysis. Generally, some non-volatile metabolites (e.g., sugars, amino acids) can be converted into volatile compounds by derivatization (Bouhifd et al. 2013) (Fig. 1-2).

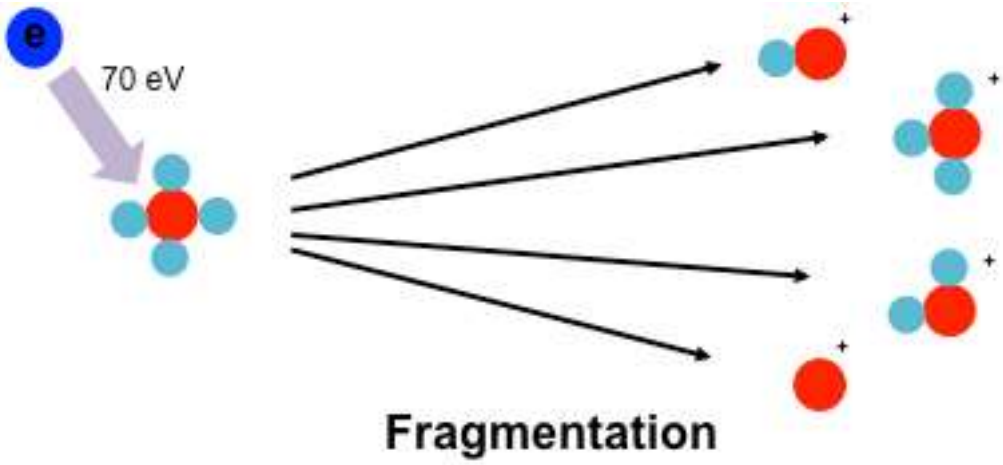

Fig. 1-2 Overview of electron impact

1.1.3.2 LC-MS

Another combined system, LC-MS, provides metabolite separation by LC followed by electrospray ionization (ESI) or, less typically, atmospheric pressure chemical ionization (APCI) (Byrdwell 2001). This technique differs from GC-MS in distinct ways (lower analysis temperatures, and sample volatility not required) and this simplifies sample preparation (Dunn and Ellis 2005).

The ionization technique selected for LC-MS based metabolomics can also have a substantial impact on metabolite profiles. Generally, ESI is ideal for semi polar and polar compounds (Fig. 1-3); whereas APCI is more suitable for neutral or less polar compounds. These two ionization techniques provide complementary data, both desirable in large scale non-targeted metabolomics (Lei et al. 2011). These ion sources perform ionization at atmospheric pressure with subsequent transfer of ions from atmospheric to vacuum pressure (Dunn, Bailey, et al. 2005).

Many modern MS instruments are now capable of fast polarity switching during data acquisition and have been exploited in simultaneous acquisition of both positive and negative ion mode data (Tolonen and Uusitalo 2004; Cai et al. 2010). Use of both positive and negative ionization LC-MS offers more comprehensive metabolome coverage than using a single polarity (Farag et al. 2007; Nordström et al. 2008; Lei et al. 2011). Quantification is performed by external calibration. Metabolite identification is more time intensive. LC-MS does not result in fragmentation of molecular ions as observed in electron impact mass spectrometers, so it does not allow direct metabolite identification by comparison of LC-MS mass spectra, as LC-MS mass spectral libraries are not commonly available (as is the case for

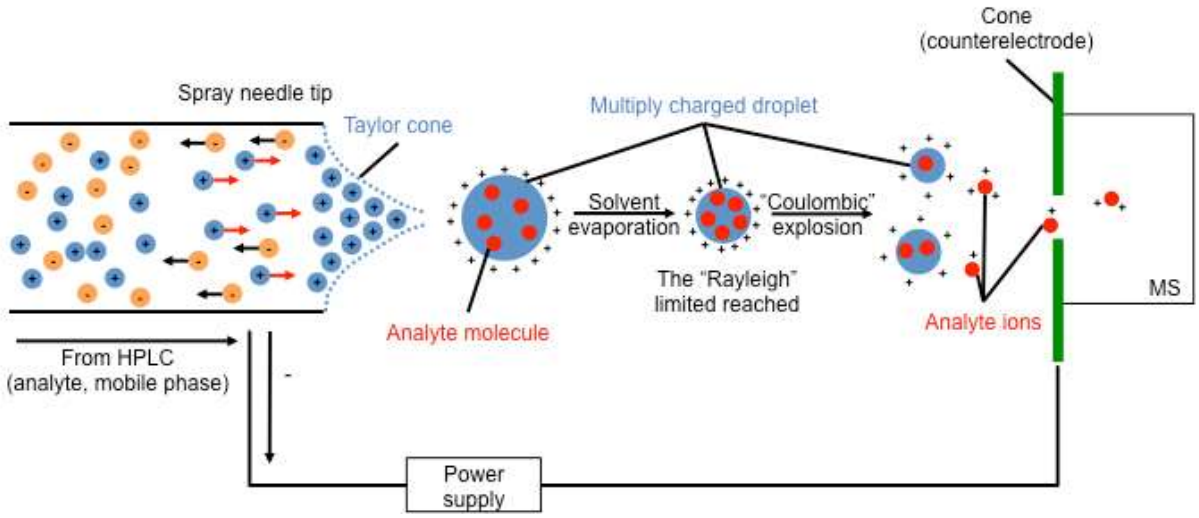

Fig. 1-3 Overview of electrospray ionization

GC-MS). However, with the use of accurate mass measurements and/or tandem MS (MS/MS) to provide collisional induced dissociation (CID) and related mass spectra (MS/MS), metabolite identification can be performed (Lenz et al. 2004) in either quadruple-based tandem in-space instruments (e.g., triple quadrupole (QqQ)), or ion-trap-based tandem in-time instruments (e.g., quadrupole-ion trap time of flight (IT-TOF)) (Dunn and Ellis 2005).

High resolution separations of complex metabolomic samples will provide more descriptive data and can be performed with capillary columns, where in theory, as the column internal diameter and packing particle size decrease the chromatographic resolution will increase. Due to a reduction in band broadening, there will also be a greater S/N ratio, and thus an increase in sensitivity (Dunn, Bailey, et al. 2005).

Column chemistry is also important as most published applications use reversed phase assays with solvents that are compatible with electrospray ionization instrumentation. However, polar metabolites can be eluted in the void volume with little chromatographic retention and therefore separation is not achieved and ionization suppression can be problematic. Different column chemistries are being assessed including hydrophilic interaction liquid chromatography in the study of cucurbita maxima leaves, where oligosaccharides, glycosides, amino sugars, amino acids and sugar nucleotides were all detected (Dunn, Bailey, et al. 2005).

Ion annotation is a procedure to recognize a group of ions likely to originate from the same compound. In LC-MS-based metabolomics, one metabolite is often represented by multiple peaks in LC-MS data with distinct *m/z* values but, at similar retention times, due to the presence of isotopes, adducts and neutral loss fragments. As long as the scan rate of mass spectrometer is properly adjusted and enough scanning points are acquired to define the

chromatographic peaks, the ions from the same compound share similarly shaped elution profiles, which can be represented by their extracted ion chromatograms. Thus, ion annotation can be achieved by clustering similar elution profiles together, thereby facilitating metabolite identification (Xiao et al. 2012).

After grouping peaks together by ion annotation, the monoisotopic exact masses of these compounds can be calculated based on the mass differences of adducts/isotopes from their monoisotopic neutral forms. The calculated masses can be used to search against metabolite databases (e.g., HMDB and Metlin). Metabolites having molecular masses within the pre-specified tolerance of the query masses are retrieved from these databases. However, mass-based identification seldom results in unique identification of these ions (Xiao et al. 2012). By acquiring MS/MS spectra of these ions, the results from mass-based identification can be further refined through the MS/MS spectrum matching using authentic compound or public database (e.g., MassBank). Although recent research into the reproducibility of mass spectral libraries from CID have been undertaken (Bristow et al. 2004), and show that mass spectra produced on different instrument types and different manufacturers' instruments are similar (Dunn and Ellis 2005), it is often affected by experimental factors (e.g., instrument type and collision energy). Therefore, the most reliable way to identify a metabolite unambiguously and confidently is to compare its mass, retention time and fragmentation spectrum with those of authentic standards at each laboratories and instruments.

1.1.4 Data analysis

Raw data are usually stored in sample files as series of mass spectra acquired at a given time point or scans. Each scan is represented by a pair of mass and intensity vectors. The vector length varies from scan to scan depending on the number of detected peaks. However, for a metabolomics data analysis it is necessary to extract information about all compounds, including mass and retention time, as compound identifiers and intensity as quantitative representation of concentration. Moreover, the data should be extracted from all data files as uniform matrices to allow data comparison and discovery of differentially expressed metabolites (Dettmer et al. 2007). When the mass intensity vectors are transformed to uniform length, the entire dataset obtained by direct injection analyses (a single scan) can be represented as a matrix (m (+ s) × f), where m is the length of the uniform mass vector, s is the retention time and f is the number of files (Dettmer et al. 2007).

Next, each sample is usually normalized to remove the unwanted systematic bias in ion intensities between measurements, while retaining the interesting biological variation. Strategies for normalization of metabolic profile data can be divided into two major categories: (1) Statistical models used to derive optimal scaling factors for each sample based on complete dataset (Crawford and Morrison 1968), such as normalization by unit norm (Scholz et al. 2004) or median (Wang et al. 2003) of intensities. (2) Normalization by a single or multiple internal (e.g., added to sample prior to extraction) or external (e.g., added to sample after extraction) standard compounds based on empirical rules, such as specific regions of retention time (Hermansson et al. 2005; Bijlsma et al. 2006; Katajamaa and Oresic

2007).

The statistical tools for metabolomics data analysis should be selected according to the aim of the study. If the aim is sample classification and prior information about the sample identity is unknown (e.g., in identification of silent mutation phenotype in progeny), unsupervised methods such as hierarchical clustering analysis (HCA), or principal component analysis (PCA) are used (Setoyama et al. 2013). On the other hand, sample identity is often known and the aim of the study is to discover characteristic biomarkers (e.g., search for biomarkers of a disease comparing samples from healthy and diseased subjects) (Sugimoto et al. 2010). In this case, supervised methods such as orthogonal partial least squares discriminant analysis (OPLS-DA) can be used as well. The supervised methods use prior information about sample class and perform better in biomarker discovery (Jonsson et al. 2005). The supervised methods are also the preferred option for diagnostics studies, when classes of some samples are known and identities of others need to be determined (e.g., cancer diagnosis by comparing a patient's metabolic fingerprint with the fingerprints of healthy and diseased subjects). However, if the aim of the study is a mere biomarker discovery in samples of known classes, common statistical methods such as Student's t test can be applied in order to find statistically significant differences of metabolite levels between the clusters (Smilde et al. 2005; Dettmer et al. 2007).

1.1.5 Concluding Remarks

Metabolomics use in several research fields is rapidly increasing. Especially coupling chromatography to MS offers an excellent solution to complex mixture analyses and has been extensively used in metabolomics. There are enormous benefits to performing hyphenated-MS based metabolomics on several samples. Molecular analyses provide new insight into biochemical processes that are not attainable by other analysis. Although MS coupled with chromatography techniques such as LC-MS or GC-MS has been known to be a conventionally used strategy for metabolomics (Miura et al. 2012), these methods have a drawback in the analysis of tissue samples because of the requirement of metabolite extraction, which causes the loss of information on the spatial localization of the metabolites. Understanding the complex biochemical processes that occur within living organisms requires not only the elucidation of the molecular entities involved in these processes, but also their spatial distribution within the organism. Analytical technologies for elucidating multiple molecular dynamics in the micro-region that retain the spatial information of the target tissue are thought to be important for understanding biological complexity of disease progress.

1.2 Mass spectrometry imaging

Understanding the complex biochemical processes that occur within living organisms requires not only the elucidation of the molecular entities involved in these processes, but also their spatial distribution within the organism. Analytical technologies for elucidating multiple molecular dynamics in the micro-region that retain the spatial information of the target tissue are thought to be important for understanding biological complexity of disease progress (Miura et al. 2012).

Traditional imaging techniques like positron emission tomography, magnetic resonance imaging, and whole-body radiography share a key advantage in their compatibility with living systems but have limited spatial resolution and require molecular or radioisotope tags that do not distinguish molecular forms having the tag (Dale et al. 2008).

MS based imaging technique such as laser capture microdissection offers the highest regional selectivity and can be used for single cell analyses (Ladanyi et al. 2006; Pinzani et al. 2006). This approach is time consuming and requires a high number of cells in order to detect low abundance molecules. Voxelization and subsequent LC–MS of a mouse brain tissue section have been used for spatial mapping and quantitation of a lot of biomolecules, but at the cost of low spatial resolution (1 mm^3) and extensive sample preparation (Petyuk et al. 2007; Amstalden van Hove et al. 2010). Thus, the simultaneous multiple molecular imaging with high sensitivity and high-throughput will be a technical breakthrough for pathophysiological research.

Matrix-assisted laser desorption/ionization (MALDI)-MS based MS imaging (MSI),

enables the determination of the distribution of biomolecules present in tissue sections by direct ionization and detection at comparatively sensitive and high-resolution (Miura et al. 2010a). This technique can detect various biomolecules simultaneously without any labeling during a single analysis. Therefore, MSI is now being widely used for the in situ imaging of macromolecules, such as proteins, peptides, lipids, metabolites and drugs and is expected to be a potential tool for the pathological analysis of the brain, kidneys or tumors (Walch et al. 2008; Sugiura et al. 2009; Miura et al. 2012).

1.2.1 Matrix assisted laser desorption/ionization (MALDI)-MS

MALDI is a soft ionization technique used in MS, allowing the analysis of biomolecules (biopolymers such as DNA, proteins, peptides and sugars) and large organic molecules (such as polymers, dendrimers and other macromolecules), which tend to be fragile and fragment when ionized by more conventional ionization methods (Fig. 1-4). The mechanism of ion formation in MALDI is a complex phenomenon. The laser is fired at the matrix crystals in the dried-droplet spot. The matrix absorbs the laser energy and it is thought that primarily the matrix is desorbed and ionized (by addition of a proton) by this event. The matrix is then thought to transfer proton to the analyte molecules, thus charging the analyte. Ions observed after this process consist of a neutral molecule [M] and an added or removed ion. Together, they form a quasimolecular ion, for example $[M+H]^+$ in the case of an added proton, $[M+Na]^+$ in the case of an added sodium ion, or $[M-H]^-$ in the case of a removed proton. MALDI is capable of creating singly charged ions, but multiply charged ions ($[M+nH]^{n+}$) can also be created, as a function of the matrix, the laser intensity and/or the voltage used. Note that these are all even-electron species. Ion signals of radical cations (photoionized molecules) can be observed.

Instrument of MSI need capability of the throughput, mass resolving power, mass accuracy, tandem-MS capabilities and spatial resolution. Generally, MALDI-MSI is typically carried out on an instrument with a time of flight (TOF) mass analyzer because speed, sensitivity and broad mass range detection (m/z ~1-100,000) make it attractive for imaging purpose (Amstalden van Hove et al. 2010).

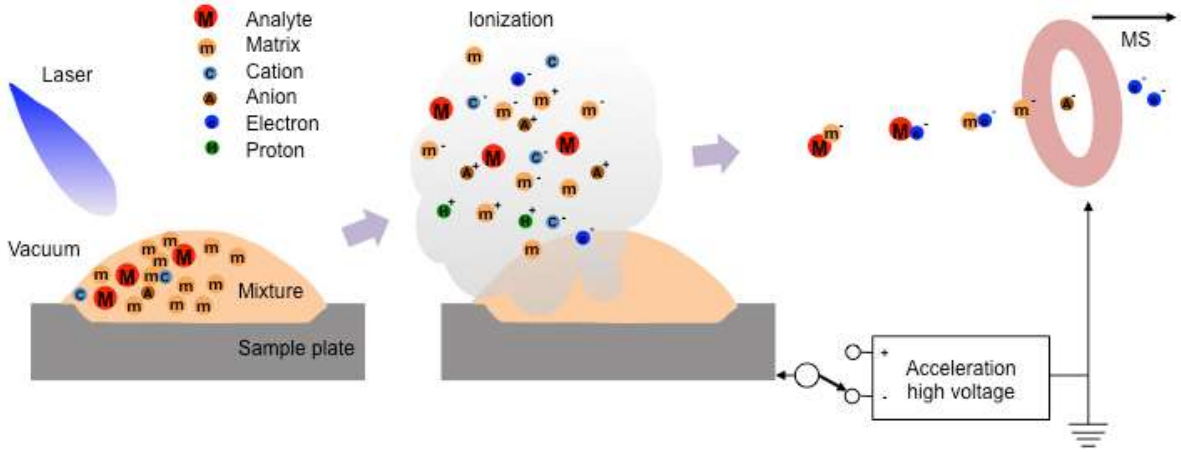

Fig. 1-4 Overview of matrix-assisted laser desorption/ionization

1.2.2 Sample preparation

Several factors for MS imaging sample preparation must be considered, from sample collection to surface treatment prior to analysis. The proper and immediate treatment of tissue after surgical removal is essential to avoid degradation and spatial rearrangement of molecules (Schwartz et al. 2003; Amstalden van Hove et al. 2010).

Thin, flat surfaces are required for MS imaging analysis. Samples are typical prepared by cryo-sectioning on a microtome. The sectioned tissue slice can be directly applied on a conductive surface (e.g., indium tin oxide (ITO)-coated glass slide), for full tissue imaging (Amstalden van Hove et al. 2010).

1.2.2.1 Matrix selection and deposition

Matrix selection and deposition is crucial step in the sample preparation protocol for MSI. It is clear that the molecules detected depend critically on the chemistry of the matrix used and its dispersion on the sample to be analyzed (Vickerman 2011). Moreover, the matrix must not react with the analytes in the tissue section and should posses a low sublimation rate because most MSI are conducted under high vacuum conditions. In addition, the type and molecular weight of the analytes of interest must be considered when choosing a MALDI matrix (Amstalden van Hove et al. 2010). Thus detection of proteins requires sinapinic acid, whereas lipids may be detected using either 2, 5-dihydrobenzoic acid or

a-cyano-4-hydroxycinnamic acid (Vickerman 2011). In addition, 9-aminoacridine is suited to detect smaller endogenous metabolites.

Matrix deposition must be homogeneous, reproducible, provide sufficient sensitivity and should be easy to use (Amstalden van Hove et al. 2010). In addition, the spatial resolution attainable is particularly critically dependent on the dispersion and particle size of the matrix crystallites (Vickerman 2011). The environmental conditions (e.g., humidity, temperature) during matrix deposition are important, since they may result in poor interaction between matrix and analytes (Amstalden van Hove et al. 2010). The methods for matrix deposition methods for MSI are briefly described below.

Direct-droplet method: The matrix solution is applied on the sample manually with a pipette. The droplet of matrix solution diffuse on the tissue surface and results in the nonuniform matrix crystals that form in the droplet area (Amstalden van Hove et al. 2010).

Pneumatic nebulization: The matrix solution is sprayed onto the sample with a hand-held airbrush (Schwartz et al. 2003). A gentle spray allows the formation of a homogeneous crystal layer on the sample surface. This technique can form very tiny matrix crystals on the surface, but the intensity of the signals is not satisfactory compared to the droplet method. Moreover, the spray has to be optimized previous to each application, thus reproducibility may be an issue (Amstalden van Hove et al. 2010).

Matrix sublimation: Solid matrix is placed on the bottom section of a condenser and the sample is attached to the condenser with double sided thermally conductive tape facing the solid matrix. The sublimation occurs under low pressure and high temperature which allows the matrix to condense on the cold sample surface (Amstalden van Hove et al. 2010). This method provides enhanced purity of matrix applied to the sample, small crystal size, and

uniformity of deposition (Hankin et al. 2007). This method is suited to detect lipids.

1.2.2.2 Data acquisition and analysis

To generate an image, matrix is applied over the entire tissue section, and mass spectra are acquired across the entire tissue section in an ordered array. Generally, spatial resolution ranges from 10 to 100 μm. With currently available lasers, images can be generated in minutes to hours, depending on the sampler size and spatial resolution. Each individual spot has an associated mass spectrum that is analogous to a pixel in a digital image. One can generate an average spectrum from the entire tissue section to aid in the generation of MS images. Each peak from the average spectrum can be displayed as a function of location and relative intensity across the tissue section (Seeley and Caprioli 2011).

1.2.3 Concluding Remarks

Recent developments, from instrumentation to sample preparation, have improved the sensitivity and spatial resolution for MSI. There are enormous benefits to performing MSI on tissue samples. Molecular analyses provide new insight into biochemical processes that are not attainable by other analysis. The application of this technique and metabolic pathway analysis to a rat transient middle cerebral artery occlusion (MCAO) model visualized a spatiotemporal behavior of metabolites in the central metabolic pathway regulated by an ischemia-reperfusion (Miura et al. 2010a). Hattori et al. have also reported spatiotemporal changes in energy charge, adenylates, and NADH during focal ischemia in a mouse MCAO model (Hattori et al. 2010). These findings highlight the potential applications of the in situ metabolomic imaging technique to visualize spatiotemporal dynamics of the tissue metabolome, which will facilitate biological discovery in both preclinical and clinical settings (Miura et al. 2012).

However, some limitations remain to overcome before the broad range of endogenous metabolite imaging can be achieved. As mentioned above, it is generally known that, in MALDI, the detection of molecules is completely dependent on the matrix. Moreover, Matrix effects (otherwise referred to as ionization suppression or enhancement) should be assessed when analyzing complex biological samples without chromatographic separation. The sensitivity and accuracy of quantification between samples of differing matrix composition (including differences between matrices and sample) can be compromised, which means this is a screening and not a quantitative tool. Detectable metabolites by single MSI analysis are a

few than standard metabolomics protocols such as LC-MS. Therefore, the combination of MSI and standard bioanalytical protocols is needed to understand detailed biological phenomenon. This combination will allow confident identification of biologically relevant compounds and their localization in tissues (Fig. 1-5).

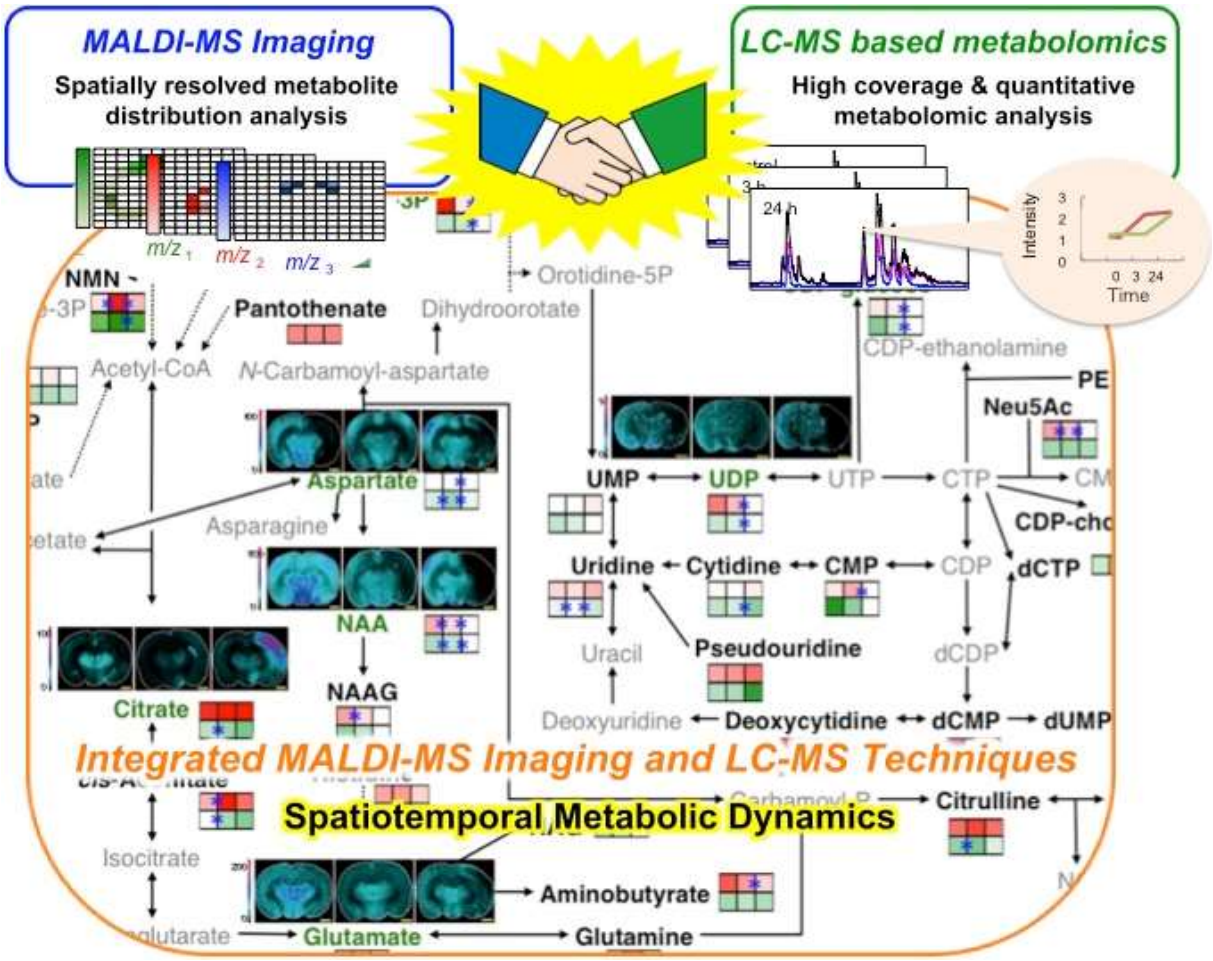

Fig. 1-5 Summary of spatiotemporal metabolic dynamics

1.3 The aim of this study

In the case of tissue analysis, metabolomics requires not only comprehensive and quantitative but also information of metabolite distributions in the tissue (Fig. 1-5). In the present study, 1) the author developed elucidation technique of detailed metabolic valiance each micro-region using combination of LC-MS-based metabolomics data, which is high comprehensive and quantitative analysis, and MSI data, which is able to visualize metabolites distribution in the tissue. Firstly, to exploit above technique, LC-MS based authentic standard library for comprehensive and high-throughput analysis was constructed. Moreover, the author applied combination technique to MCAO rat brain during infarct formation. To validate MSI data, metabolites extracted from not whole brain but 3 each region (cortex, hippocampus and corpus striatum) at LC-MS analysis, and the author compared metabolite variation in MCAO brain during infarct formation between MSI and LC-MS data. Next, 2) the author performed elucidation of metabolic variance from onset to becoming serious using above technique in cisplatin-induced acute kidney injury, at which metabolite extraction is difficult from each region.

CHAPTER 2

Integrated MALDI-MS imaging and LC–MS techniques for visualizing spatiotemporal metabolomic dynamics in a rat stroke model

2.1 Introduction

Stroke is the third major cause of death in the major industrialized countries, and is a brain disease associated with cell death due to a decrease in oxygen and glucose resulting from a lack of blood flow (ischemia) (Green 2008). The symptoms of this disease are caused by both blood flow blockage-induced occlusion injury and oxidative stress-induced reperfusion injury (Martin 2003; Memezawa et al. 1992). To date, several therapeutic agents, including edaravone, have been developed to lessen the ischemia-induced damage. However, the efficacy of such agents was limited for treating acute ischemic stroke patients, because of the limited time window (~3 h after ischemia) (Zhang et al. 2005). Therefore, the development of drugs with a longer or later time window or that function via other mechanisms is necessary.

Previous research addressing the mechanisms of disease, including stroke, have been targeted to particular genes, proteins and metabolites, and the analysis of only a part of the functions related to these biomolecules has been the focus of most investigations (Phillis et al. 1996, 1994). However, the data obtained from such studies is insufficient to understand the complex disease processes using conventional techniques alone, because various other, untargeted, biomolecules may participate in the pathological progress (Jung et al. 2011). Behaviors of biomolecules are drastically altered by the time elapsed from disease onset, and there are often local differences within the lesion site (Matsumoto et al. 1993). Therefore, to obtain a precise understanding of the biological complexity of disease progression, it is necessary to obtain more comprehensive and spatiotemporal information about the biomolecules in the target site.

Recently, “omics” technology, the analysis of comprehensive biomolecules, has received considerable attention. In particular, metabolomics, the analysis of comprehensive metabolites as a compound-level phenotype of genomic information, can elucidate the biological phenomena unresolved by transcriptomics and proteomics (Griffin and Shockcor 2004; Holmes et al. 2008; Nicholson et al. 1999). Generally, MS coupled with pre-separation techniques such as liquid chromatography (LC)-MS or gas chromatography (GC)-MS, has been used for the metabolomic studies due to their high coverage (more than several hundred metabolites) and ability to provide quantification (Dunn and Ellis 2005; Werner et al. 2008; Pohjanen et al. 2007). However, these methods have a drawback in the analysis of tissue samples because of the requirements for metabolite extraction, which causes the loss of information regarding the spatial localization of the metabolites. Visualization of the in situ interactions among a broad range of metabolites and their dynamic changes with information about their localization is indispensable for accurately understanding complex biological processes. In the pathological analysis of tissues with many functional compartments, such as the brain, it is necessary to not only determine the comprehensive metabolites involved in these processes, but also to visualize their spatial distribution within the tissue.

A remarkable new technology, MS imaging (MSI), enables the determination of the distribution of biomolecules present in tissue sections by direct ionization and detection (Caprioli et al. 1997; Miura et al. 2012). This technique can detect various biomolecules simultaneously without any labeling during a single analysis. Therefore, MSI is now being widely used for the in situ imaging of relatively abundant macromolecules, such as proteins, peptides and lipids, and is expected to be a potential tool for the pathological analysis of the brain, kidneys or tumors (Stoeckli et al. 2001; Amstalden van Hove et al. 2010; Vickerman

2011).

We recently succeeded in simultaneously visualizing more than 30 metabolites in normal mouse brain tissue by using matrix-assisted laser desorption/ionization-time of flight (MALDI-TOF)-MSI (Miura et al. 2010a). Moreover, the application of this technique and metabolic pathway analysis to a rat transient middle cerebral artery (MCA) occlusion (MCAO) model allowed for partially visualizing the spatiotemporal behavior of metabolites in the central metabolic pathway regulated by the ischemia-reperfusion insult (Miura et al. 2010a). This MSI technique is expected to be useful as an innovative multi-molecular imaging technique for high-precision pathological evaluation (Kinross et al. 2011). Therefore, an additional understanding of the dynamics of more comprehensive metabolites detected by LC-MS, which cannot be detected by MSI, may lead to further elucidation of the complex pathological mechanisms underlying various diseases.

In the present study, the author performed LC-MS analysis of metabolites extracted from MCAO rat brain, and these data were co-analyzed with our previous and newly added MSI data (Miura et al. 2010a) to investigate the detailed metabolic dynamics during pathological progression. This approach could trace the diverse spatiotemporal metabolic behavior and visualize significant metabolic change in response to disease progression in the rat brain in a model of MCAO during infarct formation after ischemia-reperfusion.

2.2 Materials and methods

2.2.1 Materials

Internal standard compounds sulfanilamide, methionine sulfone, 4-aminoantipyrine, 2-hydroxyundecanate and 4-hydroxybenzophenone purchased from Sigma-Aldrich. Acetonitrile, ethanol, methanol, 2-propanol, dimethylsulfoxide ammonium formate, formic acid and chloroform were purchased from Wako Pure Chemical Industries, Ltd. A part of metabolite standards (215 species) were kindly supplied from Mitsubishi Tanabe Pharma Corporation. Indium tin oxide (ITO)-coated slide glass and 9-aminoacridine (9-AA) hydrochloride were obtained from Sigma-Aldrich (St Louis, MO, USA). The 9-AA was recrystallized prior to use. The organic solvents, internal standards and metabolite standards used in this study were purchased from Wako Pure Chemical Industries, Ltd (Osaka, Japan).

2.2.2 Analytical condition of LC-MS

The mobile phase conditions were as follows: linear gradient analysis with mobile phase A (H_2O with 0.1% formic acid), and mobile phase B (acetonitrile). After a 4 min isocratic run at 100% eluting solvent A, the ratio of eluting solvent B was linearly increased to 35% from 4 to 8 min and to 50% from 8 to 12 min. The use of 50% eluting solvent B was maintained for 5 min. The column was then washed with 100% of eluting solvent B for 5 min, and column equilibration was carried out with 100% eluting solvent A for 7 min. A 3 μL aliquot of the sample solution filtered through a 0.2 μm PTFE filter (EMD Millipore Corporation, Billerica, MA) was injected onto the column with a flow rate of 0.2 mL/min.

For the MS, the instrument was operated using an electrospray ionization source in both positive and negative ionization modes. The ionization parameters were: capillary voltage, 4.5 and -3.5 kV; the nebulizer gas flow, 1.5 L/min; the CDL temperature, 250°C and the heat block temperature, 250°C.

2.2.3 Animal protocol

Male Wistar rats (6 weeks of age) were purchased from Kyudou (Tosu, Japan). The rats were housed in a temperature- and humidity-controlled room (23°C, 78% humidity), and fed a commercial diet (MF; Oriental Yeast, Tokyo, Japan) and water ad libitum. Reversible focal cerebral ischemia was induced with an intraluminal suture to produce a model of MCAO. In brief, anesthesia was induced with 2% isoflurane (Dainippon Pharmaceutical, Osaka, Japan) in air, and was maintained with 1% isoflurane using a facemask. A 1 cm midline incision was made on the anterior neck, and the right common carotid artery, external carotid artery and internal carotid artery were exposed. The common carotid artery and external carotid artery were ligated, and a suture was placed around the internal carotid artery for ligation. An embolus was made by inserting a 4-0 nylon surgical thread into the internal carotid artery through a small incision. The MCA was occluded by advancing the embolus into the internal carotid artery to block the origin of the MCA (Fig. 2-1). After 1 h of MCAO, the MCA was reperfused by withdrawing the embolus. The rectal temperature was maintained by placing the rat on a heating pad under anesthesia. All the procedures and animal care were approved by the Animal Care and Use Committee, Kyushu University, and carried out in accordance with the Guidelines for Animal Experiments, Kyushu University. Extirpated tissue samples were immediately frozen and stored at -80°C prior to use.

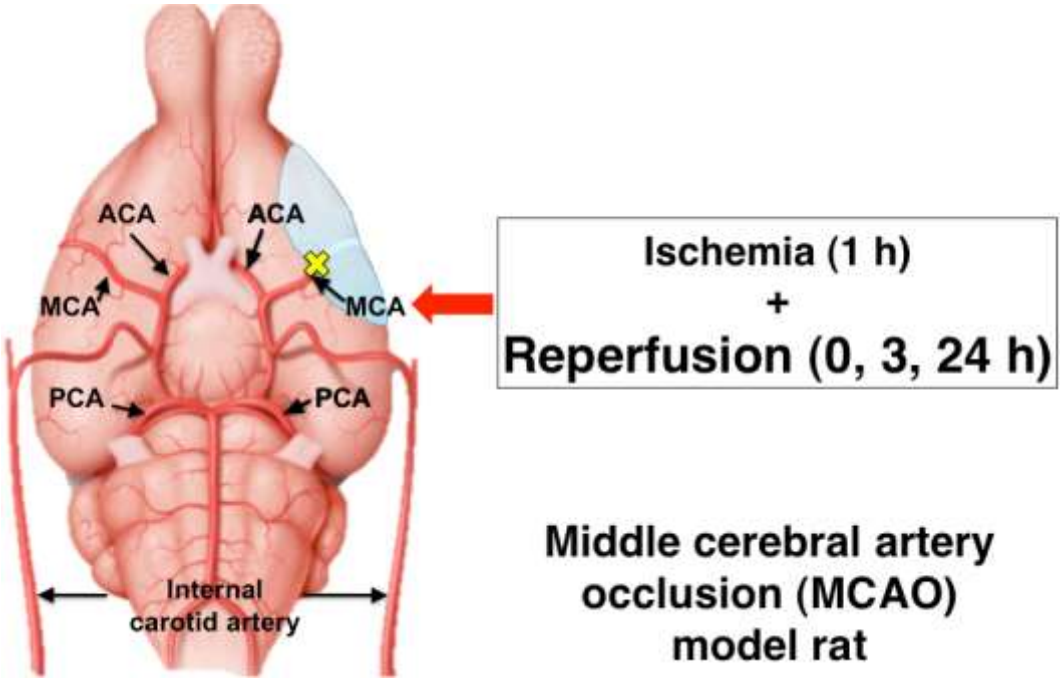

Fig. 2-1 A schematic diagram of the middle cerebral artery occlusion (MCAO) model rat.

MCA; middle cerebral artery, ACA; anterior cerebral artery, PCA; posterior cerebral artery.

2.2.4 MSI analysis of brain sections

In this study, the author used three types of MS instruments. For MSI, single reflectron-type MALDI-TOF-MS (AXIMA Confidence, Shimadzu) was used. And For identification of metabolites by MS/MS analysis, quadrupole ion trap (QIT)-type (AXIMA QIT, Shimadzu) and TOF/TOF-type (AXIMA Performance, Shimadzu) instruments were used. As shown in Fig. 2-2A, 10 μm thick frozen coronal sections were used for the analysis, as described previously (Miura et al. 2010a). In the MSI experiments, the data were acquired in negative ionization mode with 50 μm spatial resolution (10 laser shots/data point), and the signals between *m/z* 50 and 1000 were collected. 9-AA exhibits very few matrixderived interferences in the low-mass range, achieved great improvement for the sensitivity of metabolite analysis (detection potential with subfemtomole sensitivity for various endogenous metabolites) that is advantageous for the simultaneous detection of a variety of cellular metabolites (Miura et al. 2010b; Yukihira et al. 2010). The acquired MSI data were processed with the freely available software program, BioMap (http://www.maldi-msi.org). For normalization of the imaging data, we first constructed an averaged mass spectrum image ranging from *m/z* = 50 to 1000 over the whole region of the tissue section. Second, averaged mass intensity maps of the overall mass range were created. Third, averaged mass intensity maps divided the intensity maps of each peak. This means that the intensity of each peak in each pixel was divided by the average of the total ion count of each pixel. This normalization process is critical for allowing a more quantitative comparison of the MSI data acquired from different tissue sections, because MALDI ionization has been known to cause both spot-to-spot and sample-to-sample variation in the signal intensities based on the heterogeneity of matrix crystals. The signal intensity of each imaging data in the figure was

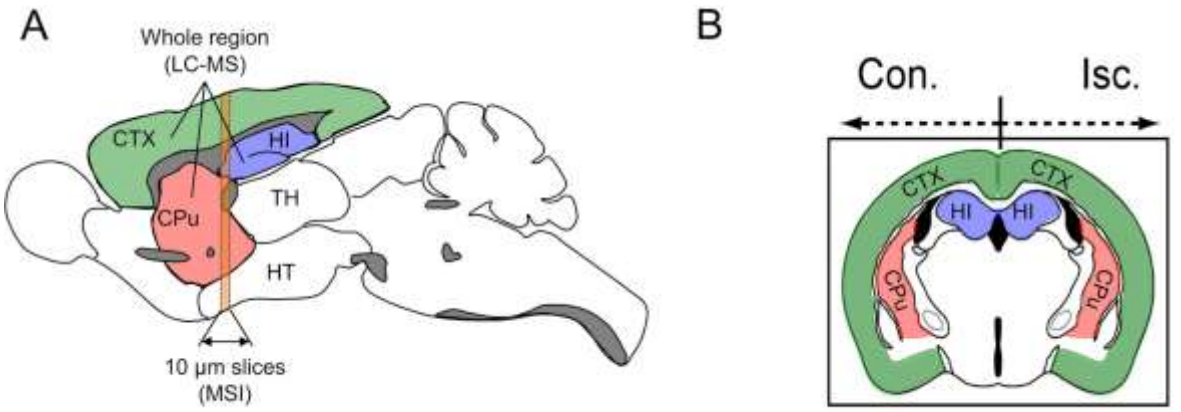

CTX: Cerebral Cortex, HI: Hippocampus, CPu: Corpus Striatum, TH: Thalamus, HT: Hypothalamus

Fig. 2-2 A schematic diagram of the sampling areas for the MSI and LC-MS analyses. Rat brain tissue samples were collected 0, 3 and 24 h after reperfusion following 1 h of MCAO. A schematic illustration represents the structures of the sagittally (A) and coronally (B) sectioned brains. In both the contralateral (Con.) and ischemic (Isc.) hemispheres, the whole cerebral cortex (CTX), hippocampus (HI) and corpus striatum (CPu) were enucleated from the brain for the LC-MS analysis. Coronal brain sections, including the CTX, CPu and HI, were subjected to the MSI analysis.

represented as the normalized intensity.

2.2.5 Metabolomic analysis of brain extracts by LC-MS

The rat brain samples were prepared 0, 3 and 24 h after reperfusion following 1 h of MCAO. Metabolites were extracted from the whole cortex (CTX), hippocampus (HI) and corpus striatum (CPu) in the ischemic (Isc.) and contralateral (Con.) hemispheres. Each tissue sample was homogenized in 80% MeOH, including 10 μM sulfanilamide and 2 μM 4-aminoantipyrine to evaluate the extraction efficiency, on ice (50 mg per tissue in 1 mL vials) using dounce tissue grinders. After centrifugation at 15,000 × g for 30 min at 4°C, the supernatant was collected, and an equal volume of a 2:1 $H_2O/CHCl_3$ solution was added and further mixed vigorously for 30 s. Each sample was then centrifuged at 15,000 × g for 20 min at 4°C. After centrifugation, the aqueous layers were collected. A centrifugal evaporator (CVE-2000, EYELA, Tokyo, Japan) was used for solvent removal and sample concentration. The resultant samples were stored at -80°C until the analysis. Samples were dissolved in 30 μL of 20% acetonitrile, including 10 μM 4-hydroxybenzophenone as an internal standard on ice, prior to the LC-MS analysis (LCMS-IT-TOF, Shimadzu Corporation, Kyoto, Japan). The instrument was fitted with a pentafluorophenylpropyl column (Discovery HS-F5 column 250 × 4.6 mm, Supelco, Bellefonte, PA), ovened at 40°C. Analytical condition is above mentioned (see “analytical condition of LC-MS”). Peak picking, alignment and normalization of the mass spectral data obtained by LC-MS were performed using the Profiling Solution software program (Shimadzu Corporation, Kyoto, Japan). Identified metabolites were quantified using authentic standards, and then the data were expressed as the ratios (ischemic hemisphere/contralateral hemisphere).

2.2.6 Multivariate statistical analysis

A principal component analysis (PCA) was performed using the SIMCA-P+ software program (Version 12, MKS-Umetrics, Umeå, Sweden), allowing the visualization of LC-MS multivariate information. All variables were centered on the average and were normalized by dividing by the standard deviation (unit variance).

Heat maps were displayed using the freely available software program, MultiExperiment Viewer (http://www.tm4.org). The metabolite concentration data of LC-MS and/or mass peak intensity data of MSI were converted to the ratio of the Isc. hemisphere to the Con. hemisphere. A heat map analysis was performed on the data to visualize the metabolic dynamics.

2.3 Results and discussion

2.3.1 Construction of LC-MS based standard metabolites library

Each of 472 metabolite standards were dissolved in water (Mill-Q, Millpore), ethanol, 2-propanol or dimethylsulfoxide (10 mg/mL). Then, standard samples were mixed (each metabolite standards final concentration 1 mg/mL). In addition, 300 μM methionine sulfone, 3 μM 4-aminoantipyrine, 5 μM 2-hydroxyundecanate and 1 μM 4-hydroxybenzophenone were added as an internal standard, prior to analysis.

LC-MS was carried out using an LCMS-IT-TOF (Shimadzu). For chromatographic separation, a pentafluorophenylpropyl (PFPP) column (Discovery HS-F5 column; 250 mm × 4.6 mm; Superco) was used. PFPP column basically provides reversed-phase separations that are distinctly different from reversed-phase columns such as C18 column. Fluorinated, silica-based phases are becoming increasingly popular alternatives to traditional alkyl phases owing to their differential selectivity and retention for a variety of analyte classes. In addition to dispersive interactions available on common C18 phase, dipole interactions of fluorosubstituted ligands, π-π interactions between solutes and phenyl-ligands as well as charge transfer and ion-exchange interactions also have a considerable impact on the selectivity of PFPP column (Bell and Jones 2005; Euerby et al. 2003; Marchand et al. 2005; Needham et al. 2000; Nichthauser and Stepnowski 2009; Yang et al. 2010; Yoshida et al. 2007, 2009).

472 metabolite standards were analyzed by LCMS-IT-TOF in positive/negative mode using PFPP columns. 472 metabolite standards of 302 (63%) with PFPP were successfully detected

(see appendix). Acquisition of LC-MS data was performed under LCMSsolution (Shimadzu). LCMSsolution was used for visualization and manual processing of LC-MS data. Information acquired from LC-MS analysis of metabolite standard (*m/z*, retention time, ion species, intensity and Δppm) was accumulated. Moreover, these information were enrolled in Microsoft Excel using visual basic for application, and it enabled automatically estimation in extracted metabolites from biological samples.

2.3.2 Experimental Flow

In this study, the author analyzed the metabolic dynamics in the brain of MCAO model rats during infarct formation after ischemia-reperfusion by integrating different MS techniques (MSI and LC-MS) (Fig. 2-3). To reveal the differences in metabolic variations in each functional tissue region of the brain, a metabolomic analysis of the CTX, CPu and HI regions was performed (Fig. 2-2). Rat brain samples were collected at different time intervals after ischemia-reperfusion (0, 3 and 24 h, n=5) to investigate the time-dependent metabolic variations after reperfusion following 1 h of MCAO. To compare the metabolic state in the Isc. and Con. hemispheres of the MCAO brain (Fig. 2-2B), metabolites extracted from three different whole tissue regions (CTX, HI and CPu) were also measured by LC-MS. The CTX, CPu and HI tissue samples were coronally sectioned at 10-μm thickness, and metabolites on these partial tissue regions were directly measured by MSI to visualize their spatial distribution.

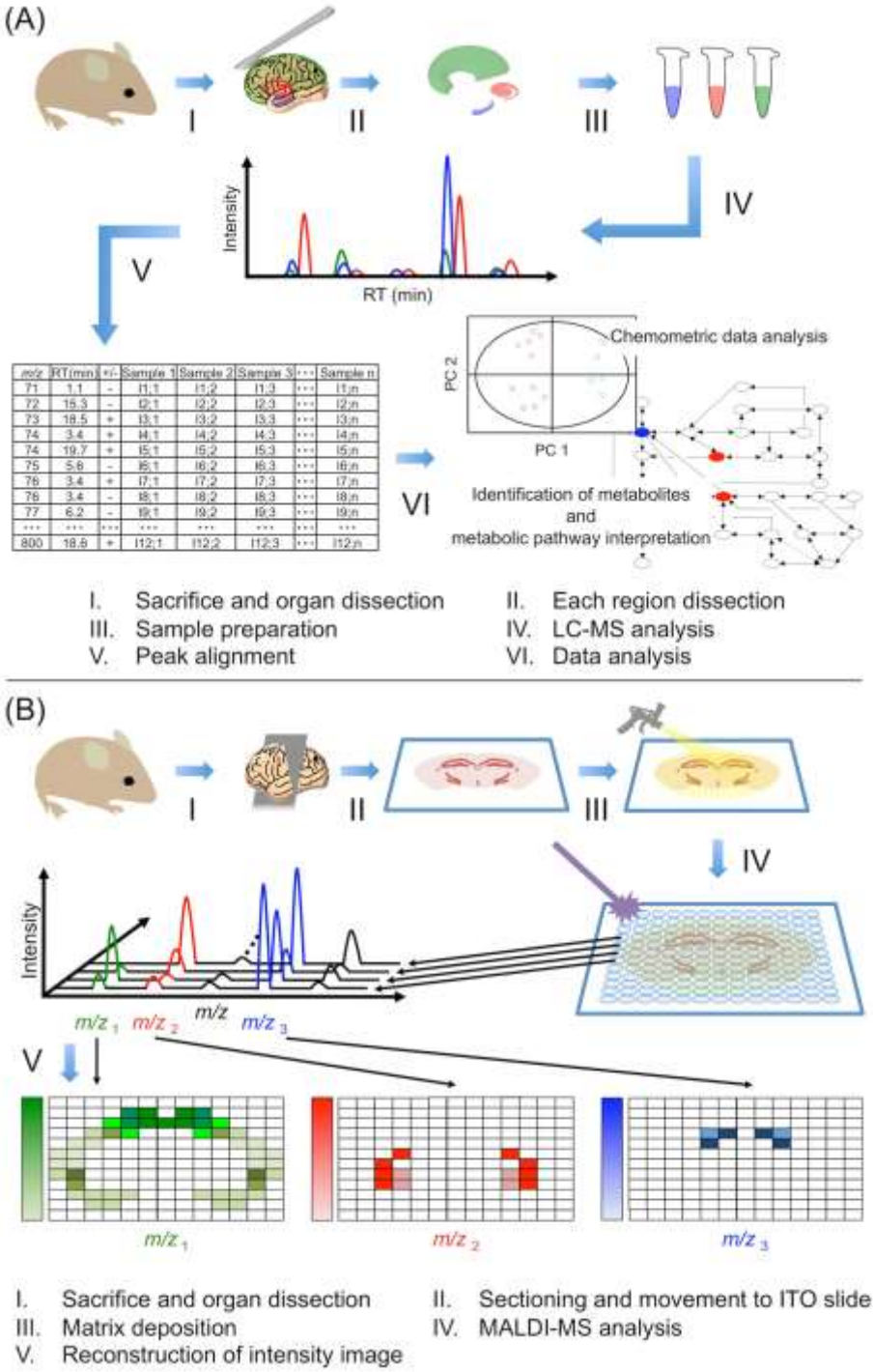

Fig. 2-3 Experimental procedures for the LC-MS and MSI analyses. (A) A schematic representation of the LC-MS analysis workflow. (B) An overview of the MSI analysis procedure.

2.3.3 Global Investigation of Region-Specific Metabolic Dynamics during Infarct Formation

In the present study, the author performed a holistic evaluation of the metabolic profile in three regions (CTX, CPu and HI) and in each hemisphere (Isc. or Con.) at different times after reperfusion (0, 3 and 24 h) by a multivariate statistical analysis using LC-MS data sets (Fig. 2-3). The author used an exploratory data analysis, PCA, which provides a summary or overview of all observations or samples in the data. In addition, groupings trends and outliers can be found easily. In the Con. hemisphere (Fig. 2-4A, Fig. 2-5), the cluster formation of each region was observed, suggesting that the metabolic states were clearly different among the three representative compartments (CTX, CPu and HI). Such region-specific clusters were also formed in the Isc. hemisphere, and further time-dependent separation was observed in both the CTX and CPu regions, unlike the HI (Fig. 2-4B, Fig. 2-6). These results indicate that the metabolic states of the CPu and CTX in the Isc. hemisphere were different from those in the Con. hemisphere, and that there were further time-dependent changes in response to ischemia-reperfusion injury. It is known that the MCA blood supply is important in both the CPu and CTX regions, but not in the HI region (Martin 2003; Kitagawa et al. 1998). This fact may provide insight into the region-specific metabolic alterations after ischemia-reperfusion.

Next, the author investigated the variations in each metabolite level in the CTX and CPu regions showing a significant metabolic change in response to disease progression. With regard to 47 common metabolites detected in both the CTX and CPu regions, changes of their ratio (Isc./Con.) at each time point were shown as a heat map (Fig. 2-7). The concentrations of almost all of the nucleic acids, except for ATP, UMP and CDP-choline in the CPu and ATP and IMP in the CTX, were reduced in a time-dependent manner. The peak accumulation of

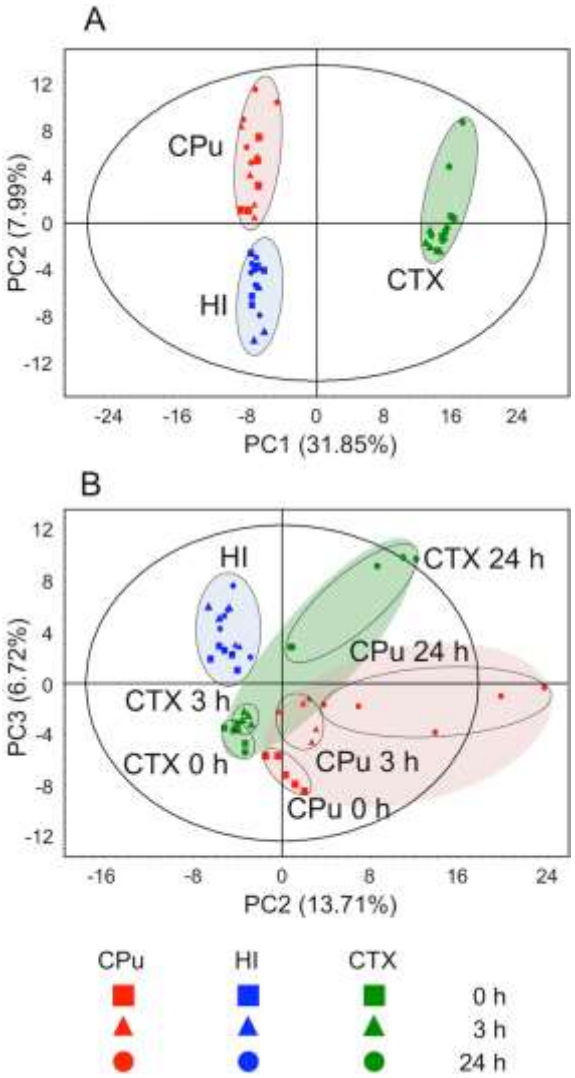

Fig. 2-4 The multivariate analysis of cerebral metabolomic changes induced by reperfusion following 1 h MCAO. The CPu (red), HI (blue) and CTX (green) extracts from the contralateral (A) and ischemic hemispheres (B) at 0 h (square), 3 h (triangle) and 24 h (circle) after reperfusion were measured by LC-MS, and the resulting MS spectral data were subjected to an exploratory data analysis (PCA). The separate score plot is shown for each hemisphere's data sets.

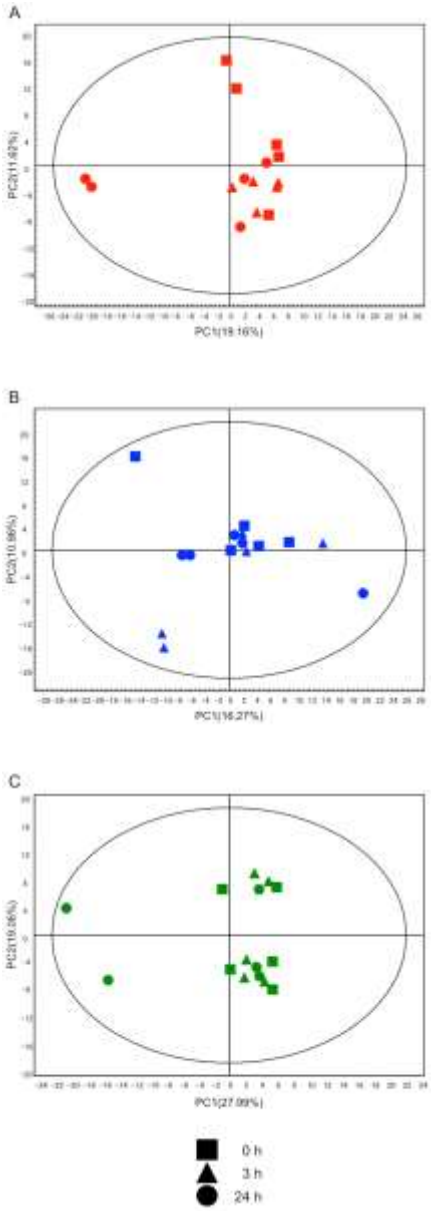

Fig. 2-5 The multivariate analysis of cerebral metabolomic changes in contralateral hemisphere induced by reperfusion following 1 h MCAO. The CPu (A), HI (B) and CTX (C) extracts from the contralateral hemispheres at 0 h (square), 3 h (triangle) and 24 h (circle) after reperfusion were measured by LC-MS, and the resulting MS spectral data were subjected to an exploratory data analysis (PCA).

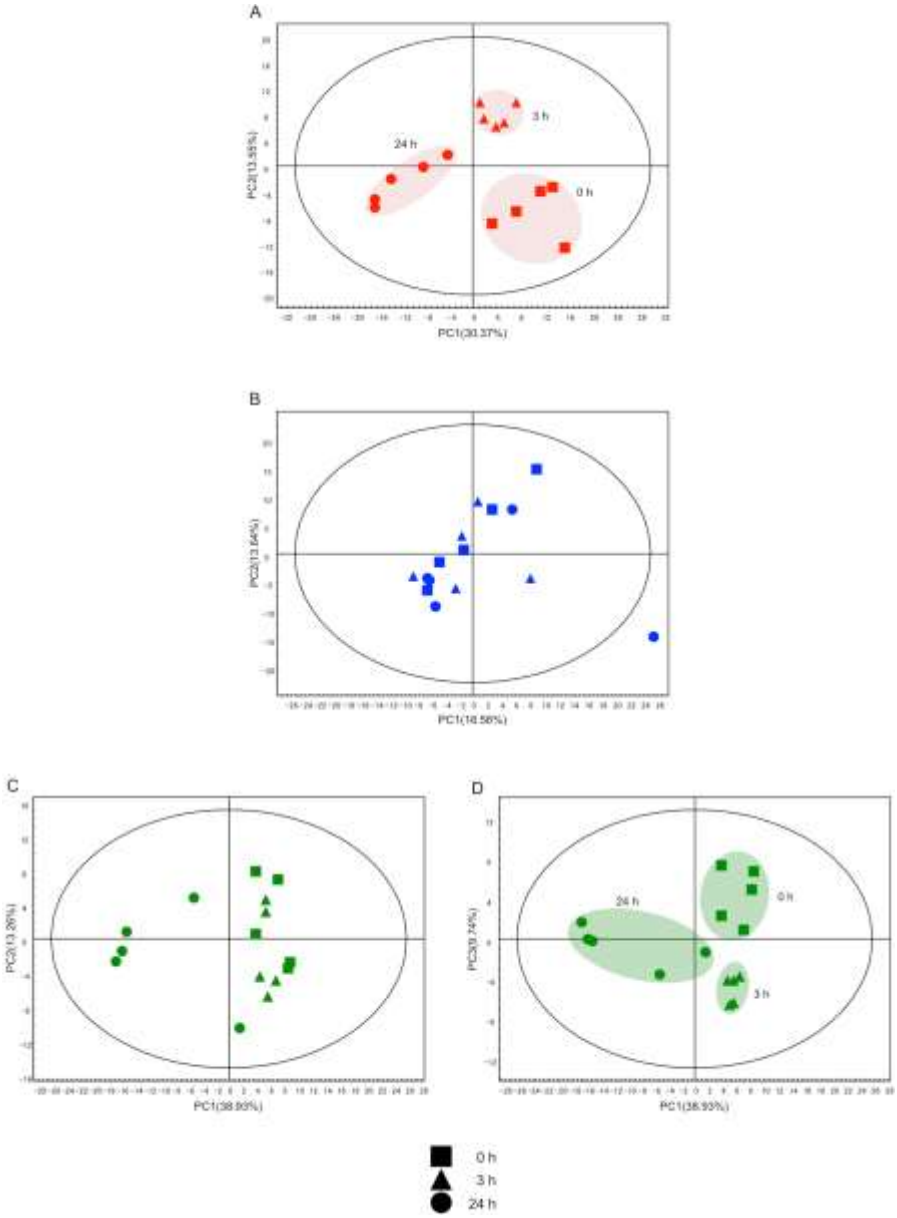

Fig. 2-6 The multivariate analysis of cerebral metabolomic changes in ischemic hemisphere induced by reperfusion following 1 h MCAO. The CPu (A), HI (B) and CTX (C, D) extracts from the ischemic hemispheres at 0 h (square), 3 h (triangle) and 24 h (circle) after reperfusion were measured by LC-MS, and the resulting MS spectral data were subjected to an exploratory data analysis (PCA).

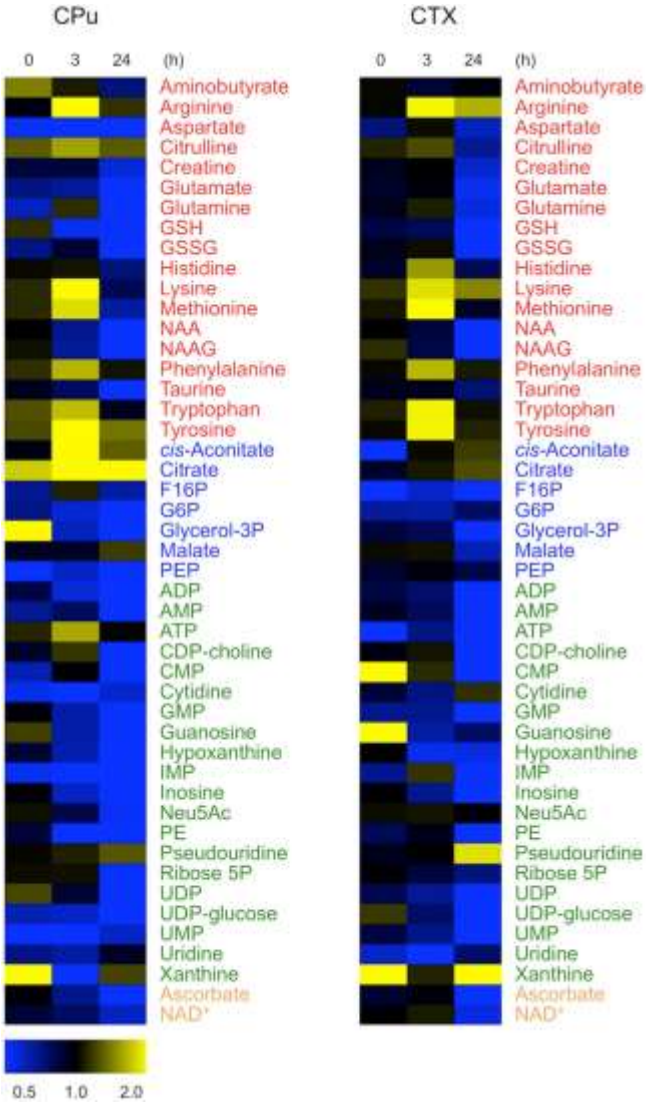

Fig. 2-7 Heat map visualization of the common metabolites identified in two brain components during ischemia-reperfusion. Data were obtained by the average intensity ratio (ischemic hemisphere/contralateral hemisphere) from the LC-MS analysis. The data of 47 common metabolites detected in the CTX and CPu were visualized. The normalized mean values were displayed using the MultiExperiment Viewer (http://www.tm4.org). The colored letters for the heat map are as follows: amino acids (red), central metabolism intermediates (blue), nucleic acids (green), other metabolites (orange).

amino acids (e.g., lysine, phenylalanine, arginine and histidine) was observed at 3 h after reperfusion. The amounts of tricarboxylate cycle (TCA) cycle intermediates, such as citrate, in the Isc. hemisphere were sustained at higher levels compared to the Con. hemisphere. Although many of the detected metabolites were expressed at the same level in both hemispheres just after reperfusion, the difference in concentrations was clearly observed by 3 h after reperfusion. Especially at the time point 24 h after reperfusion, the majority of the metabolites in the CPu and CTX, except for pseudouridine and xanthine (malate in the CPu), were significantly reduced in the Isc. hemisphere compared with the Con. hemisphere.

A previous study reported that the production of reactive oxygen species (ROS) was especially increased at 1 or 2 h after reperfusion (Sims and Muyderman 2010; Lipton 1999). The generation of ROS causes an inactivation of metabolic enzymes and membrane lipid peroxidation (Martin 2003; Bromont et al. 1989). Therefore, reperfusion after 1 h MCAO may induce a failure of energy production and result in a low energy state in the cells present in the occluded MCA area (Sims et al. 2010; Lipton 1999). Moreover, both the synthesis and degradation of proteins are dependent on the energy status (Bylund-Fellenius et al. 1984), and the enzymatic activity of protein synthesis was markedly inhibited after reperfusion (Abe et al. 1988). Hence, the above-mentioned alterations of the amino acid level may be due to an accumulation of amino acids as a result of the catabolism of proteins resulting from the inhibition of protein synthesis. Furthermore, it was already known that the activity of glucose-6-phosphate dehydrogenase in the pentose phosphate pathway, which generates nicotinamide adenine dinucleotide phosphate (NADPH) and ribose-5-phosphate for nucleotide synthesis, is reduced after reperfusion of the MCA (Yousuf et al. 2009; Sarkar and Das 2006). Such an alteration of enzymatic activity may cause a reduction in the overall

nucleic acid level (Fig. 2-7). Taken together, these results raised the possibility that changes in the blood flow during MCA occlusion and reperfusion were associated with the region-specific metabolic behavior involved in the reduction of both energy production and related enzymatic activity. Although many metabolite levels after reperfusion showed similar alterations in the CTX and CPu regions, the variation pattern of particular metabolites, such as malate, was clearly different (Fig. 2-7). A high concentration of citrate was sustained at the CPu in the Isc. hemisphere during reperfusion (0, 3 and 24 h), but the citrate level in the CTX showed a time-dependent accumulation. The metabolic response in the CTX was partially delayed compared with that in the CPu. A previous study reported that a decrease in the blood flow occurred over the whole region of the CPu following occlusion of the MCA, and that the medial area of the anterior CPu had relatively mild ischemia (blood flow rate: 50%) (Memezawa et al. 1992). On the other hand, the CTX is finely separated into several functional regions (Fig. 2-8) and its blood flow is supplied via multiple arteries, including the MCA. Therefore, the occlusion of the MCA causes a heterogeneous biological regulation in different functional regions of the CTX. The blood flow rate in the cingulate cortex was not significantly reduced by occlusion of the MCA, whereas the rates in the neocortex and piriform cortex were markedly decreased (H. Memezawa et al. 1992). Moreover, the parietal cortex and somatosensory cortex, one of the neocortex-constructed regions, exhibited serious ischemia (blood flow rate: 15%), while both other neocortex areas (e.g., the parietal cortex, motor area) and piriform cortex exhibited modest ischemia (blood flow rate: 20%) (H. Memezawa et al. 1992). These circumstances may thus help to explain the differences between the CPu and CTX regions in terms of the time-dependent metabolic dynamics during reperfusion.

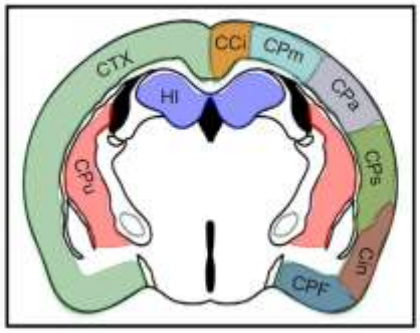

CTX: Cerebral Cortex
HI: Hippocampus
CPu: Corpus Striatum
CCi (mesocortex): Cingulate Cortex, posterior part
CPm (neocortex): Parietal Cortex, Motor Area
CPa (neocortex): Parietal Cortex
CPs (neocortex): Parietal Cortex, Somatosensory Area
Cin (neocortex): Insular Cortex
CPF(neocortex): Piriform Cortex

Fig. 2-8 Schematic illustrations of the functional regions in the cortex. A schematic illustration represents the structure of coronally sectioned rat brain. Different parts of the cerebral cortex are involved in different cognitive and behavioral functions.

2.3.4 Comparison of the Metabolic Variations between the Whole Tissue Region and its Micro-regions in the MCAO Rat Brain after Ischemia-Reperfusion

Generally, an LC-MS analysis is able to detect and determine many kinds of metabolites, but the resulting data are averaged information from the whole tissue because of the extraction step. Tissue samples consisting of several functional compartments, such as brain, may have different metabolic regulation within smaller compartments contained within the single target region. Hence, the LC-MS technique may not correctly trace characteristic metabolic states during a pathological progress. To elucidate accurate and region-specific metabolic changes induced by ischemia-reperfusion, it is necessary to visualize the spatiotemporal metabolic behavior at the micro-regional scale.

To investigate spatially-resolved metabolic dynamics in micro-regions of the CPu and CTX, the author used brain tissue sections (Fig. 2-2B) for MALDI-MSI, which enabled us to simultaneously detect multiple biomolecules with two-dimensional local information (Miura et al. 2010a). Although a part of the MSI data was already reported (Miura et al. 2010a), the author compared the intensities of metabolite peaks between MSI and LC-MS. In the LC-MS analysis, the metabolites were extracted from whole CTX or CPu region in both the Isc. and Con. hemispheres, and the metabolite concentrations were averaged for each whole region (Fig. 2-2A). As shown in Fig. 2-2A, the author prepared 10 μm brain slices, including the central portions of the ischemic lesions. The signal intensity of each metabolite within each region of interest (CTX (green) and CPu (red) as shown in Fig. 2-2B) was averaged, and then the data were used for the assessment of region-specific changes in the metabolite levels.

The data for 12 metabolites commonly detected by both LC-MS and MSI were examined

by a heat map analysis (Fig. 2-9, Table 2-1). Although some partial MSI data were already published (Miura et al. 2010), a further data analysis was performed in this study. Each data was expressed as the ratio of the Isc. hemisphere to the Con. hemisphere. Similar behaviors of several metabolite levels were observed between the MSI and LC-MS data, although the intensity ratios were different. In particular, the time-dependent changes in *N*-acetyl aspartate (NAA) were similar to those of glycerol-3-phosphate (glycerol-3P) and citrate in the CPu and CTX regions in both analytical platforms.

On the other hand, the correlations between the data acquired by two different platforms were low for fructose 1,6-bisphosphate (F16P) (CPu and CTX), glutamate and aspartate (CPu), and UDP-glucose (CTX). The coronally sliced tissue samples of MSI contained the central portions of the ischemic lesions, and the obtained data directly reflect the metabolic change during ischemia-reperfusion in the tissue micro-region level (e.g., highly resolved spatial information of the target region). In contrast, the data from LC-MS were averaged information of the whole region that contained the non-ischemic area. Therefore, the different metabolic events between the analytical platforms may be due to the different metabolic changes between the affected area and its peripheral area. The temporal expression patterns of citrate and glycerol-3P after reperfusion in the CPu and CTX were highly correlated between the MSI and LC-MS data. In the CPu, such metabolite concentrations were similar between the platforms, although these concentrations were clearly different in the CTX. The metabolism in the whole region of the CPu is relatively homogeneously regulated by the MCA, whereas many micro-regions of the CTX are not. The author speculates that the differences in the regulation of blood flow between CTX and CPu regions may have contributed to the differences between the LC-MS and MSI data. The LC-MS data at least

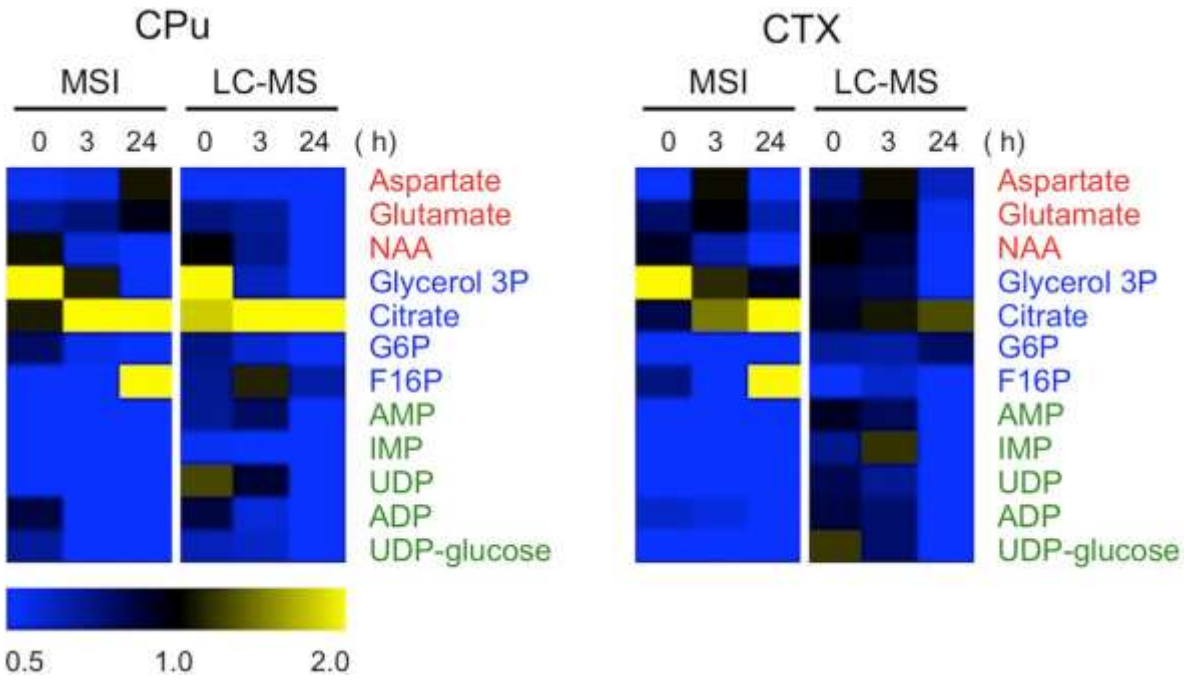

Fig. 2-9 A comparison of the average intensity between the whole tissue regions and partial tissue regions. The average intensity of the whole tissue region is represented as the average intensity ratio (ischemic hemisphere/contralateral hemisphere) for each whole tissue region (LC-MS data, see Fig. 1A). The regional average intensity of a partial tissue region is represented as the average intensity of each region on 10 μm slices (MSI data, see Figure 1B). In the heat map, 12 common metabolites detected by LC-MS and MSI were visualized. The normalized mean values were displayed using the MultiExperiment Viewer (http://www.tm4.org). The colored letters for the heat map are as follows: amino acids (red), central metabolism intermediates (blue), nucleic acids (green), other metabolites (orange).

Table 2-1 Mass-to-charge ratio, molecular species and fragments observed on tissue sections.

m/z	*Molecular species*	*Fragments observed*	*Formula*
426	ADP	328, 291, 159, 134, 79	$C_{10}H_{15}N_5O_{10}P_2$
346	AMP	211, 151, 97	$C_{10}H_{14}N_5O_7P$
339	F1,6P	242, 160, 97, 79	$C_6H_{14}O_{12}P_2$
347	IMP	211, 151, 135, 97, 92, 79	$C_{10}H_{13}N_4O_8P$
565	UDP-glucose	403, 385, 323, 305, 241, 159, 97, 79	$C_{15}H_{24}N_2O_{17}P_2$
403	UDP	323, 305, 291, 159, 111, 97	$C_9H_{14}N_2O_{12}P_2$
132	aspartate	115, 88	$C_4H_7NO_4$
191	citrate	134, 131, 111	$C_6H_8O_7$
259	G6P	199, 169, 97, 79	$C_6H_{13}O_9P$
146	glutamate	128, 102	$C_5H_9NO_4$
171	Glycerol-P	97, 79	$C_3H_9O_6P$
174	NAA	130, 114, 58	$C_6H_9NO_5$

relatively reflected the time-dependent metabolic changes shown by MSI. Therefore, the information about the metabolites detected by LC-MS, but not by MSI, may lead to an understanding of the spatial characteristics of the metabolic state in response to pathological progression.

2.3.5 Spatiotemporal Metabolomic Dynamics and Metabolic Pathway analysis by Combing MSI and LC-MS

As described above, the author found several properties of both MS platforms in the metabolomic analysis. To expand this knowledge to a pathological evaluation, the author applied this technique to visualize more comprehensive spatiotemporal metabolic dynamics in the pathogenesis of ischemia-reperfusion injury (Fig. 2-10). The MSI data, indicating the time-dependent changes in the metabolite distribution at 0, 3 and 24 h after reperfusion, are shown in Fig. 2-10A. A quantitative comparison (the ratio of the Isc. hemisphere to the Con. hemisphere) of time-dependent metabolite variations in molecules related to glycolysis, the TCA cycle, nucleotide and amino acid metabolism in the CPu and CTX was performed by using LC-MS (Fig. 2-10B, 2-11, 2-12, 2-13, 2-14). By integrating the highly quantitative data obtained from LC-MS and the spatially resolved data obtained from MSI, the author could investigate the spatiotemporal metabolic variance.

With regard to the pyrimidine metabolism, in the MSI analysis, a significant decrease in uridine diphosphate (UDP) and UDP-glucose was observed over the whole region of the Isc. hemisphere 24 h after reperfusion (Fig. 2-10A, No. 11 and 12). In the LC-MS analysis, a reduction of UDP derivatives (UDP and UDP-glucose), as well as peripheral metabolites (cytidine diphosphate (CDP)-choline, phosphoethanolamine (PE), and *N*-acetylneuraminate (Neu5Ac)), was observed at 24 h. Previously, it was reported that the production of ROS was increased during ischemia, and its level was further elevated with the onset of reperfusion, and finally, the generated ROS were able to cause injury to the plasma membranes, thus leading to cell death (Bromont et al. 1989). The reduced levels of membrane intermediates, such as PE, CDP-choline, UDP and UDP-glucose, may have been due to their consumption

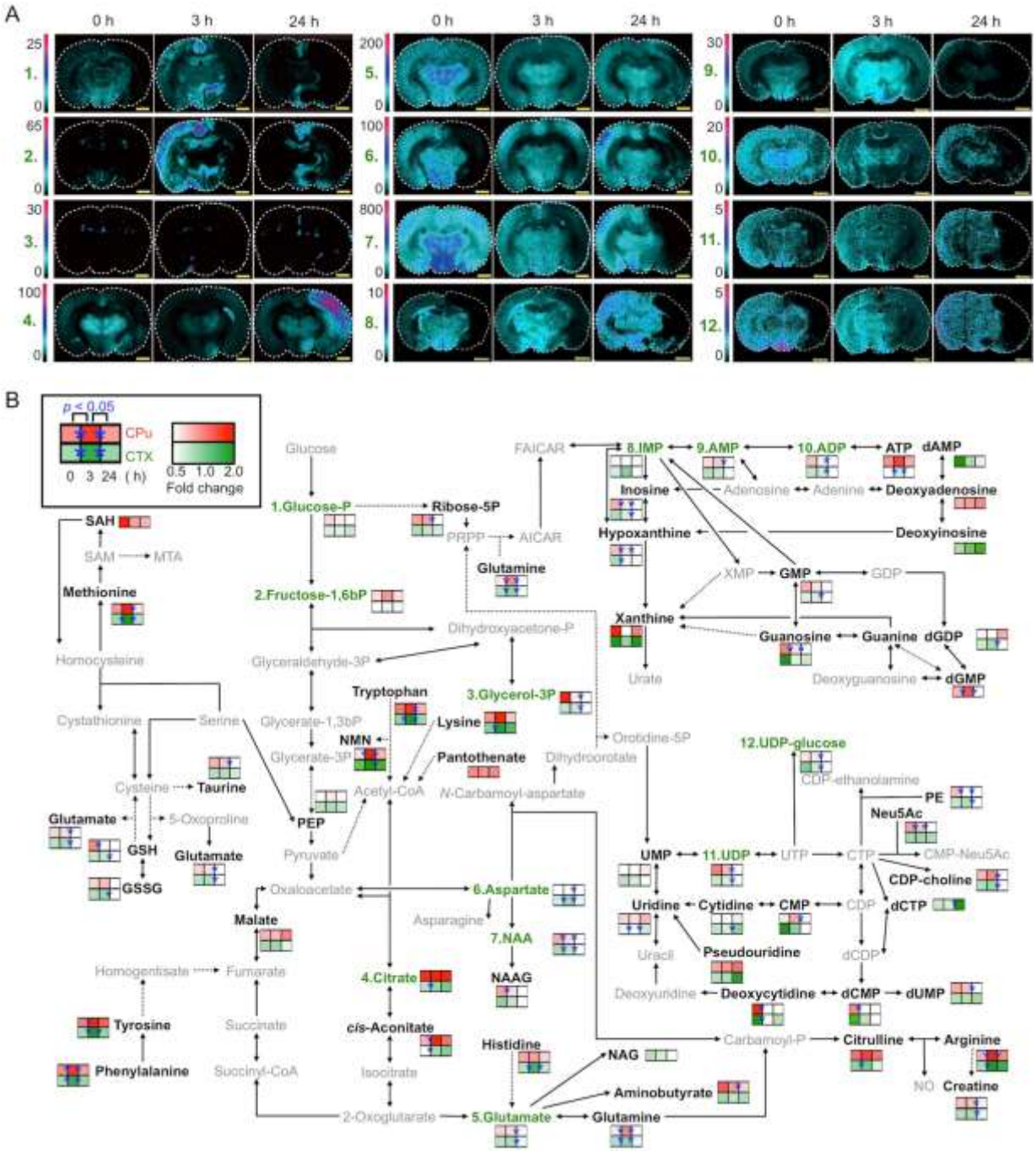

Fig. 2-10 The integrated MSI and LC-MS techniques allow the visualization of drastic changes in the spatiotemporal metabolite distribution. (A) *In situ* MSI visualized dramatic changes in the spatiotemporal metabolite distribution in the MCAO rat brain. Metabolites related to nucleotide and amino acid metabolism, as well as the central pathway, were simultaneously visualized in a single MSI experiment. Scale bar = 1.0 mm. Data (No.1~7) were reprinted with permission from the author (Miura et al. 2010a).

(Fig.2-10 continue)

(B) Comparative visualization of the central metabolic pathway and its peripheral metabolic pathways in the CPu (upper box, red) and CTX (lower box, green) in the MCAO rat brain, as determined by LC-MS. Significant differences (Student's *t*-test, $*P<0.05$) are indicated by asterisks on the colored boxes. Black and grey letters indicate LC-MS-detected metabolites and unmeasured metabolites, respectively. Green letters indicate metabolites detected by both LC-MS and MSI. Solid arrows represent a single step connecting two metabolites, and dotted arrows represent multiple steps.

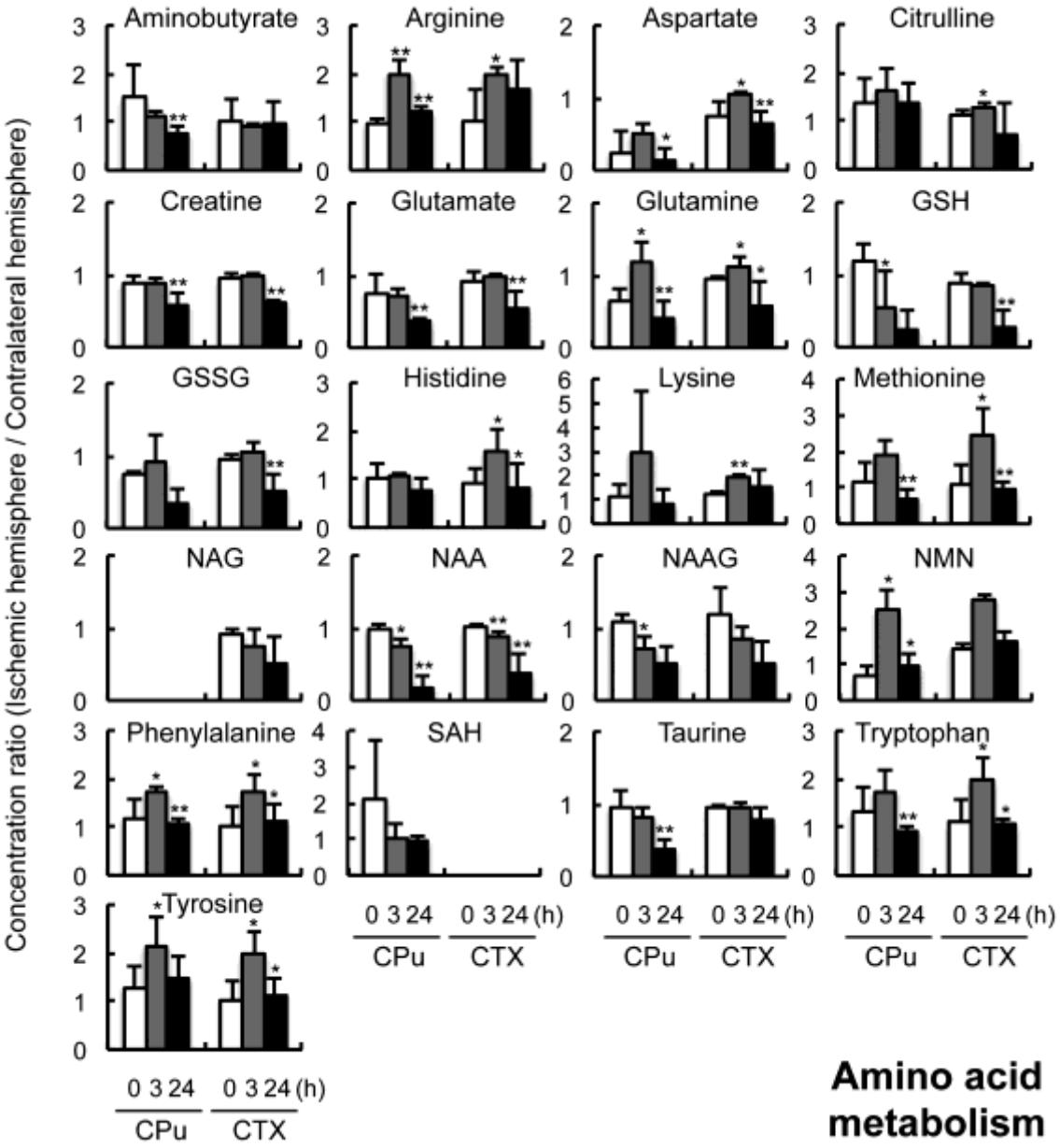

Fig. 2-11 The LC-MS analysis of region-specific metabolomic changes during reperfusion. The data indicate the average intensity (ischemic hemisphere/contralateral hemisphere) of amino acid metabolism related metabolites at each whole tissue region (CPu or CTX). The values are the means of five replicates + SD. Asterisks indicate significant differences between 0 and 3 h, or 3 and 24 h, as determined by Student's *t*-test (*$P < 0.05$; **$P < 0.01$).

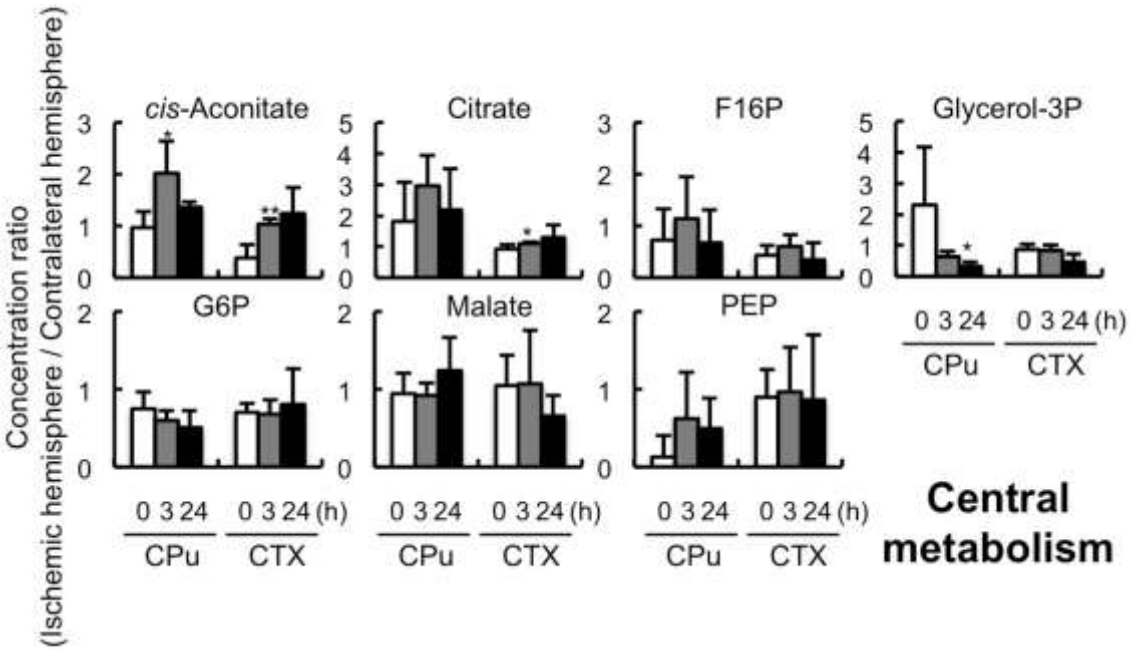

Fig. 2-12 The LC-MS analysis of region-specific metabolomic changes during reperfusion. The data indicate the average intensity (ischemic hemisphere/contralateral hemisphere) of central metabolism related metabolites at each whole tissue region (CPu or CTX). The values are the means of five replicates + SD. Asterisks indicate significant differences between 0 and 3 h, or 3 and 24 h, as determined by Student's *t*-test (**P* < 0.05; ***P* < 0.01).

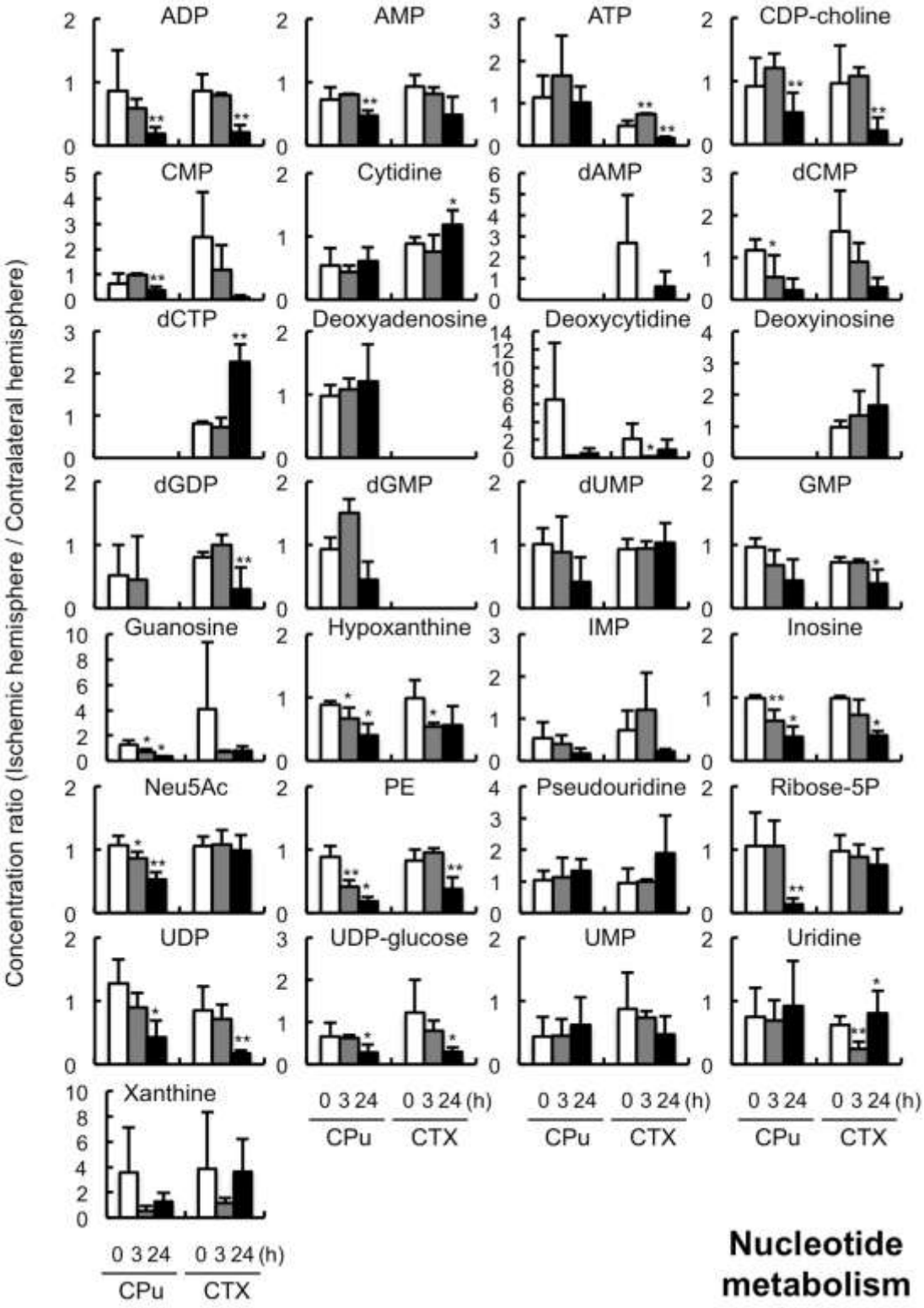

Fig. 2-13 The LC-MS analysis of region-specific metabolomic changes during reperfusion.

(Fig.2-13 continue)

The data indicate the average intensity (ischemic hemisphere/contralateral hemisphere) of nucleotide metabolism related metabolites at each whole tissue region (CPu or CTX). The values are the means of five replicates + SD. Asterisks indicate significant differences between 0 and 3 h, or 3 and 24 h, as determined by Student's *t*-test (*$P < 0.05$; **$P < 0.01$).

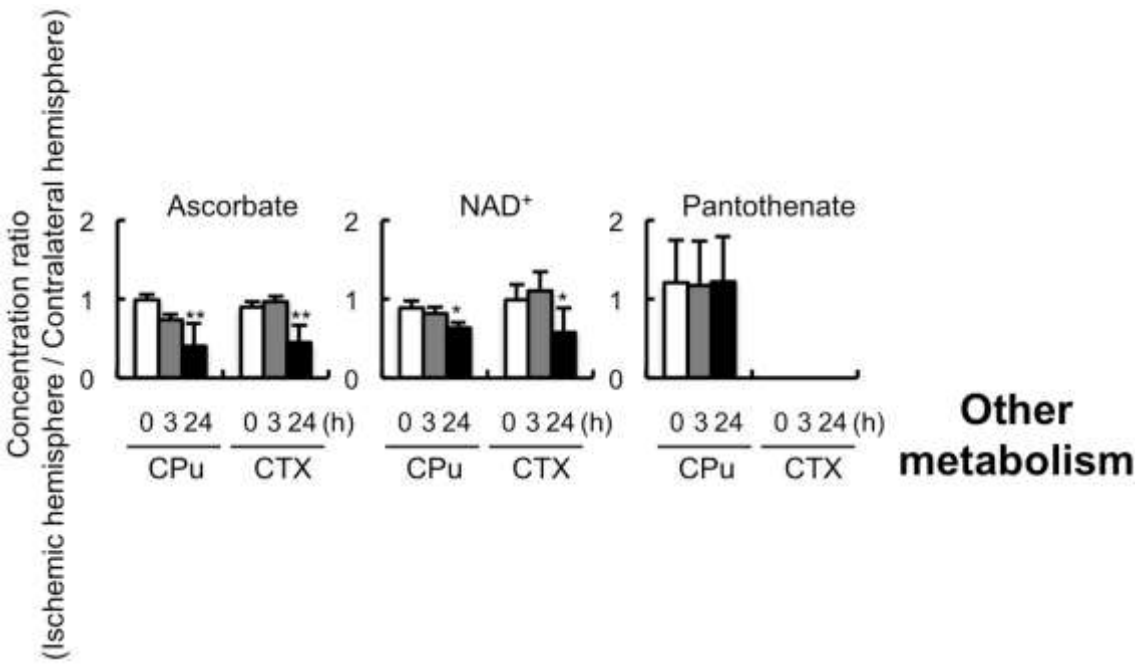

Fig. 2-14 The LC-MS analysis of region-specific metabolomic changes during reperfusion. The data indicate the average intensity (ischemic hemisphere/contralateral hemisphere) of metabolites except for amino acid, central, and nucleic acid metabolism related metabolites at each whole tissue region (CPu or CTX). The values are the means of five replicates + SD. Asterisks indicate significant differences between 0 and 3 h, or 3 and 24 h, as determined by Student's *t*-test (*$P < 0.05$; **$P < 0.01$).

for plasma membrane synthesis to restore the membrane integrity following ROS-mediated damage.

The levels of many amino acids, the catabolites of proteins, were increased, except for glutamate, which is related to various metabolic reactions, after 3 h of reperfusion in the Isc. hemisphere (Fig. 2-10B). The inhibition of protein synthesis and the progression of protein degradation after reperfusion have been reported previously (Bylund-Fellenius et al. 1984; Neumar 2000). Although MSI data alone cannot explain the characteristic behavior of amino acids, the above-mentioned protein alterations after reperfusion probably contribute to the accumulation of the building blocks of proteins 3 h after reperfusion. MSI also showed a significant increase in the aspartate level in the whole regions of the Isc. hemisphere after 3 h of reperfusion (Fig. 2-10A, No.6). In this study, MSI was not able to trace most of the amino acids measured by LC-MS. However, our findings that the LC-MS data exhibited a relatively high correlation with the MSI data (Fig. 2-9) suggest that amino acids showing a similar behavior to aspartate in the LC-MS results may show an aspartate-like distribution in the Isc. hemisphere, although further studies are needed to confirm whether this is the case.

On the other hand, the levels of almost all amino acids, including glutamate, were reduced at 24 h (Fig. 2-10B). The energy production was reported to be depressed after reperfusion due to the inactivation of TCA cycle-related enzymes, aconitase and 2-oxoglutarate dehydrogenase, resulting from the hypergeneration of ROS (Tretter and Adam-Vizi 2000). In addition, we previously found that citrate synthase activity was not affected by ischemia-reperfusion (Miura et al. 2010a). The LC-MS analysis in the present study also showed that TCA cycle intermediates, citrate (CPu and CTX) and malate (CPu), were accumulated in the Isc. hemisphere after reperfusion. These observations raise a possibility

that the reduction of amino acids may be partially due to their utilization as TCA cycle intermediates for reactivation of the TCA cycle. The MSI data also revealed that the increase in citrate, as well as the decrease in aspartate and glutamate after 24 h of reperfusion were characteristically heterogeneously distributed in the Isc. hemisphere (Fig. 2-10A, No. 4-6).

As previously mentioned in the description of the LC-MS-based metabolic profiling (Fig. 2-4), the blood supply of the brain is provided via not only the MCA, but also several other arteries (such as the anterior and posterior cerebral arteries). The artery-regulated region is not necessarily consistent with each functional compartment. In fact, the blood supply of the CTX is regulated by both the MCA and other arteries. Intriguingly, the region with the most characteristic metabolic variation (citrate, aspartate and glutamate) shown by MSI was relatively consistent with the specific region demonstrating remarkable lowering of the blood flow by occlusion of the MCA (Kitagawa et al. 1998).

2.4 Concluding Remarks

In the present study, the author was able to visualize diverse spatiotemporal metabolic dynamics within the central metabolic pathway and its periphery in the MCAO rat brain during infarct formation using an integrated technique combining MSI with LC-MS. Using representative tissue samples of different functional compartments, LC-MS was used to trace the temporal changes of many metabolites which could not be visualized by MSI. Significant metabolic changes in the blood supplying area from the MCA were observed by a series of region-specific behavioral analyses. To date, conventional pathological analysis of MCAO models has not shown the spatiotemporal metabolic behaviors after reperfusion. In contrast, the author herein visualized a MCA-regulated metabolic change in several metabolic pathways, including the pyrimidine-, amino acid- and TCA cycle-related metabolism, during pathological progression. Thus, our new approach combining MSI (spatial information but low coverage) and its complementary technique LC-MS (high coverage but loss of spatial information) will provide insight into the understanding of the complex pathological mechanism(s) of ischemia-reperfusion injury. This could be broadly applicable to emerging issues in the precise pathological evaluation of target tissues in both preclinical and clinical settings, and may become a compulsory technique for *in situ* pharmacometabolomics and biomarker discovery.

CHAPTER 3

Metabolic Analysis of Cisplatin-induced Acute Kidney Injury

3.1 Introduction

Cisplatin [*cis*-diamminedichloroplatinum (II)] is a potent anticancer drug that has been used successfully to treat tumors of the head, neck, lungs, and genitourinary tract. The antitumor activity of cisplatin is thought to be mediated by its binding to DNA (Fig 3-1), leading to the formation of adducts and cross-links that lead to inhibition of DNA synthesis (Johnsson et al. 1995). Cisplatin is one of the most remarkable successes in 'the war on cancer'. Since the accidental discovery over four decades ago, cisplatin has been widely used for chemotherapy. It is potent, demonstrating one of the highest cure rate, for example, over 90% in testicular cancers (Arany and Safirstein 2003; Wang and Lippard 2005; Siddik 2003).

Although cisplatin has been a mainstay for cancer therapy, its use is mainly limited by severe side effects in normal tissues (Arany et al. 2003; Siddik 2003). The side effects in the use of cisplatin include neurotoxicity, ototoxicity, nausea and vomiting, and nephrotoxicity. Especially, most serous and one of the more common presentations is acute kidney injury (AKI), one of the nephrotoxicity, which occurs in 20-30% of patients (Miller et al. 2010). For years, various approaches have been attempted to curtail these side effects. One strategy is to synthesize and screen for novel cisplatin analogues that have lower toxicity in normal tissues. In this direction, several cisplatin analogues, such as carboplatin and oxaliplatin, have been identified with less severe side effect (Pasetto et al. 2006). Another approach that has been used with some success is to hydrate the patients during cisplatin treatment (Cornelison and Reed 1993; Bajorin et al. 1986). Despite these efforts, the side effects of cisplatin, particularly nephrotoxicity, remain a major factor that limits the use and efficacy of cisplatin in cancer

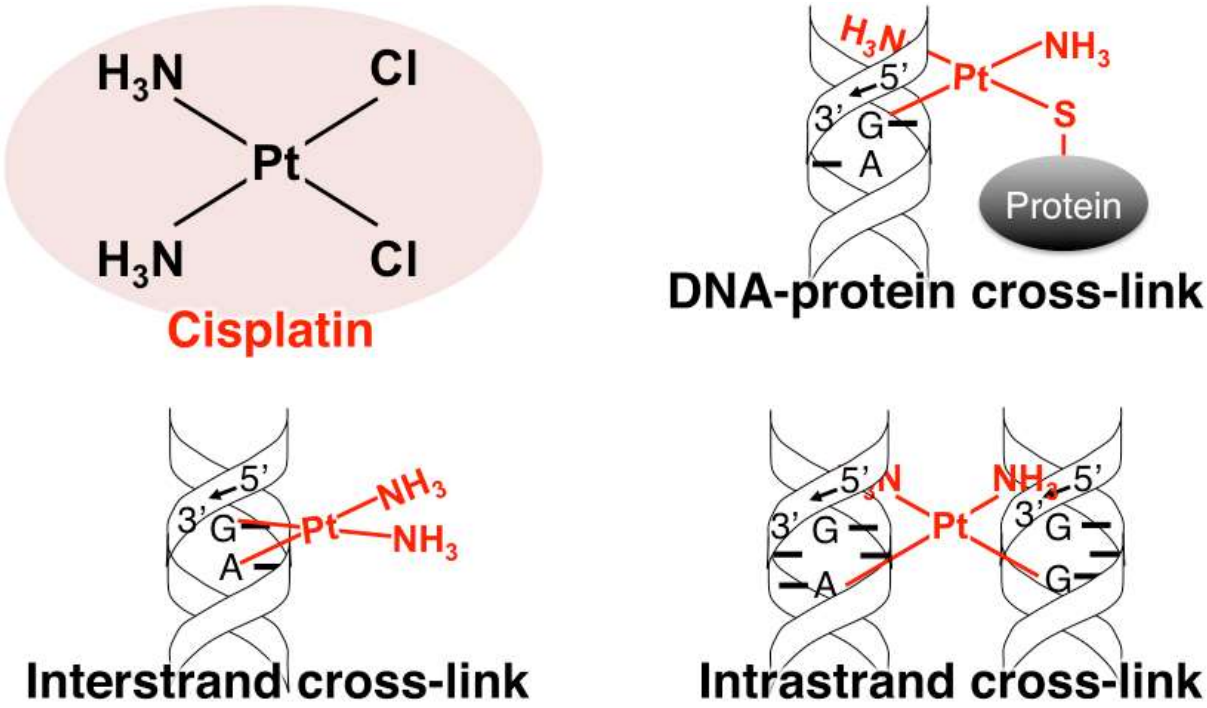

Fig. 3-1 Interaction of cisplatin with DNA nucleobases.

therapy.

The major limitation of cisplatin chemotherapy is the development of dose-dependent nephrotoxicity in about 30% of patients, preventing the administration of high doses to take full advantage of its chemotherapeutic efficacy (Ries and Klastersky 1986; Schrier 2002). To date, the mechanism of cisplatin-induced nephrotoxicity is known that increased oxidative stress, inflammation and DNA damage have been implicated in cisplatin-induced renal tubular cell injury (Davis et al. 2001; Mukhopadhyay et al. 2010; Ramesh and Reeves 2002) because cisplatin not only target DNA but also cause damage to other cellular components. However, the precise mechanisms of cisplatin's renal toxicity are not yet well understood (Mukhopadhyay et al. 2012). Understanding the mechanism of cisplatin nephrotoxicity could lead to novel renoprotective interventions (Pabla and Dong 2008).

Previous research addressing the mechanisms of disease, including cisplatin-induced nephrotoxicity, have been targeted to particular genes, proteins and metabolites, and the analysis of only a part of the functions related to these biomolecules has been the focus of most investigations (Siddik 2003; Wang et al. 2005; Ramesh et al. 2002). However, the data obtained from such studies is insufficient to understand the complex disease processes using conventional techniques alone, because various other, untargeted, biomolecules may participate in the pathological progress (Fig.3-2) (Miller et al. 2010). Behaviors of biomolecules are drastically altered by the time elapsed from disease onset, and there are often local differences within the lesion site (Matsumoto et al. 1993). Therefore, to obtain a precise understanding of the biological complexity of disease progression, it is necessary to obtain more comprehensive and spatiotemporal information about the biomolecules in the target site.

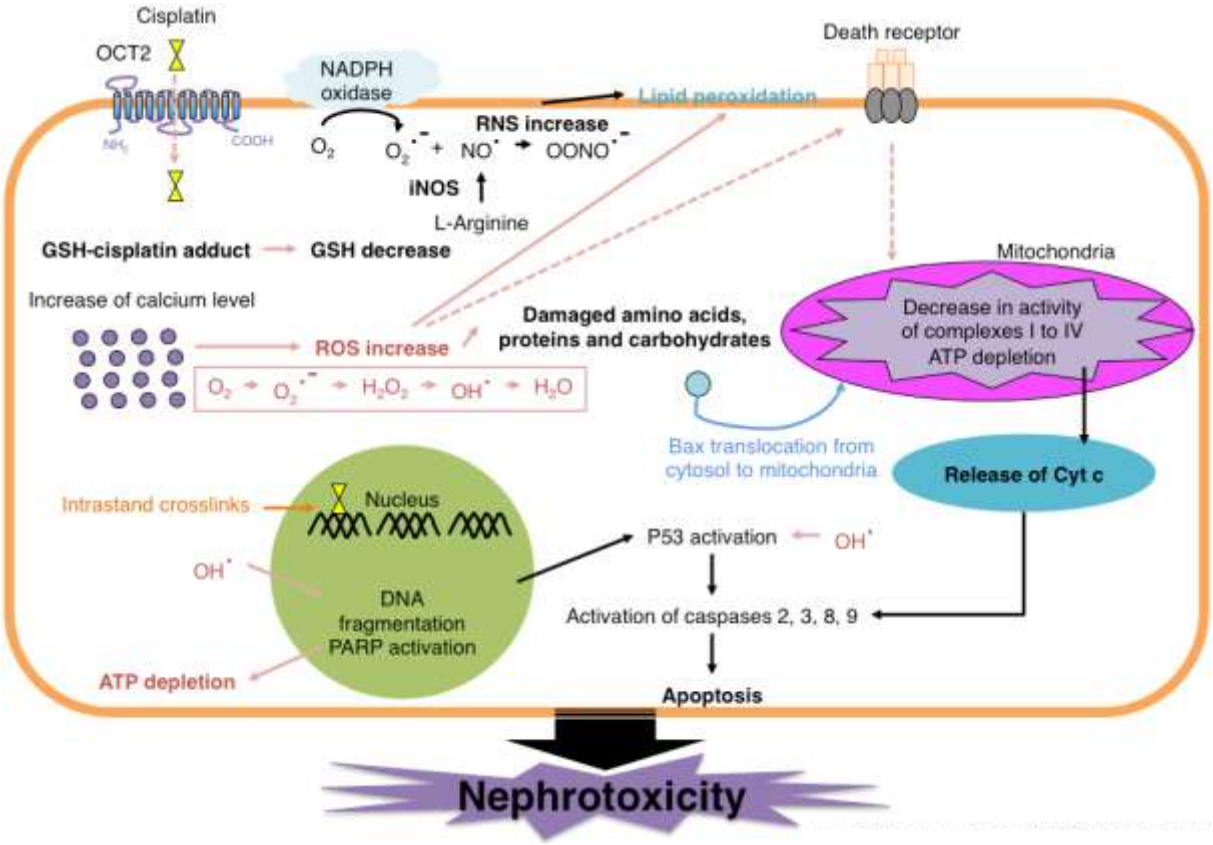

Fig. 3-2 Biochemical cell death pathways induced by cisplatin.

Recently, “omics” technology, the analysis of comprehensive biomolecules, has received considerable attention. In particular, metabolomics, the analysis of comprehensive metabolites as a compound-level phenotype of genomic information, can elucidate the biological phenomena unresolved by transcriptomics and proteomics. Moreover, most studies targeting the mechanism of cisplatin-induced nephrotoxicity have been focused on proximal renal tubule (Blanc et al. 2000; Chen et al. 1999; Mandic et al. 2001; Mese et al. 2000; Razzaque et al. 1999; Takeda et al. 1997; Widmann et al. 1997; Wang et al. 2000). In the pathological analysis of tissues with many functional compartments, such as the brain and kidney, it is necessary to not only determine the comprehensive metabolites involved in these processes, but also to visualize their spatial distribution within the tissue.

Previously, we developed an integrated technique combining MSI with LC-MS to analyze the metabolic dynamics during pathological progression and succeed that revealed the diverse spatiotemporal metabolic behavior in the rat brain in a model of MCAO during infarct formation after ischemia-reperfusion (Irie et al. 2013). In this study, the author used a well-established mouse model of cisplatin-induced nephropathy (Wei et al. 2007; Tadagavadi and Reeves 2010b; Lee et al. 2006; Tadagavadi and Reeves 2010a; Mukhopadhyay et al. 2012) to investigate the time-dependent spatiotemporal metabolic variance in cisplatin-induced kidney injury applied integrated technique combining MSI with LC-MS.

3.2 Materials and methods

3.2.1 Materials

Indium tin oxide (ITO)-coated slide glass and 9-aminoacridine (9-AA) hydrochloride were obtained from Sigma-Aldrich (St Louis, MO, USA). 9-AA was recrystallized prior to use. Organic solvents, internal standards and metabolite standards used in this study were purchased from Wako Pure Chemical Industries, Ltd.

3.2.2 Animals and drug treatment

Six-week-old male C57BL/6NJ mice were obtained from Kyudou (Fukuoka, Japan). All animals were kept in a temperature-controlled environment with a 12-h light-dark cycle and were allowed free access to food and water at all times for 7 days before the injection of cisplatin. Cisplatin (Sigma, St. Louis, MO) was dissolved in saline at a concentration of 1 mg/ml. Mice were given a single intraperitoneal injection of either control (saline) or cisplatin (30 mg/kg b.w.). After the injection of cisplatin, mice were returned to their cages and allowed free access to food and water. A total of 5 animals were examined at each of these time points (3, 6, 24 and 72 h following cisplatin injection and 72 h after saline administration). At the end of each of these time points, the animals were anesthetized with 2% isoflurane (Dainippon Pharmaceutical, Osaka, Japan) in the air, the abdominal cavity opened, and urine and blood obtained via puncture of the bladder for BUN analysis. The blood samples stood at 4°C overnight. The mice were sacrificed, and both kidneys harvested. Left kidneys were coronary separated at half. Right kidneys, one half of each left kidney and

liver were snap frozen in liquid nitrogen and stored at –80°C until further processing. The other half of left kidney was embedded in OCT compound (Sakura Finetek) and frozen sections (10 μm) obtained for MSI and immunohistochemistry. All the procedures and animal care were approved by the Animal Care and Use Committee, Kyushu University, and carried out in accordance with the Guidelines for Animal Experiments, Kyushu University.

3.2.3 Blood urea nitrogen analysis

Blood urea nitrogen (BUN) concentration was determined colorimetrically using a commercially available kit (Wako Chemicals, Japan).

3.2.4 Metabolomic analysis of kidney extracts by LC-MS

The mouse kidney samples were prepared control, 3, 6, 24 and 72 h after cisplatin injection. Metabolites were extracted from the whole kidney. Each tissue sample was homogenized in 80% MeOH, including 2 μM 4-aminoantipyrine to evaluate the extraction efficiency, on ice (50 mg per tissue in 1 mL vials) using dounce tissue grinders. After centrifugation at 15,000 × g for 30 min at 4°C, the supernatant was collected, and an equal volume of a 2:1 $H_2O/CHCl_3$ solution was added and further mixed vigorously for 30 s. Each sample was then centrifuged at 15,000 × g for 20 min at 4°C. After centrifugation, the aqueous layers were collected. A centrifugal evaporator (CVE-2000, EYELA, Tokyo, Japan) was used for solvent removal and sample concentration. The resultant samples were stored at -80°C until the analysis. Samples were dissolved in 30 μL of 20% acetonitrile, including 10 μM 4-hydroxybenzophenone as an internal standard on ice, prior to the LC-MS analysis (LCMS-IT-TOF and LCMS-2020, Shimadzu Corporation, Kyoto, Japan). LCMS-IT-TOF for non-target analysis was fitted with

a pentafluorophenylpropyl column (Discovery HS-F5 column 250 × 4.6 mm, Supelco, Bellefonte, PA), ovened at 40°C. The mobile phase conditions were as follows: linear gradient analysis with mobile phase A (H_2O with 0.1% formic acid), and mobile phase B (acetonitrile). After a 4 min isocratic run at 100% eluting solvent A, the ratio of eluting solvent B was linearly increased to 35% from 4 to 8 min and to 50% from 8 to 12 min. The use of 50% eluting solvent B was maintained for 5 min. The column was then washed with 100% of eluting solvent B for 5 min, and column equilibration was carried out with 100% eluting solvent A for 7 min. A 3 μL aliquot of the sample solution filtered through a 0.2 μm PTFE filter (EMD Millipore Corporation, Billerica, MA) was injected onto the column with a flow rate of 0.2 mL/min. For the MS, the instrument was operated using an electrospray ionization source in both positive and negative ionization modes. The ionization parameters were: capillary voltage, 4.5 and -3.5 kV; the nebulizer gas flow, 1.5 L/min; the CDL temperature, 250°C and the heat block temperature, 250°C.

LCMS-2020 (QMS) for target analysis was fitted with a C18 column (Unison UK-C18 : 3 μm, 2x150 mm, Imtakt Corporation), ovened at 40°C. The mobile phase conditions were as follows: linear gradient analysis with mobile phase A (10mM Tributylamine/15mM Acetic acid (ion pare)), and mobile phase B (methanol). After a 8 min isocratic run at 100% eluting solvent A, the ratio of eluting solvent B was linearly increased to 90% from 8 to 24 min. The column equilibration was carried out with 100% eluting solvent A for 6 min. A 10 μL aliquot of the sample solution was injected onto the column with a flow rate of 0.3 mL/min. MS coupling with ESI interface was used in negative ion mode and SIM at *m/z* 87, 115, 116, 117, 130, 131, 132, 133, 145, 146, 148, 164, 167, 173, 180, 185, 203, 229, 259, 275, 289, 339, 346, 426, 506, 565, 662, 664, 742, 744, 808 and 866. $[M-H]^-$ was selected as the SIM ion in

quantification. The ionization parameters were: capillary voltage, -3.5 kV; the nebulizer gas flow, 1.5 L/min; the CDL temperature, 250°C and the heat block temperature, 400°C.

Peak picking, alignment and normalization of the mass spectral data obtained by LC-MS were performed using the Profiling Solution software program (Shimadzu Corporation, Kyoto, Japan). Identified metabolites were quantified using authentic standards, and then the data were expressed as the ratios (each injection sample/control sample).

3.2.5 MSI analysis of kidney sections

In this study, the author used three types of MS instruments. For MSI, reflectron-type MALDI-TOF-MS (AXIMA Performance, Shimadzu) was used. And For identification of metabolites by MS/MS analysis, quadrupole ion trap (QIT)-type (AXIMA QIT, Shimadzu) and TOF/TOF-type (AXIMA Performance, Shimadzu) instruments were used. 10 μm thick frozen coronal sections were used for the analysis, as described previously (Miura, Fujimura, Yamato, et al. 2010). In the MSI experiments, the data were acquired in negative ionization mode with 50 μm spatial resolution (10 laser shots/data point), and the signals between *m/z* 50 and 1000 were collected. 9-AA exhibits very few matrixderived interferences in the low-mass range, achieved great improvement for the sensitivity of metabolite analysis (detection potential with subfemtomole sensitivity for various endogenous metabolites) that is advantageous for the simultaneous detection of a variety of cellular metabolites (). The acquired MSI data were processed with the SIMedit（Shimadzu） and the freely available software program, BioMap (http://www.maldi-msi.org).

3.2.6 Statistical analysis

BUN data are expressed as mean±*s. e.*, LC-MS data are presented as mean±*s. d*. Statistical analysis was performed using unpaired Student's *t*-test. A *p*-value of <0.05 was considered to be statistically significant.

A principal component analysis (PCA) was performed using the SIMCA-P+ software program (Version 12, MKS-Umetrics, Umeå, Sweden), allowing the visualization of LC-MS multivariate information. All variables were centered on the average and were normalized by unit variance.

Heat map analysis was displayed using the freely available software program, MultiExperiment Viewer (http://www.tm4.org). The metabolite concentration data of LC-MS were converted to the ratio of the cisplatin exposure samples to the control samaples. A heat map analysis was performed on the data to visualize the metabolic dynamics.

3.3 Results

3.3.1 Body weight and blood analyses

Kidney function was monitored by measuring BUN and body weight after intraperitoneal injection of saline or cisplatin, Fig. 3-3a and b present the changes on BUN and body weight in mice treated with saline (control), and cisplatin. Cisplatin treatment at 3-24 h did not result in significant change in average body weight and BUN of the mice, although the BUN at 24 h after injection was numerically increased than in control mice. On the other hand, cisplatin-treated mice at 72 h showed a 1.3-fold decrease (P<0.05) in control mice. Moreover, BUN levels were 5-fold higher in cisplsatin treated after 72 h mice (P<0.05) than in the saline-treated control mice, indicating a severe decline in kidney function.

3.3.2 Global investigation of metabolic dynamics during disease formation

In the present study, the author performed a holistic evaluation of the metabolic profile in kidney at control and different times after cisplatin injection (3, 6, 24 and 72 h) by a multivariate statistical analysis using LC-MS data sets. The author used an exploratory data analysis, principal component analysis (PCA), which provides a summary or overview of all observations or samples in the data. In addition, groupings trends and outliers can be found easily. PCA of the spectra integrals detected by LC-MS showed distinct clusters for control kidney and for kidney collected on early phase (3 and 6 h), intermediate phase (24 h), and last phase (72 h) following administration of cisplatin, indicating clear differences between the metabolic profiles, as shown in Fig. 3-4.

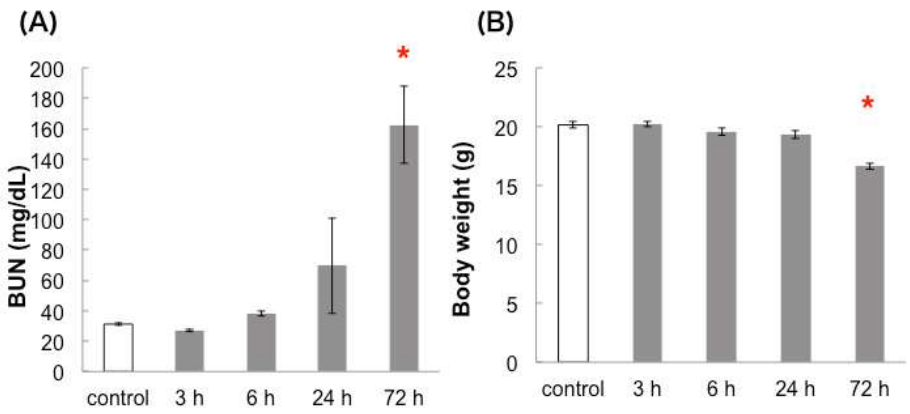

Fig. 3-3 Change of BUN and body weight after cisplatin injection. (A) BUN, (B) Body weight（n = 5, mean±SEM. *; $p<0.05$）

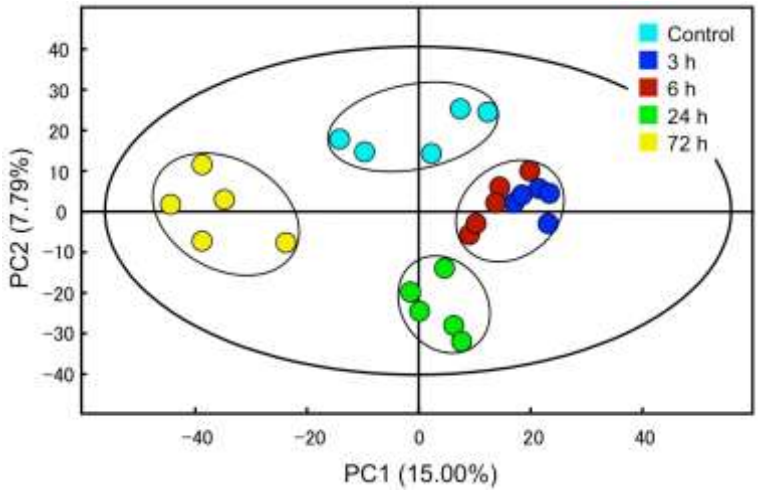

Fig. 3-4 The multivariate analysis of kidney metabolomic changes induced by cisplatin administration. The extracts of control kidney (aqua blue) and cisplatin-treated kidney at 3 h (blue), 6 h (red), 24 h (green) and 72 h (yellow) after cisplatin injection were measured by LC-MS, and the resulting MS spectral data were subjected to an exploratory data analysis (PCA).

Next, the author investigated the variations in each metabolite level in the kidney showing a significant metabolic change in response to disease progression. A student's *t*-test was performed in the kidney tissue metabolite data to compare each of cisplatin treated groups versus the control group. The number of significantly changed metabolites for each of the comparisons is shown in Table 3-1. Metabolites had tendency to increase at early phase, whereas decrease at last phase. The putative metabolites included compounds belonging to amino acid, nucleotide, central, folate, and vitamin metabolism. The majority of amino acid metabolism related metabolites increased in the cisplatin-treated groups compared to control group, whereas the opposite fluctuation was observed at cofactor and sugar metabolism related metabolites. Among nicotinate metabolism related metabolites, nicotinamide-*N*-oxide increased while nicotinamide decreased time-dependently. The majority of central and folate metabolism related metabolites increased at early phase and decreased at late phase, respectively.

To display dynamic variance of metabolic pathway (Fig. 3-5), a quantitative comparison (the ratio of the cisplatin-treated samples to the control samples) of time-dependent metabolite variations in molecules related to glycolysis, TCA cycle, nucleotide and amino acid metabolism in the whole kidney tissue was performed by using LC-MS data not only significantly changed metabolites (Table 3-1) but also no significantly changed metabolites (Table 3-2).

Table 3-1 List of significantly changed putative metabolites in kidney tissue. Fold-change between drug-treated and control group, with their corresponding *p* values. Red is significantly increased and blue is significantly decreased compared to control group ($p < 0.05$).

metabolite	3 h	6 h	24 h	72 h	related pathway	sub-pathway
Asparagine (Asn)	1.53	1.27	1.62	1.55	amino acid	aspartate
Aspartate (Asp)	1.61	1.50	1.45	0.97	amino acid	aspartate
Acetylcarnitine	5.26	9.51	7.34	47.86	amino acid	carnitine
Cysteine-glutathione disulfide	0.69	0.44	0.43	1.47	amino acid	glutathione
Hypotaurine	1.15	1.11	0.93	0.62	amino acid	glutathione
Histidine (His)	1.33	1.52	1.70	1.78	amino acid	glutamate
Hexanoylglycine	1.14	2.10	1.41	3.20	amino acid	glycine
Leucine / Isoleucine (Leu / Ile)	4.16	6.14	5.20	5.43	amino acid	leusine
N-Acetylleucine	1.02	1.96	0.95	3.35	amino acid	leusine
5-Methylthioadenosine (MTA)	2.63	2.47	1.70	0.76	amino acid	methionine
Methionine (Met)	1.39	1.46	1.13	0.68	amino acid	methionine
Phenylacetylglycine	0.29	0.35	0.88	4.00	amino acid	phenylalanine
Phenylalanine (Phe)	1.15	1.30	1.38	1.58	amino acid	phenylalanine
Proline (Pro)	1.34	1.04	1.01	1.64	amino acid	proline
Threonine (Thr)	1.20	0.48	0.86	0.92	amino acid	threonine

Table 3-1 (continue)

metabolite	3 h	6 h	24 h	72 h	related pathway	sub-pathway
3-Nitro-L-tyrosine	1.91	1.88	1.87	0.99	amino acid	tyrosine
L-Adrenaline / 3-(3, 4-Dihydroxyphenyl)-L-alanine (L-DOPA)	1.50	0.64	2.42	0.90	amino acid	tyrosine
Tyrosine (Tyr)	1.46	1.25	1.55	0.98	amino acid	tyrosine
Arginine (Arg)	1.47	1.41	1.09	0.70	amino acid	urea cycle
Creatine	0.95	1.01	1.18	2.45	amino acid	urea cycle
Homoarginine	2.30	2.04	1.38	2.54	amino acid	urea cycle
Phosphocreatine (Creatine-P)	1.15	2.63	0.75	11.65	amino acid	urea cycle
Valine (Val)	1.65	1.84	1.19	0.94	amino acid	valine
2-Phosphoglycerate / 3-Phosphoglycerate (2PG / 3PG)	1.55	1.39	1.13	1.19	central	glycolysis
6-Phosphoglycerate (6PG)	2.02	1.89	1.42	1.29	central	glycolysis
Fructose 6-phosphate (F6P)	1.38	1.12	2.06	0.92	central	glycolysis
Glucose 6-phosphate (G6P)	1.72	1.61	1.74	0.66	central	glycolysis
Glycerol 3-phosphate (Glycerol-3P)	0.75	0.73	0.58	0.59	central	glycolysis
Phosphoenolpyruvate (PEP)	1.92	1.75	1.38	1.40	central	glycolysis

Table 3-1 (continue)

metabolite	3 h	6 h	24 h	72 h	related pathway	sub-pathway
2-Oxoglutarate	0.78	0.73	0.71	0.58	central	TCA cycle
Acetyl coenzyme A (Acetyl-CoA)	1.27	0.95	0.40	0.47	central	TCA cycle
cis-Aconitate	1.51	1.29	0.95	3.63	central	TCA cycle
Oxaloacetate	0.98	0.79	0.78	1.18	central	TCA cycle
Succinate	0.90	0.92	0.70	0.92	central	TCA cycle
Succinyl coenzyme A (Succinyl-CoA)	2.18	2.91	0.86	1.06	central	TCA cycle
Nicotinamide adenine dinucleotide (NAD^+)	0.78	0.76	0.44	0.72	cofactor	nicotinate
Nicotinamide adenine dinucleotide (NADH)	0.22	0.25	0.15	0.69	cofactor	nicotinate
Nicotinamide adenine dinucleotide phosphate ($NADP^+$)	0.91	0.87	0.49	0.78	cofactor	nicotinate
Nicotinamide adenine dinucleotide phosphate (NADPH)	0.72	0.70	0.29	0.27	cofactor	nicotinate
Flavin adenine dinucleotide (FAD)	0.55	0.90	0.16	0.79	cofactor	

Table 3-1 (continue)

metabolite	3 h	6 h	24 h	72 h	related pathway	sub-pathway
5-Methyl tetrahydrofolate (5MeTHF)	1.13	1.09	1.54	0.18	folate	
Folate	1.44	0.91	0.64	0.89	folate	
Tetrahydrofolate	1.34	0.78	0.66	0.63	folate	
1-Methyladenosine	1.04	1.75	1.61	4.01	purine	
5-Aminoimidazole-4-carboxamide ribonucleotide (AICAR)	1.49	1.46	2.02	0.77	purine	
Adenosine	0.00	1.26	1.45	0.82	purine	
Adenosine monophosphate (AMP)	0.85	0.84	0.69	0.95	purine	
Adenosine triphosphate (ATP)	1.30	1.22	1.07	1.09	purine	
Guanosine monophosphate (GMP)	0.94	0.94	0.57	1.22	purine	
Hypoxanthine	1.11	1.03	1.19	0.76	purine	
2'-Deoxyuridine	0.54	0.75	0.16	0.00	pyrimidine	
Deoxyuridine diphosphate (dUDP)	2.41	1.98	2.82	1.62	pyrimidine	
N-Acetylneuraminate (Neu5Ac)	0.84	0.97	1.35	1.44	pyrimidine	

Table 3-1 (continue)

metabolite	3 h	6 h	24 h	72 h	related pathway	sub-pathway
Phosphoethanolamine (PE)	0.70	0.67	0.88	0.87	pyrimidine	
Pseudouridine	1.41	1.98	1.80	3.02	pyrimidine	
Thymidine	1.83	1.43	2.23	0.62	pyrimidine	
Uracil	3.04	3.87	3.13	2.51	pyrimidine	
Uridine	1.96	1.39	1.10	1.25	pyrimidine	
Uridine diphosphate glucose (UDP-glucose)	0.86	0.76	0.61	0.96	pyrimidine	
Uridine diphosphate *N*-acetylglucosamine (UDP-GlcNAc)	0.93	1.07	1.18	1.61	pyrimidine	
Uridine monophosphate (UMP)	0.85	0.79	0.45	1.13	pyrimidine	
Gluconate	1.13	1.12	1.07	0.56	sugar	
Pentose	0.31	0.28	0.42	1.26	sugar	
Nicotinamide	1.32	1.15	1.15	0.64	vitamin	nicotinate
Nicotinamide-*N*-oxide	0.57	0.69	0.65	6.80	vitamin	nicotinate
Cholate	0.05	0.12	0.99	0.83	other	bile acid
Glycerol	2.06	1.37	1.04	0.28	other	
Decreased metabolites	10	13	16	15		
Increased metabolites	24	18	13	12		

Fig. 3-5 Time-dependent metabolic variance after cisplatin injection

Table 3-2 List of putative metabolites in kidney tissue. Fold-change between drug-treated and control group.

metabolite	3 h	6 h	24 h	72 h	related pathway	sub-pathway
Lysine (Lys)	0.92	1.02	1.01	0.83	amino acid	aspartate
Cysteine (Cys)	1.06	1.02	1.50	0.44	amino acid	glutathione
(R)-*S*-Lactoylglutathione	0.61	0.70	0.43	0.56	amino acid	glutathione
O-Acetyl-L-homoserine	0.83	0.85	0.78	1.30	amino acid	glutathione
Serine (Ser)	1.17	1.60	2.23	1.41	amino acid	glutathione
Glutamate (Glu)	0.66	0.83	0.90	0.59	amino acid	glutamate
Glutamine (Gln)	1.16	1.15	1.09	1.18	amino acid	glutamate
Hydroxyproline	1.34	1.13	1.12	0.80	amino acid	glutamate
Methyl histidine	1.12	0.85	1.00	0.91	amino acid	glutamate
5-Hydroxyindoleacetate	0.87	0.44	1.46	0.54	amino acid	tryptophan
N-Acetyltryptophan	0.97	0.69	2.44	5.19	amino acid	tryptophan
Tryptophan (Trp)	1.01	1.06	1.02	1.23	amino acid	tryptophan
5-Aminovalerate	1.02	0.96	1.13	0.71	amino acid	urea cycle
Citrulline	0.94	1.45	0.90	1.09	amino acid	urea cycle
Creatinine	0.88	0.56	1.08	5.19	amino acid	urea cycle
Fructose-bisphosphate (F16P)	2.39	1.34	1.21	1.32	central	glycolysis
Glucose 1-phosphate (G1P)	1.74	1.27	2.22	1.95	central	glycolysis
Pyruvate (PYR)	1.16	0.97	0.35	1.20	central	glycolysis

Table 3-2 (continue)

metabolite	3 h	6 h	24 h	72 h	related pathway	sub-pathway
Citrate / Isocitrate	1.03	0.80	1.12	1.45	central	TCA cycle
Fumarate	1.10	1.10	1.22	0.67	central	TCA cycle
Malate	1.04	1.05	1.07	0.83	central	TCA cycle
Choline	0.55	0.90	0.84	0.76	choline	
Glycero phosphoryl choline (GPC)	0.95	1.26	0.95	1.38	choline	
3-Hydroxybutyrate (BHBA)	0.76	1.47	1.22	0.70	fatty acid	
Ribose 5-phosphate (R5P)	2.00	1.37	1.14	0.77	pentose phosphate	
Riburose 5-phosphate (Ribu5P)	1.06	0.93	0.99	1.03	pentose phosphate	
Sedoheptulose 7-phosphate (S7P)	1.00	1.05	0.89	0.59	pentose phosphate	
Xylulose 5-phosphate (X5P)	1.10	1.04	0.98	0.92	pentose phosphate	
Adenosine diphosphate (ADP)	1.06	1.07	0.86	0.92	purine	
Adenosine diphosphate ribose (ADP-ribose)	0.63	0.53	0.37	0.81	purine	
Allantoin	0.99	0.78	0.92	0.97	purine	

Table 3-2 (continue)

metabolite	3 h	6 h	24 h	72 h	related pathway	sub-pathway
Deoxyadenosine	0.04	0.11	0.22	0.00	purine	
Deoxyadenosine monophosphate (dAMP)	0.85	0.80	0.91	0.60	purine	
Guanosine	1.15	0.74	1.12	0.47	purine	
Guanosine diphosphate (GDP)	1.28	1.48	0.98	1.27	purine	
Inosine monophosphate (IMP)	0.40	0.56	0.44	1.28	purine	
Xanthine	1.36	1.13	1.30	1.09	purine	
5-Methylcytidine	1.13	0.97	1.55	1.32	pyrimidine	
Cytidine diphosphocholine (CDP-choline)	0.78	0.89	1.27	1.33	pyrimidine	
Cytidine monophosphate (CMP)	0.77	0.67	0.67	1.25	pyrimidine	
Uridine diphosphate (UDP)	0.75	0.86	0.78	1.22	pyrimidine	
Pentitol	1.32	2.21	3.62	2.32	sugar	sugar alcohol
N-Acetylglucosamine (GlcNAc)	1.13	0.89	0.74	0.45	sugar	
Xylonate	1.59	1.12	1.14	2.07	sugar	
Riboflavin	0.67	0.87	0.78	0.49	vitamin	vitamin B2
Phosphate	1.23	1.18	1.26	0.83	other	

3.3.3 Spatiotemporal metabolic variance in kidney visualized by MSI

To investigate spatially-resolved metabolic dynamics in micro-regions of the kidney, the author used kidney tissue sections for MALDI-MSI, which enabled us to simultaneously detect multiple biomolecules with two-dimensional local information (Miura et al. 2010a). The averaged mass spectrum data of normal and cisplatin exposure mouse kidney section showed more than 90 metabolite peaks, respectively (Table 3-1, 3-2). Among metabolite peaks detected in the present study, more than 15 metabolites, including nucleotides, cofactors, phosphorylated sugars, amino acids, lipids, and carboxylic acid, were successfully identified by comparison with MS/MS spectra of standard compounds or with online databases. These metabolites were simultaneously detected, and their unique distribution variance among chronogical mouse kidneys after cisplatin injection was visualized with a 50 μm spatial resolution (Fig. 3-6, 3-7, 3-8). In control mouse kidney, hexose monophosphate, AMP, IMP, and UDP-hexose were mainly distributed at medulla, while diphosphoglycerate, UMP, ATP, cyclic ADP-ribose and NADH were presented at cortex. The amount of ADP-ribose and lipids (phosphatidylcholine and phosphatidylinositol) increased in cisplatin treated kidneys (ADP-ribose; 6 and 24 h, lipids; 3-72 h) compared with the control kidney. On the other hand reduced level of NADH, cyclic ADP-ribose was observed after cisplatin injection. Moreover, ATP and ADP decreased in the medullar after 6 h injection.

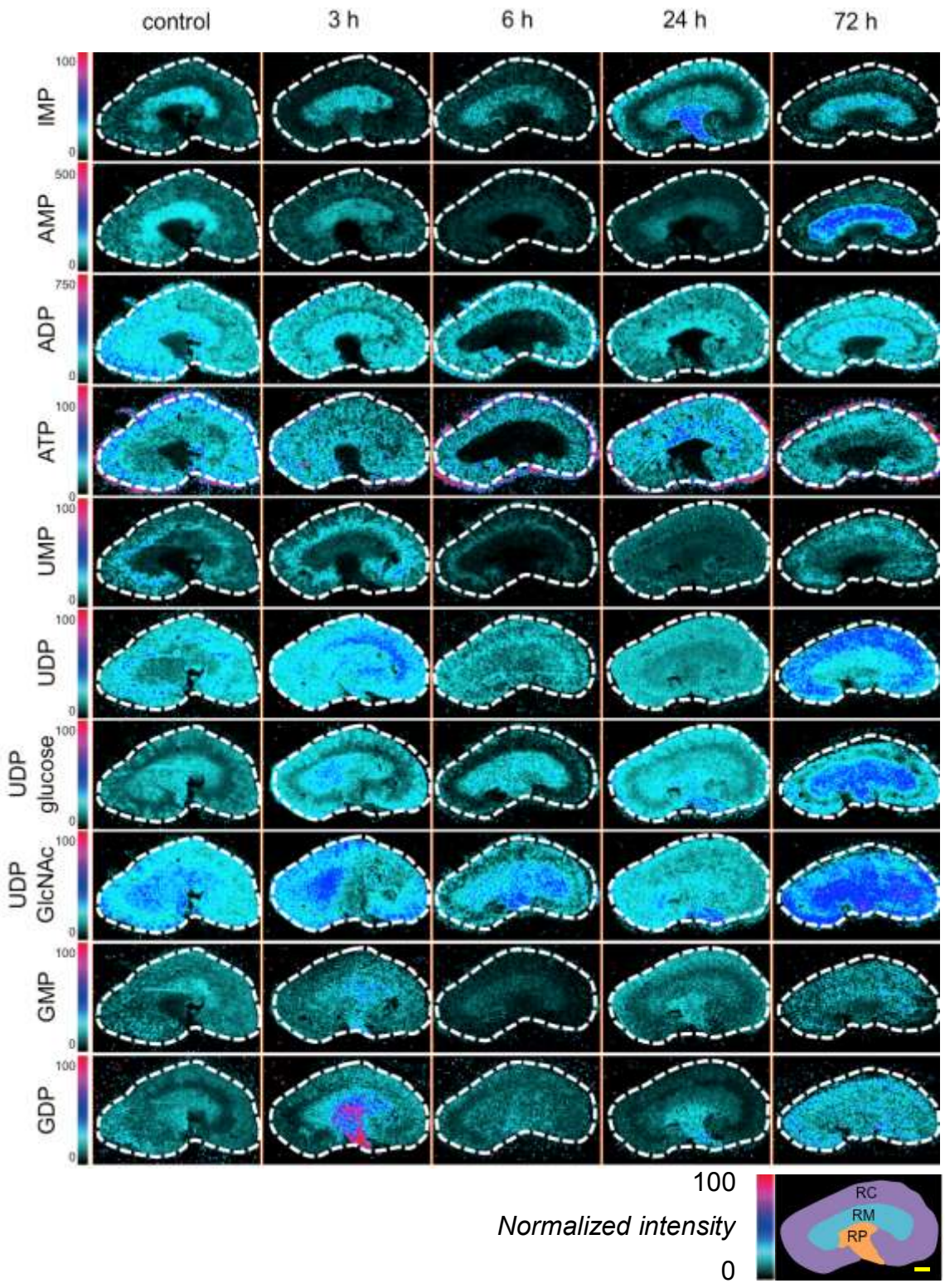

Fig. 3-6 Visualization of spatiotemporal distribution of renal metabolites related to nucleotide metabolism after cisplatin injection by MSI. RC; renal cortex, RM; renal medulla, RP; renal pelvis. Scale bar = 1.0mm.

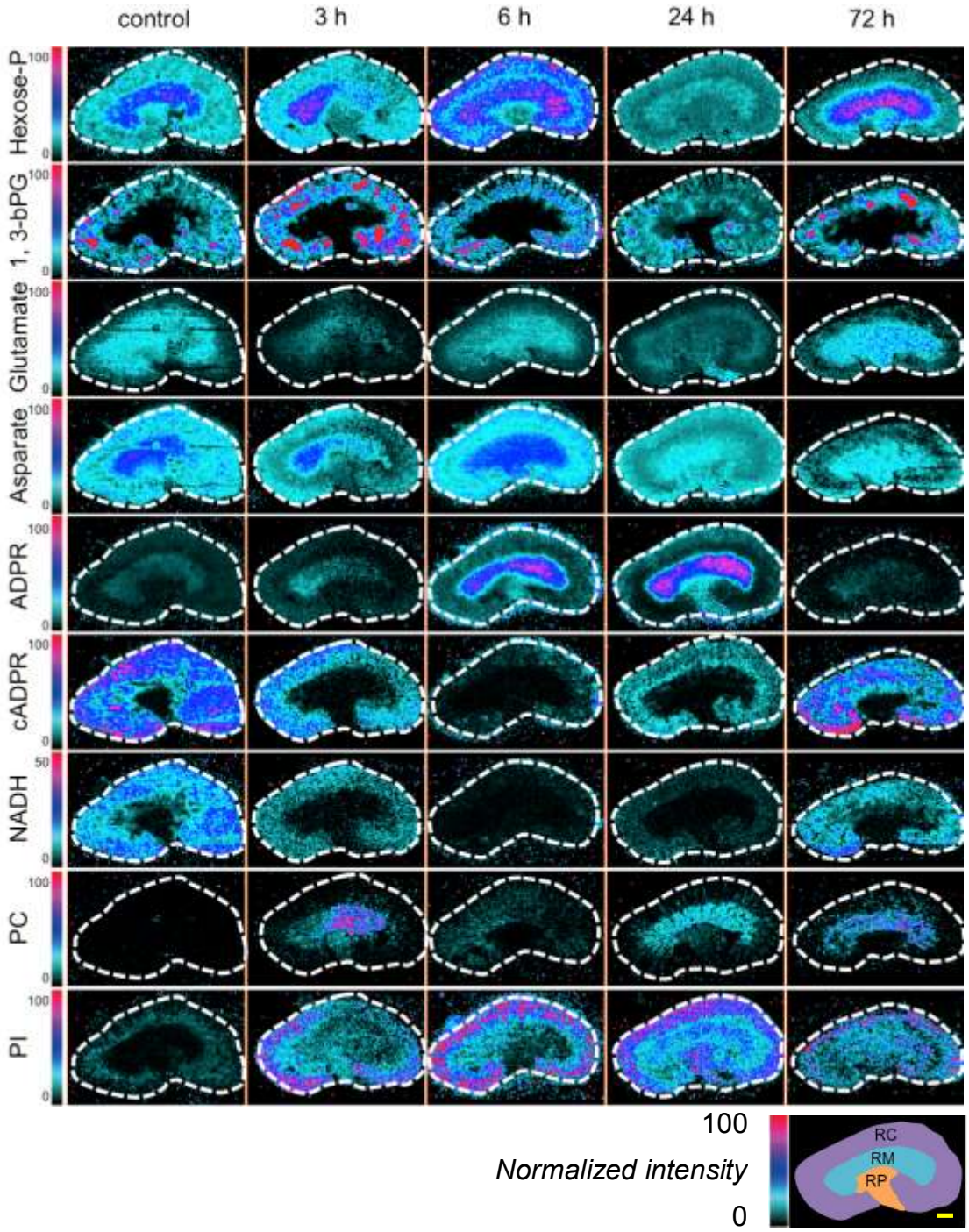

Fig. 3-7 Visualization of spatiotemporal distribution of renal metabolites related to amino acid, glycolysis and lipid metabolism after cisplatin injection by MSI. RC; renal cortex, RM; renal medulla, RP; renal pelvis. Scale bar = 1.0mm.

Fig. 3-8 Integrated LC-MS and MSI technique visualizes drastic changes of spatiotemporal metabolite distribution in mouse kidney after cisplatin injection.

3.4 Discussion

Clinical chemistry measurements found that higher BUN and lower body weight were present at 72 h after cisplatin administration. However, no other treated groups had elevated BUN and decreased body weight. This finding is not surprising, since the commonly used BUN and body weight measurements are not very sensitive markers for nephrotoxicity (Mukhopadhyay et al. 2012; Wei et al. 2007; Portilla et al. 2006; Sheikh-Hamad et al. 2004; Okui et al. 2012; Boudonck et al. 2009). Usually by the time changes in BUN and body weight levels are detected, significant damage to the nephrons has already occurred. Thus, elucidation of early response mechanism against cisplatin in kidney is clearly needed. Such evaluation of early response would indicate when the damage begins, exploits new biomarker for assessment of damage level, and be useful to develop nephrotoxicity of therapeutic agents in preclinical drug development and phase I drug trials. The author used metabolomics to identify changes in metabolites from kidney upon dosing with cisplatin-induced nephropathy and one control. The author showed that metabolic profile compared with control was significantly different from not only last stage but also early and intermediate stage.

A series of relevant observations indicate that cisplatin can cause DNA damage (Miller et al. 2010). DNA damage triggers a series of adaptive and repair mechanisms including the activation of poly ADP-ribose polymerase (PARP). PARP has a dual role in response to DNA damage. It recognizes DNA breaks and binds to histones at the damaged site. Poly-ADP-ribosylation of histones destabilizes the chromatin structure and makes it accessible to DNA repair enzymes thereby initiating the assembly of the DNA repair complex

(Lindahl et al. 1995) (Fig. 3-9). Whereas PARP participates in averting cell damage, its excessive activation can have deleterious effect, as well. This is due to an abnormally increased consumption of NAD^+ that PARP uses for building up poly (ADP-ribose) chains. This activity leads to depletion of cellular NAD^+, and subsequently ATP resulting in metabolic collapse and eventually in cell death (Virág et al. 1998; Szabó et al. 1996; Cepeda et al. 2007; Schreiber et al. 2006; Javle and Curtin 2011) (Fig. 3-10). In the present study, decrease of NAD^+ level was confirmed just after cisplatin administration by LC-MS (Table 3-1). Hence NAD^+, related for DNA repair, may be varied due to DNA repair by cisplatin-induced DNA damage at 24 h. In addition, intermediates of folate metabolism, related nucleic metabolism, were increased from 3 h to 24 h after cisplatin administration (Table 3-1). This variance possibly produced nucleic acids for DNA repair. In spite of decreasing rate of ADP-ribose at LC-MS data (Table 3-1), MSI visualized accumulation of ADP-ribose in outer medullar at 6 and 24 h after cisplatin injection (Fig. 3-7). It is known that after repairing, the poly ADP-ribose chains are degraded via poly ADP-ribose glycohydrolase (PARG) (Isabelle et al. 2010), and pathological changes in cisplatin-induced nephrotoxicity occur mainly at the S3 segment of the proximal tubule in the outer stripe of the outer medulla (Yalcin et al. 2003; Los et al. 1990). Assuming that the DNA repair occurred in the S3 segment of the proximal tubule due to recovery for cisplatin-induced DNA damage and the poly ADP-ribose chains was degraded to mono ADP-ribose after DNA repair in most serious damaged region (outer medullar), it is not unreasonable to speculate that ADP-ribose accumulates at outer medullar for DNA repair.

In contrast, concentration of ATP remarkably decreased in kidney medullar at 6 h (Fig. 3-7). However, its concentration of extracted metabolite from the whole kidney significantly

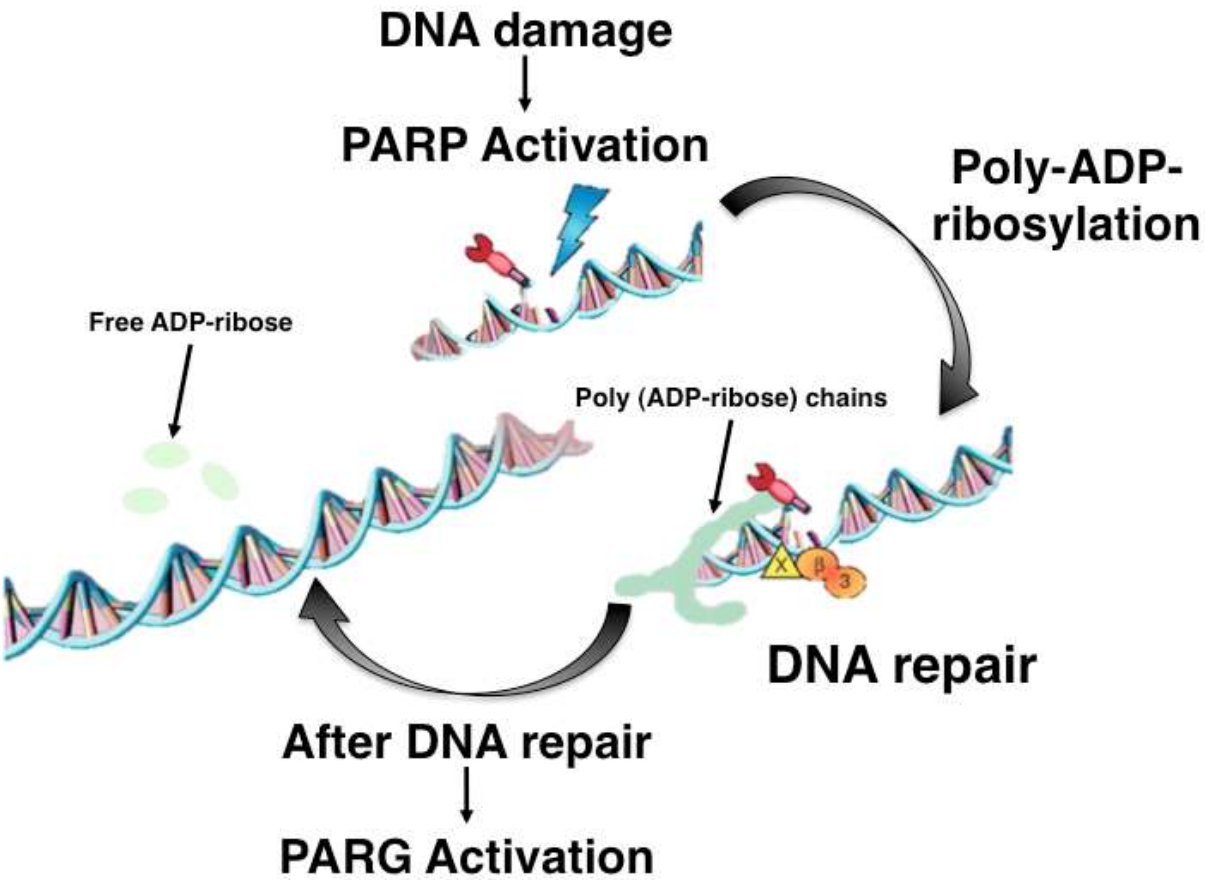

Fig. 3-9 Catalytic activity of poly ADP-ribose polymerase (PARP) and role in DNA damage. PARP cleaves NAD^+ releasing nicotinamide; the ADP-ribose polymers are covalently attached to acceptor proteins, such as PARP itself and histones. These loosen the chromatin and recruit the scaffold protein (X) and other histone remodelling enzymes, which in turn recruits DNA polymerase (β) and ligase III (3) to fill in and re-seal the gap. The polymers are degraded by poly ADP-ribose glycohydrolase (PARG), releasing unmodified PARP to bind other DNA breaks.

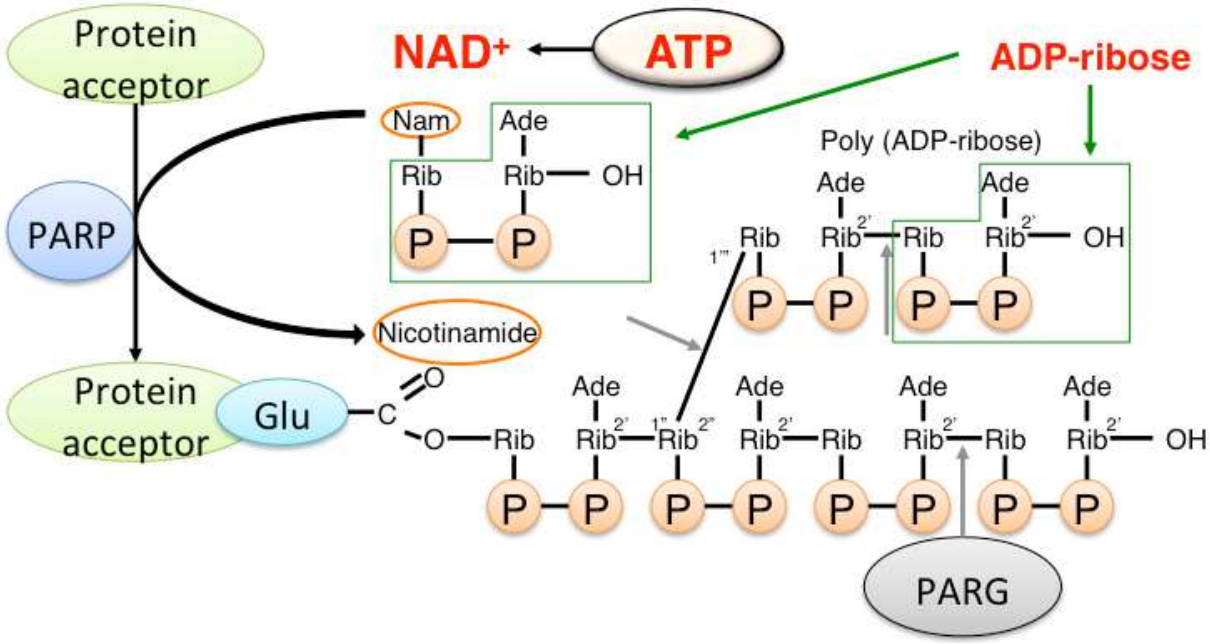

Fig. 3-10 Metabolism of poly ADP-ribose during DNA damage and repair (Schreiber et al. 2006)**.** In response to DNA-strand breaks, DNA-damage-dependent poly ADP-ribose polymerases hydrolyse NAD+, releasing nicotinamide (Nam) and one proton (H^+), and catalyse the successive transfer of the ADP-ribose moiety to nuclear protein acceptors that might be transiently inactivated. The reaction is initiated by the formation of an ester bond between the amino-acid acceptor (Glu, Asp or COOH-Lys) and the first ADP-ribose; polymer elongation involves the catalysis of a 2′-1′′ glycosidic bond; polymer branching occurs on average after 20 ADP-ribose units and branching points are located at regular distances (every 40–50 ADP-ribose units). The same chemistry is used during the elongation and branching reactions because of the equivalent orientation of the 2′-OH of the riboses relative to the Ade (in the elongation mode) or to the Nam (in the branching mode) of NAD^+. The degradative nuclear enzyme poly ADP-ribose glycohydrolase (PARG) has endo- and exoglycolytic activities that cleave glycosidic bonds between ADP-ribose units. P, phosphate; Rib, ribose.

increased at 3 and 6 h after cisplatin injection (Table 3-1). It is assumed that cisplatin indirectly induced overexpression of ATP generation at penumbra of outer medullar for many utilized ATP reaction such as DNA repair at most serious damaged region (outer medullar), leading to overproduction of ROS. Generally, cisplatin-induced nephrotoxicity is known that increased oxidative stress. Moreover, overexpression of ATP synthase after drug injection was already reported (Perez et al. 2011). These results suggested that cisplatin-induced DNA damage may possibly promote overproduction of ATP and ROS, leading to irreversible serious injury for all over the kidney. In brief, nephropathy will progress by the interaction between most serious damaged region and its penumbra region.

Although the date reported that the maximal cisplatin-DNA adducts level in kidney tissue was reached at 30 min after drug injection, followed by a steady state lasting for at least 24 h (Johnsson et al. 1995), in the present study, accumulation of ADP-ribose and reduction of ATP in outer medullar, most serious cisplatin damaged region, was confirmed not at 3 and 72 h but at 6 and 24 h (only ADP-ribose) after drug exposure (Table 3-1, 3-2). Moreover, most remarkable depletion of NAD^+ was occurred at 24 h (Table 3-1). It is known that with increasing levels of DNA damage the cell switches from DNA repair to apoptosis (Bernstein et al. 2002). Therefore, these result may suggest that DNA damage and repair most remarkably performed following 6 h after drug administration, apoptosis and necrosis probably progressed more than DNA repair in kidney at 72 h and, DNA damage and repair all over the kidney may probably hardly occur at least following 3 h after cisplatin administration.

As other variance at early stage, the accumulation of lipids at medullar was confirmed from just after cisplatin administration. Moreover, almost all amino acids, related protein

construction, also relatively increased at 3 h after cisplatin administration (Table 3-1, 3-2, Fig. 3-5). When cisplatin passes trough the cell membrane, the cisplatin center may coordinate to some constituents of the lipidic bilayer, which contain nitrogen and sulphur atoms including phospholipids and phosphatidylserine, thus leasing to injury of plasma membranes (Cepeda et al. 2007). Moreover, only 5-10% of covalently bound cell-associated cisplatin is found in the DNA, whereas 75-85% of the drug binds to proteins and other cellular constituents (Cepeda et al. 2007). Therefore, a lot of cisplatin bind to protein rather than DNA, and cisplatin may alter the structure and activity of enzymes, receptors, and other proteins and finally accumulate abnormal proteins in kidney. Generally, abnormal proteins are treated by photolytic enzymes and degraded to amino acids. Therefore, level of lipid and amino acid may increase from just after cisplatin exposure due to degradation of protein and cell membrane. These variance were confirmed from 3 h after cisplatin injection, and protein and cell membrane degradation may possibly be important factors, leading to cell death.

3.5 Concluding Remarks

In the present study, the author was able to visualize diverse spatiotemporal metabolic dynamics within the central metabolic pathway and its periphery in mouse kidney after cisplatin injection using an integrated technique combining MSI with LC-MS (Fig. 3-8). The author indicated very early response against cisplatin that can vary tubular kidney damage much earlier than BUN measurement. In addition, our analysis validated some of the earlier published mechanism of cisplatin-induced nephropathy, but it highlighted that many metabolites at early kidney malfunction are in fact different variance with last stage. Moreover, the author hypothesized new mechanism of disease progression in cisplatin-induced acute kidney injury. Our future efforts will be focused on the validation of those variance, and expansion of test panel of nephrotoxins to include other mechanisms of action. Elucidation of early stage for cisplatin-induced nephropathy may have a beneficial effect on cisplatin therapy of malignant tumor by reducing tis side effects.

CHAPTER 4

Final remarks

In the present study, the author developed technique of combining comprehensive and quantitative method (LC-MS based metabolomics) and spatiotemporal metabolic valiance method (MSI), and applied this technique to several disease models. LC-MS has been used for the metabolomic studies due to their high coverage (more than several hundred metabolites) and ability to provide quantification (Dunn and Ellis 2005; Werner et al. 2008; Pohjanen et al. 2007). On the other hand, MSI enables the determination of the distribution of biomolecules present in tissue sections by direct ionization and detection (Caprioli et al. 1997; Miura et al. 2012). As a result, the author succeeded in indication of metabolic variance according to disease levels.

This new approach combining MSI (spatial information but low coverage) and its complementary technique LC-MS (high coverage but loss of spatial information) will provide insight into the understanding of the complex pathological mechanism(s) of ischemia-reperfusion and acute kidney injury. This could be broadly applicable to emerging issues in the precise pathological evaluation of target tissues in both preclinical and clinical settings, and may become a compulsory technique for *in situ* pharmacometabolomics and biomarker discovery.

Until now, several pathological mechanisms were proposed for various pathologies. However, pathological mechanism considering the interaction between regions in the same tissue or organ is probably not exists. Therefore, elucidation of interaction between regions in the same tissue or organ using MS-coupled technique may enable us to prevent disease progression. In brief, this may be predicted to lead to the development of new pharmacy and establishment of new therapy method by reveal the new biological mechanism using this technique.

Moreover, this technique can apply not only to disease sample but also other samples such as animal samples of functional food administration and plant samples. Therefore, it may become useful technique in agricultural field as well as medical and pharmaceutical field.

References

Abe, K., Araki, T., Kogure, K. (1988) "Recovery from edema and of protein synthesis differs between the cortex and caudate following transient focal cerebral ischemia in rats." *J. Neurochem.*, **51** (5), 1470–1476.

Amstalden van Hove, E.R., Smith, D.F., Heeren, R.M. a (2010) "A concise review of mass spectrometry imaging." *J. Chromatogr. A*, **1217** (25), 3946–3954.

Arany, I., Safirstein, R.L. (2003) "Cisplatin nephrotoxicity." *Semin. Nephrol.*, **23** (5), 460–464.

Bajorin, D.F., Bosl, G.J., Alcock, N.W., Saline, H., Itosi, G.J., Niedzwiecki, D., Gallina, E., Shurgot, B. (1986) "Pharmacokinetics of cis -Diamminedichloroplatinum (II) after Administration in Hypertonic Saline." *Cancer Res.*, **46** (11), 5969–5972.

Bell, D.S., Jones, a. D. (2005) "Solute attributes and molecular interactions contributing to 'U-shape' retention on a fluorinated high-performance liquid chromatography stationary phase." *J. Chromatogr. A*, **1073** (1-2), 99–109.

Beran, J., Kevanl, L. (1969) "Molecular Electron Ionization Cross Sections at 70 eV." *J. Phys. Chem.*, **73** (11), 3866–3876.

Bernstein, C., Bernstein, H., Payne, C.M., Garewal, H. (2002) *DNA repair/pro-apoptotic dual-role proteins in five major DNA repair pathways: fail-safe protection against carcinogenesis.*,

Bijlsma, S., Bobeldijk, I., Verheij, E.R., Ramaker, R., Kochhar, S., Macdonald, I. a, van Ommen, B., Smilde, A.K. (2006) "Large-scale human metabolomics studies: a strategy for data (pre-) processing and validation." *Anal. Chem.*, **78** (2), 567–574.

Blanc, C., Deveraux, Q.L., Krajewski, S., Ja, R.U., Porter, A.G., Reed, J.C., Jaggi, R., Marti, A. (2000) "Caspase-3 Is Essential for Procaspase-9 Processing and Cisplatin-induced Apoptosis of MCF-7 Breast Cancer Cells." *Cancer Res.*, **60** (16), 4386–4390.

Boudonck, K.J., Mitchell, M.W., Német, L., Keresztes, L., Nyska, A., Shinar, D., Rosenstock, M. (2009) "Discovery of metabolomics biomarkers for early detection of nephrotoxicity." *Toxicol. Pathol.*, **37** (3), 280–292.

Bouhifd, M., Hartung, T., Hogberg, H.T., Kleensang, A., Zhao, L. (2013) "Review: toxicometabolomics." *J. Appl. Toxicol.*, **33** (12), 1365–1383.

Bristow, A.W.T., Webb, K.S., Lubben, A.T., Halket, J. (2004) "Reproducible product-ion tandem mass spectra on various liquid chromatography/mass spectrometry instruments for the development of spectral libraries." *Rapid Commun. Mass Spectrom.*, **18** (13), 1447–1454.

Bromont, C., Marie, C., Bralet, J. (1989) "Increased lipid peroxidation in vulnerable brain regions after transient forebrain ischemia in rats." *Stroke*, **20** (7), 918–924.

Bylund-Fellenius, A., Ojamaa, K., Flaim, K., Li, J., Wassner, S., Jefferson, L. (1984) "Protein synthesis versus energy state in contracting muscles of perfused rat hindlimb." *Am. J. Physiol.*, **246**, E297–305.

Byrdwell, W.C. (2001) "Atmospheric pressure chemical ionization mass spectrometry for analysis of lipids." *Lipids*, **36** (4), 327–346.

Cai, F., Xu, W., Wei, H., Sun, L., Gao, S., Yang, Q., Feng, J., Zhang, F., Chen, W. (2010) "Simultaneous determination of active xanthone glycosides, timosaponins and alkaloids in rat plasma after oral administration of Zi-Shen Pill extract for the pharmacokinetic study by liquid chromatography-tandem mass spectrometry." *J. Chromatogr. B. Analyt. Technol. Biomed. Life Sci.*, **878** (21), 1845–1854.

Caprioli, R.M., Farmer, T.B., Gile, J. (1997) "Molecular imaging of biological samples: localization of peptides and proteins using MALDI-TOF MS." *Anal. Chem.*, **69** (23), 4751–4760.

Cepeda, V., Fuertes, M. a, Castilla, J., Alonso, C., Quevedo, C., Pérez, J.M. (2007) "Biochemical mechanisms of cisplatin cytotoxicity." *Anticancer. Agents Med. Chem.*, **7** (1), 3–18.

Chen, Z., Seimiya, H., Naito, M., Mashima, T., Kizaki, A., Dan, S., Imaizumi, M., Ichijo, H., Miyazono, K., Tsuruo, T. (1999) "ASK1 mediates apoptotic cell death induced by genotoxic stress." *Oncogene*, **18** (1), 173–180.

Cornelison, T., Reed, E. (1993) "Nephrotoxicity and Hydration Management for Cisplatin, Carboplatin, and Ormaplatin." *Gynecol Oncol.*, **50** (2), 147–158.

Crawford, L., Morrison, J. (1968) "Computer Methods in Analytical Mass Spectrometry Identification of an Unknown Compound in a Catalog." *Anal. Chem.*, **40** (10), 1464–1469.

Dale, S., CornettSara, L., FrappierRichard, M., Caprioli (2008) "MALDI-FTICR Imaging Mass Spectrometry of Drugs and Metabolites in Tissue." *Anal. Chem.*, **80** (14), 5648–5653.

Davis, C. a, Nick, H.S., Agarwal, A. (2001) "Manganese superoxide dismutase attenuates Cisplatin-induced renal injury: importance of superoxide." *J. Am. Soc. Nephrol.*, **12** (12), 2683–2690.

Dettmer, K., Aronov, P.A., Hammock, B.D. (2007) "MASS SPECTROMETRY-BASED METABOLOMICS." *Mass Spectrom. Rev.*, 51–78.

Dunn, W.B., Bailey, N.J.C., Johnson, H.E. (2005) "Measuring the metabolome: current analytical technologies." *Analyst*, **130** (5), 606–625.

Dunn, W.B., Ellis, D. (2005) "Metabolomics: Current analytical platforms and methodologies." *TrAC Trends Anal. Chem.*, **24** (4), 285–294.

Ellis, D.I., Dunn, W.B., Griffin, J.L., Allwood, J.W., Goodacre, R. (2007) "Metabolic fingerprinting as a diagnostic tool." *Pharmacogenomics*, **8** (9), 1243–1266.

Euerby, M.R., McKeown, A.P., Petersson, P. (2003) "Chromatographic classification and comparison of commercially available perfluorinated stationary phases for reversed-phase liquid chromatography using Principal Component Analysis." *J. Sep. Sci.*, **26** (3-4), 295–306.

Farag, M. a, Huhman, D. V, Lei, Z., Sumner, L.W. (2007) "Metabolic profiling and systematic identification of flavonoids and isoflavonoids in roots and cell suspension cultures of Medicago truncatula using HPLC-UV-ESI-MS and GC-MS." *Phytochemistry*, **68** (3), 342–354.

Fiehn, O. (2001) “Combining genomics, metabolome analysis, and biochemical modelling to understand metabolic networks.” *Comp. Funct. Genomics*, **2** (3), 155–168.

Fiehn, O. (2002) “Metabolomics--the link between genotypes and phenotypes.” *Plant Mol. Biol.*, **48** (1-2), 155–171.

Fiehn, O., Kopka, J., Trethewey, R.N., Willmitzer, L. (2000) “Identification of uncommon plant metabolites based on calculation of elemental compositions using gas chromatography and quadrupole mass spectrometry.” *Anal. Chem.*, **72** (15), 3573–3580.

Gonzalez, B., François, J., Renaud, M. (1997) “A rapid and reliable method for metabolite extraction in yeast using boiling buffered ethanol.” *Yeast*, **13** (14), 1347–1355.

Green, A. (2008) “Pharmacological approaches to acute ischaemic stroke: reperfusion certainly, neuroprotection possibly.” *Br. J. Pharmacol.*, **153** (S1), S325–S338.

Griffin, J.L., Shockcor, J.P. (2004) “Metabolic profiles of cancer cells.” *Nat. Rev. Cancer*, **4** (7), 551–561.

Hankin, J. a, Barkley, R.M., Murphy, R.C. (2007) “Sublimation as a method of matrix application for mass spectrometric imaging.” *J. Am. Soc. Mass Spectrom.*, **18** (9), 1646–1652.

Hattori, K., Kajimura, M., Hishiki, T., Nakanishi, T., Kubo, A., Nagahata, Y., Ohmura, M., Yachie-Kinoshita, A., Matsuura, T., Morikawa, T., Nakamura, T., Setou, M., Suematsu, M. (2010) “Paradoxical ATP elevation in ischemic penumbra revealed by quantitative imaging mass spectrometry.” *Antioxid. Redox Signal.*, **13** (8), 1157–1167.

Hermansson, M., Uphoff, A., Käkelä, R., Somerharju, P. (2005) “Automated quantitative analysis of complex lipidomes by liquid chromatography/mass spectrometry.” *Anal. Chem.*, **77** (7), 2166–2175.

Holmes, E., Wilson, I.D., Nicholson, J.K. (2008) “Metabolic phenotyping in health and disease.” *Cell*, **134** (5), 714–717.

Irie, M., Fujimura, Y., Yamato, M., Miura, D., Wariishi, H. (2013) “Integrated MALDI-MS imaging and LC–MS techniques for visualizing spatiotemporal metabolomic dynamics in a rat stroke model.” *Metabolomics*.

Isabelle, M., Moreel, X., Gagné, J.-P., Rouleau, M., Ethier, C., Gagné, P., Hendzel, M.J., Poirier, G.G. (2010) "Investigation of PARP-1, PARP-2, and PARG interactomes by affinity-purification mass spectrometry." *Proteome Sci.*, **8**, 22.

Javle, M., Curtin, N.J. (2011) "The role of PARP in DNA repair and its therapeutic exploitation." *Br. J. Cancer*, **105** (8), 1114–1122.

Johnsson, A., Olsson, C., Nygren, O., Nilsson, M., Seiving, B., Cavallin-Stahl, E. (1995) "Pharmacokinetics and tissue distribution of cisplatin in nude mice: platinum levels and cisplatin-DNA adducts." *Cancer Chemother. Pharmacol.*, **37** (1-2), 23–31.

Jonsson, P., Bruce, S.J., Moritz, T., Trygg, J., Sjöström, M., Plumb, R., Granger, J., Maibaum, E., Nicholson, J.K., Holmes, E., Antti, H. (2005) "Extraction, interpretation and validation of information for comparing samples in metabolic LC/MS data sets." *Analyst*, **130** (5), 701–707.

Jung, J.Y., Lee, H.-S., Kang, D.-G., Kim, N.S., Cha, M.H., Bang, O.-S., Ryu, D.H., Hwang, G.-S. (2011) "1H-NMR-based metabolomics study of cerebral infarction." *Stroke*, **42** (5), 1282–1288.

Katajamaa, M., Oresic, M. (2007) "Data processing for mass spectrometry-based metabolomics." *J. Chromatogr. A*, **1158** (1-2), 318–328.

Kinross, J.M., Holmes, E., Darzi, A.W., Nicholson, J.K. (2011) "Metabolic phenotyping for monitoring surgical patients." *Lancet*, **377** (9780), 1817–1819.

Kitagawa, K., Matsumot, M., Yang, G., Mabuchi, T., Yagita, Y., Hori, M., Yanagihara, T. (1998) "Cerebral Ischemia After Bilateral Carotid Artery Occlusion and Intraluminal Suture Occlusion in Mice : Evaluation of the Patency of the Posterior Communicating Artery." *J. Cereb. Blood Flow Metab.*, **18**, 570–579.

Ladanyi, A., Sipos, F., Szoke, D., Galamb, O. (2006) "Laser Microdissection in Translational and Clinical Research." *Cytom. Part A*, **69** (9), 947–960.

Lee, S., Moon, S.-O., Kim, W., Sung, M.J., Kim, D.H., Kang, K.P., Jang, Y.B., Lee, J.E., Jang, K.Y., Lee, S.Y., Park, S.K. (2006) "Protective role of

L-2-oxothiazolidine-4-carboxylic acid in cisplatin-induced renal injury." *Nephrol. Dial. Transplant.*, **21** (8), 2085–2095.

Lei, Z., Huhman, D. V, Sumner, L.W. (2011) "Mass spectrometry strategies in metabolomics." *J. Biol. Chem.*, **286** (29), 25435–25442.

Lenz, E.M., Bright, J., Knight, R., Wilson, I.D., Major, H. (2004) "Cyclosporin A-induced changes in endogenous metabolites in rat urine: a metabonomic investigation using high field 1H NMR spectroscopy, HPLC-TOF/MS and chemometrics." *J. Pharm. Biomed. Anal.*, **35** (3), 599–608.

Lindahl, T., Satoh, M.S., Poider, G.G., Klungland, A. (1995) "Post-translational modification of poly(ADP-ribose)polymerase induced by DNA strand breaks." *Trends Biochem. Sci.*, **20** (10), 405–411.

Lipton, P. (1999) "Ischemic cell death in brain neurons." *Physiol. Rev.*, **79** (4), 1431–1568.

Los, G., Mutsaers, P.H., Lenglet, W.J., Baldew, G.S., McVie, J.G. (1990) "Platinum distribution in intraperitoneal tumors after intraperitoneal cisplatin treatment." *Cancer Chemother. Pharmacol.*, **25** (6), 389–394.

Maharjan, R.P., Ferenci, T. (2003) "Global metabolite analysis: the influence of extraction methodology on metabolome profiles of Escherichia coli." *Anal. Biochem.*, **313** (1), 145–154.

Mandic, A., Viktorsson, K., Molin, M., Akusjärvi, G., Eguchi, H., Hayashi, S., Toi, M., Hansson, J., Linder, S., Maria, C. (2001) "Cisplatin Induces the Proapoptotic Conformation of Bak in a Δ MEKK1-Dependent Manner." *Mol. Cell. Biol.*, **21** (11), 3684–3691.

Marchand, D.H., Croes, K., Dolan, J.W., Snyder, L.R., Henry, R. a., Kallury, K.M.R., Waite, S., Carr, P.W. (2005) "Column selectivity in reversed-phase liquid chromatography." *J. Chromatogr. A*, **1062** (1), 65–78.

Martin, J. (2003) *Neuroanatomy: Text and Atlas.*, New York: McGraw-Hill Companies,Inc.

Matsumoto, K., Graf, R., Rosner, G., Taguchi, J., Heiss, W.D. (1993) “Elevation of neuroactive substances in the cortex of cats during prolonged focal ischemia.” *J. Cereb. blood flow Metab.*, **13** (4), 586–594.

Memezawa, H, Minamisawa, H., Smith, M.., Siesjo, B.. (1992) “Ischemic penumbra in a model of reversible middle cerebral artery.” *Exp. Brain Reserch*, **89** (1), 67–78.

Memezawa, H., Smith, M.L., Siesjo, B.K. (1992) “Penumbral tissues salvaged by reperfusion following middle cerebral artery occlusion in rats.” *Stroke*, **23** (4), 552–559.

Mese, H., Sasaki, A., Nakayama, S., Alcalde, R.E., Matsumura, T. (2000) “The role of caspase family protease, caspase-3 on cisplatin-induced apoptosis in cisplatin-resistant A431 cell line.” *Cancer Chemother. Pharmacol.*, **46** (3), 241–245.

Miller, R.P., Tadagavadi, R.K., Ramesh, G., Reeves, W.B. (2010) “Mechanisms of Cisplatin nephrotoxicity.” *Toxins (Basel).*, **2** (11), 2490–2518.

Miura, D., Fujimura, Y., Tachibana, H., Wariishi, H. (2010b) “Highly sensitive matrix-assisted laser desorption ionization-mass spectrometry for high-throughput metabolic profiling.” *Anal. Chem.*, **82** (2), 498–504.

Miura, D., Fujimura, Y., Wariishi, H. (2012) “In situ metabolomic mass spectrometry imaging: recent advances and difficulties.” *J. Proteomics*, **75** (16), 5052–5060.

Miura, D., Fujimura, Y., Yamato, M., Hyodo, F., Utsumi, H., Tachibana, H., Wariishi, H. (2010a) “Ultrahighly sensitive in situ metabolomic imaging for visualizing spatiotemporal metabolic behaviors.” *Anal. Chem.*, **82** (23), 9789–9796.

Mukhopadhyay, P., Horváth, B., Zsengellér, Z., Zielonka, J., Tanchian, G., Holovac, E., Kechrid, M., Patel, V., Stillman, I.E., Parikh, S.M., Joseph, J., Kalyanaraman, B., Pacher, P. (2012) “Mitochondrial-targeted antioxidants represent a promising approach for prevention of cisplatin-induced nephropathy.” *Free Radic. Biol. Med.*, **52** (2), 497–506.

Mukhopadhyay, P., Rajesh, M., Pan, H., Patel, V., Mukhopadhyay, B., Bátkai, S., Gao, B., Haskó, G., Pacher, P. (2010) “Cannabinoid-2 receptor limits inflammation, oxidative/nitrosative stress, and cell death in nephropathy.” *Free Radic. Biol. Med.*, **48** (3), 457–467.

Needham, S.R., Brown, P.R., Duff, K., Bell, D. (2000) "Optimized stationary phases for the high-performance liquid chromatography-electrospray ionization mass spectrometric analysis of basic pharmaceuticals." *J. Chromatogr. A*, **869** (1-2), 159–170.

Neumar, R.W. (2000) "Molecular mechanisms of ischemic neuronal injury." *Ann. Emerg. Med.*, **36** (5), 483–506.

Nicholson, J.K., Lindon, J.C., Holmes, E. (1999) "'Metabonomics': understanding the metabolic responses of living systems to pathophysiological stimuli via multivariate statistical analysis of biological NMR spectroscopic data." *Xenobiotica*, **29** (11), 1181–1189.

Nichthauser, J., Stepnowski, P. (2009) "Retention mechanism of selected ionic liquids on a pentafluorophenylpropyl polar phase: investigation using RP-HPLC." *J. Chromatogr. Sci.*, **47** (3), 247–253.

Nordström, A., Want, E., Northen, T., Lehtiö, J., Siuzdak, G. (2008) "Multiple ionization mass spectrometry strategy used to reveal the complexity of metabolomics." *Anal. Chem.*, **80** (2), 421–429.

Okui, S., Yamamoto, H., Li, W., Gamachi, N., Fujita, Y., Kashiwamura, S.-I., Miura, D., Takai, S., Miyazaki, M., Urade, M., Okamura, H., Ueda, H. (2012) "Cisplatin-induced acute renal failure in mice is mediated by chymase-activated angiotensin-aldosterone system and interleukin-18." *Eur. J. Pharmacol.*, **685** (1-3), 149–155.

Ollins, G.E.J.C., Erhoeyen, M.A.E. V (2003) "Metabolite Profiling of Tomato (Lycopersicon esculentum) Using 1 H NMR Spectroscopy as a Tool To Detect Potential." *J. Agric. Food Chem.*, **51** (9), 2447–2456.

Pabla, N., Dong, Z. (2008) "Cisplatin nephrotoxicity: mechanisms and renoprotective strategies." *Kidney Int.*, **73** (9), 994–1007.

Pasetto, L.M., D'Andrea, M.R., Brandes, A.A., Rossi, E., Monfardini, S. (2006) "The development of platinum compounds and their possible combination." *Crit. Rev. Oncol. Hematol.*, **60** (1), 59–75.

Patti, G.J., Yanes, O., Siuzdak, G. (2012) “Metabolomics: the apogee of the omics trilogy.” *Nat. Rev.*, **13** (4), 263–269.

Perez, J.D., Colucci, J.A., Sakata, M.M., Cunha, T.S., Arita, D.Y., Casarini, D.E. (2011) “Proteomic approaches in understanding a detected relationship between chemotherapy-induced nephrotoxicity and cell respiration in HK-2 cells.” *Nephron. Physiol.*, **119** (1), 1–10.

Petyuk, V.A., Qian, W., Chin, M.H., Wang, H., Livesay, E.A., Monroe, M.E., Adkins, J.N., Jaitly, N., Anderson, D.J., Ii, D.G.C., Smith, D.J., Smith, R.D. (2007) “Spatial mapping of protein abundances in the mouse brain by voxelation integrated with high-throughput liquid chromatography – mass spectrometry.” *Genome Res.*, **17**, 328–336.

Phillis, J.W., Smith-Barbour, M., O’Regan, M.H. (1996) “Changes in extracellular amino acid neurotransmitters and purines during and following ischemias of different durations in the rat cerebral cortex.” *Neurochem. Int.*, **29** (2), 115–120.

Phillis, J.W., Smith-Barbour, M., O’Regan, M.H., Perkins, L.M. (1994) “Amino acid and purine release in rat brain following temporary middle cerebral artery occlusion.” *Neurochem. Res.*, **19** (9), 1125–1130.

Pinzani, P., Orlando, C., Pazzagli, M. (2006) “Laser-assisted microdissection for real-time PCR sample preparation.” *Mol. Aspects Med.*, **27** (2-3), 140–159.

Pohjanen, E., Thysell, E., Eklund, C., Silfver, A., Carlsson, I., Lundgren, K., Moritz, T., Svensson, M.B., Antti, H. (2007) “A Multivariate Screening Strategy for Investigating Metabolic Effects of Strenuous Physical Exercise in Human Serum research articles.” *J. Proteome Res.*, **6** (6), 2113–2120.

Portilla, D., Li, S., Nagothu, K.K., Megyesi, J., Kaissling, B., Schnackenberg, L., Safirstein, R.L., Beger, R.D. (2006) “Metabolomic study of cisplatin-induced nephrotoxicity.” *Kidney Int.*, **69** (12), 2194–2204.

Ramesh, G., Reeves, W.B. (2002) “TNF- α mediates chemokine and cytokine expression and renal injury in cisplatin nephrotoxicity.” *Jounal Clin. Investig.*, **110** (6), 835–842.

Razzaque, M.S., Koji, T., Kumatori, A., Taguchi, T. (1999) "Cisplatin-induced apoptosis in human proximal tubular epithelial cells is associated with the activation of the Fas/Fas ligand system." *Histochem. Cell Biol.*, **111** (5), 359–365.

Ries, F., Klastersky, J. (1986) "Nephrotoxicity Induced by Cancer Chemotherapy With Special Emphasis on Cisplatin Toxicity." *Am. J. Kidney Dis.*, **8** (5), 368–379.

Sarkar, S., Das, N. (2006) "Mannosylated liposomal flavonoid in combating age-related ischemia-reperfusion induced oxidative damage in rat brain." *Mech. Ageing Dev.*, **127** (4), 391–397.

Scholz, M., Gatzek, S., Sterling, A., Fiehn, O., Selbig, J. (2004) "Metabolite fingerprinting: detecting biological features by independent component analysis." *Bioinformatics*, **20** (15), 2447–2454.

Schreiber, V., Dantzer, F., Ame, J.-C., de Murcia, G. (2006) "Poly(ADP-ribose): novel functions for an old molecule." *Nat. Rev. Mol. Cell Biol.*, **7** (7), 517–528.

Schrier, R.W. (2002) "Cancer therapy and renal injury." *J. Clin. Invest.*, **110** (6), 743–745.

Schwartz, S. a, Reyzer, M.L., Caprioli, R.M. (2003) "Direct tissue analysis using matrix-assisted laser desorption/ionization mass spectrometry: practical aspects of sample preparation." *J. Mass Spectrom.*, **38** (7), 699–708.

Seeley, E.H., Caprioli, R.M. (2011) "MALDI imaging mass spectrometry of human tissue: method challenges and clinical perspectives." *Trends Biotechnol.*, **29** (3), 136–143.

Setoyama, D., Iwasa, K., Seta, H., Shimizu, H., Fujimura, Y., Miura, D., Wariishi, H., Nagai, C., Nakahara, K. (2013) "High-throughput metabolic profiling of diverse green Coffea arabica beans identified tryptophan as a universal discrimination factor for immature beans." *PLoS One*, **8** (8), e70098.

Sheikh-Hamad, D., Cacini, W., Buckley, A.R., Isaac, J., Truong, L.D., Tsao, C.C., Kishore, B.K. (2004) "Cellular and molecular studies on cisplatin-induced apoptotic cell death in rat kidney." *Arch. Toxicol.*, **78** (3), 147–155.

Siddik, Z.H. (2003) "Cisplatin: mode of cytotoxic action and molecular basis of resistance." *Oncogene*, **22** (47), 7265–7279.

Sims, N.R., Muyderman, H. (2010) “Mitochondria, oxidative metabolism and cell death in stroke.” *Biochim. Biophys. Acta*, **1802** (1), 80–91.

Smilde, A.K., Jansen, J.J., Hoefsloot, H.C.J., Lamers, R.-J. a N., van der Greef, J., Timmerman, M.E. (2005) “ANOVA-simultaneous component analysis (ASCA): a new tool for analyzing designed metabolomics data.” *Bioinformatics*, **21** (13), 3043–3048.

Stoeckli, M., Chaurand, P., Hallahan, D.E., Caprioli, R.M. (2001) “Imaging mass spectrometry: a new technology for the analysis of protein expression in mammalian tissues.” *Nat. Med.*, **7** (4), 493–496.

Sugimoto, M., Wong, D.T., Hirayama, A., Soga, T., Tomita, M. (2010) “Capillary electrophoresis mass spectrometry-based saliva metabolomics identified oral, breast and pancreatic cancer-specific profiles.” *Metabolomics*, **6** (1), 78–95.

Sugiura, Y., Konishi, Y., Zaima, N., Kajihara, S., Nakanishi, H., Taguchi, R., Setou, M. (2009) “Visualization of the cell-selective distribution of PUFA-containing phosphatidylcholines in mouse brain by imaging mass spectrometry.” *J. Lipid Res.*, **50** (9), 1776–1788.

Szabó, C., Zingarelli, B., O’Connor, M., Salzman, L.S. (1996) “DNA strand breakage, activation of poly (ADP-ribose) synthetase, and cellular energy depletion are involved in the cytotoxicity of macrophages and smooth muscle cells exposed to peroxynitrite.” *Proc. Natl. Acad. Sci. U. S. A.*, **93** (5), 1753–1758.

Tadagavadi, R.K., Reeves, W.B. (2010a) “Endogenous IL-10 attenuates cisplatin nephrotoxicity: role of dendritic cells.” *J. Immunol.*, **185** (8), 4904–4911.

Tadagavadi, R.K., Reeves, W.B. (2010b) “Renal dendritic cells ameliorate nephrotoxic acute kidney injury.” *J. Am. Soc. Nephrol.*, **21** (1), 53–63.

Takeda, M., Kobayashi, M., Shirato, I., Osaki, T., Endou, H. (1997) “Cisplatin-induced apoptosis of immortalized mouse proximal tubule cells is mediated by interleukin-1 beta converting enzyme (ICE) family of proteases but inhibited by overexpression of Bcl-2.” *Arch. Toxicol.*, **71** (10), 612–621.

Theobald, U., Mailinger, W., Reuss, M., Rizzi, M. (1993) "In Vivo Analysis of Glucose-Induced Fast Changes in Yeast Adenine Nucleotide Pool Applying a Rapid Sampling Technique." *Anal. Biochem.*, **214** (1), 31–37.

Theodoridis, G., Gika, H.G., Wilson, I.D. (2008) "LC-MS-based methodology for global metabolite profiling in metabonomics/metabolomics." *TrAC Trends Anal. Chem.*, **27** (3), 251–260.

Tolonen, A., Uusitalo, J. (2004) "Fast screening method for the analysis of total flavonoid content in plants and foodstuffs by high-performance liquid chromatography/electrospray ionization time-of-flight mass spectrometry with polarity switching." *Rapid Commun. Mass Spectrom.*, **18** (24), 3113–3122.

Tretter, L., Adam-Vizi, V. (2000) "Inhibition of Krebs cycle enzymes by hydrogen peroxide: A key role of [alpha]-ketoglutarate dehydrogenase in limiting NADH production under oxidative stress." *J. Neurosci.*, **20** (24), 8972–8979.

Vaidyanathan, S., Kell, D.B., Goodacre, R. (2002) "Flow-Ijnection Electrospray Ionization Mass Spectrometry of Crude Cell Extracts for High-Throughput Bacterial Identification." *J. Am. Soc. Mass Spectrom.*, **13** (2), 118–128.

Vickerman, J.C. (2011) "Molecular imaging and depth profiling by mass spectrometry--SIMS, MALDI or DESI?" *Analyst*, **136** (11), 2199–2217.

Virág, L., Salzman, a L., Szabó, C. (1998) "Poly(ADP-ribose) synthetase activation mediates mitochondrial injury during oxidant-induced cell death." *J. Immunol.*, **161** (7), 3753–3759.

Walch, A., Rauser, S., Deininger, S.O., Höfler, H. (2008) "MALDI imaging mass spectrometry for direct tissue analysis: a new frontier for molecular histology." *Histochem. Cell Biol.*, **130** (3), 421–434.

Wang, D., Lippard, S.J. (2005) "Cellular processing of platinum anticancer drugs." *Nat. Rev.*, **4** (4), 307–320.

Wang, W., Zhou, H., Lin, H., Roy, S., Shaler, T. a, Hill, L.R., Norton, S., Kumar, P., Anderle, M., Becker, C.H. (2003) "Quantification of proteins and metabolites by mass

spectrometry without isotopic labeling or spiked standards." *Anal. Chem.*, **75** (18), 4818–4826.

Wang, X., Martindale, J.L., Holbrook, N.J. (2000) "Requirement for ERK activation in cisplatin-induced apoptosis." *J. Biol. Chem.*, **275** (50), 39435–39443.

Watkins, S.M., German, J.B. (2002) "Toward the implementation of metabolomic assessments of human health and nutrition." *Curr. Opin. Biotechnol.*, **13** (5), 512–516.

Wei, Q., Dong, G., Franklin, J., Dong, Z. (2007) "The pathological role of Bax in cisplatin nephrotoxicity." *Kidney Int.*, **72** (1), 53–62.

Werner, E., Croixmarie, V., Umbdenstock, T., Ezan, E., Chaminade, P., Tabet, J.-C., Junot, C. (2008) "Mass spectrometry-based metabolomics: accelerating the characterization of discriminating signals by combining statistical correlations and ultrahigh resolution." *Anal. Chem.*, **80** (13), 4918–4932.

Widmann, C., Johnson, N.L., Gardner, a M., Smith, R.J., Johnson, G.L. (1997) "Potentiation of apoptosis by low dose stress stimuli in cells expressing activated MEK kinase 1." *Oncogene*, **15** (20), 2439–2447.

Xiao, J.F., Zhou, B., Ressom, H.W. (2012) "Metabolite identification and quantitation in LC-MS/MS-based metabolomics." *Trends Analyt. Chem.*, **32**, 1–14.

Yalcin, S., Müftüoğlu, S., Cetin, E., Sarer, B., Yildirim, B.A., Zeybek, D., Orhan, B. (2003) "Protection against cisplatin-induced nephrotoxicity by recombinant human erythropoietin." *Med. Oncol.*, **20** (2), 169–174.

Yang, S., Sadilek, M., Lidstrom, M.E. (2010) "Streamlined pentafluorophenylpropyl column liquid chromatography-tandem quadrupole mass spectrometry and global (13)C-labeled internal standards improve performance for quantitative metabolomics in bacteria." *J. Chromatogr. A*, **1217** (47), 7401–7410.

Yoshida, H., Mizukoshi, T., Hirayama, K., Miyano, H. (2007) "Comprehensive analytical method for the determination of hydrophilic metabolites by high-performance liquid chromatography and mass spectrometry." *J. Agric. Food Chem.*, **55** (3), 551–560.

Yoshida, H., Yamazaki, J., Ozawa, S., Mizukoshi, T., Miyano, H. (2009) "Advantage of LC-MS metabolomics methodology targeting hydrophilic compounds in the studies of fermented food samples." *J. Agric. Food Chem.*, **57** (4), 1119–1126.

Yousuf, S., Atif, F., Ahmad, M., Hoda, N., Ishrat, T., Khan, B., Islam, F. (2009) "Resveratrol exerts its neuroprotective effect by modulating mitochondrial dysfunctions and associated cell death during cerebral ischemia." *Brain Res.*, **1250**, 242–253.

Yukihira, D., Miura, D., Saito, K., Takahashi, K., Wariishi, H. (2010) "MALDI-MS-based high-throughput metabolite analysis for intracellular metabolic dynamics." *Anal. Chem.*, **82** (10), 4278–4282.

Zhang, N., Komine-Kobayashi, M., Tanaka, R., Liu, M., Mizuno, Y., Urabe, T. (2005) "Edaravone reduces early accumulation of oxidative products and sequential inflammatory responses after transient focal ischemia in mice brain." *Stroke*, **36** (10), 2220–2225.

Appendix

Table List of analyzed standard metabolites.

Molecular species	Formula	Exact mass	Detected polarity
(R)-*S*-Lactoylglutathione	C13H21N3O8S	379.10492	pos / neg
1-(5'-Phosphoribosyl)-5-amino-4-imidazolecarboxamide	C9H15N4O8P	338.06274	
1-6-Anhydro-β-d-glucose	C6H10O5	162.05281	
1-Aminocyclopropane-1-carboxylate	C4H7NO2	101.04767	pos
1-Kestose	C18H32O16	504.16901	pos
1-Methyladenine	C6H7N5	149.07014	pos / neg
1-Methyladenosine	C11H15N5O4	281.11239	pos / neg
1-Methylhistidine	C7H11N3O2	169.08512	pos / neg
1-Methylnicotinamide	C7H9N2O	137.07148	pos
1, 5-Anhydroglucitol (1,5-AG)	C6H12O5	164.06846	pos
1, 5-Diaminopentane	C5H14N2	102.11569	
10-Heptadecenoate (17:1n7)	C17H32O2	268.24021	pos / neg
10-Nonadecenoate (19:1n9)	C19H36O2	296.27151	
2-(4-Hydroxyphenyl)propionate	C9H10O3	166.06298	pos / neg
2-Aminobutyrate	C4H9NO2	103.06332	pos
2-Deoxyribose 5-phosphate	C5H11O7P	214.02369	neg
2-Hydroxy-4-methylpentanoate	C6H12O3	132.07863	
2-hydroxyisobutyrate	C4H8O3	104.04733	
2-Hydroxypalmitate	C16H31O3	271.22730	

Molecular species	Formula	Exact mass	Detected polarity
2-Hydroxyphenylacetate	C8H8O3	152.04733	
2-Hydroxystearate	C18H36O3	300.26642	
2-Isopropylmalate	C7H12O5	176.06846	
2-Oxoadipate	C6H8O5	160.03662	pos / neg
2-oxoglutarate	C5H6O5	146.02151	pos / neg
2'-Deoxycytidine	C9H13N3O4	227.09059	pos / neg
2'-Deoxyinosine	C10H12N4O4	252.08584	neg
2'-Deoxyuridine	C9H12N2O5	228.07407	neg
3-(2-Hydroxyethyl) indole	C10H11NO	161.08405	pos
3-(2-Hydroxyphenyl)propionic acid	C9H10O3	166.06298	
3-(3-Hydroxyphenyl)propionate	C9H10O3	166.06298	neg
3-(3, 4-Dihydroxyphenyl)-L-alanine (L-DOPA)	C9H11NO4	197.06825	pos / neg
3-Furoate	C5H4O3	112.01604	
3-Hydroxy-3-methylglutarate	C6H10O5	162.05281	
3-Hydroxyanthranilate	C7H7NO3	153.04258	pos / neg
3-Hydroxybutyrate (BHBA)	C4H8O3	104.04733	pos
3-Hydroxydecanoate	C10H20O3	188.14123	neg
3-Hydroxykynurenine	C10H12N2O4	224.07915	pos / neg
3-Hydroxyoctanoate	C8H16O3	160.10993	neg
3-Hydroxyphenylacetate	C8H8O3	152.04733	neg

Molecular species	Formula	Exact mass	Detected polarity
3-Indoxyl sulfate	C8H7NO5S	229.00448	
3-Methyl-2-oxovalerate	C6H10O3	130.06298	neg
3-Methyladipate	C7H12O4	160.07355	pos / neg
3-Methylhistidine	C7H11N3O2	169.08512	pos
3-Nitro-L-tyrosine	C9H10N2O5	226.05896	pos / neg
3-Phosphoglycerate	C3H7O7P	185.99293	pos / neg
3-Ureidopropionate	C4H8N2O3	132.05348	pos / neg
3, 4-Dihydroxyphenylacetate	C8H8O4	168.04225	neg
3'-Dephosphocoenzyme A	C21H35N7O13P2S	687.14886	
4-Acetamidobutanoate	C6H11NO3	145.07388	pos / neg
4-Aminobenzoate	C7H7NO2	137.04767	pos
4-Coumarate	C9H8O3	164.04733	neg
4-Guanidinobutanoate	C5H11N3O2	145.08512	
4-Hydroxy-3-methoxyphenylglycol sulfate	C9H12O7S	264.03036	
4-Hydroxyphenylacetate	C8H8O3	152.04733	neg
4-Hydroxyphenylpyruvate	C9H8O4	180.04225	neg
4-Imidazoleacetate	C5H6N2O2	126.04292	pos / neg
4-Methyl-2-oxopentanoate	C6H10O3	130.06298	neg
4-Octenedioate	C8H12O4	172.07355	

Molecular species	Formula	Exact mass	Detected polarity
5-Aminoimidazole-4-carboxamide ribonucleotide (AICAR)	C9H15N4O8P	338.06220	neg
5-Aminolevulinate	C5H9NO3	131.05823	
5-Aminovalerate	C5H11NO2	117.07897	pos / neg
5-Dodecenoate (12:1n7)	C12H22O2	198.16196	
5-Hydroxy-L-tryptophan	C11H12N2O3	220.08424	pos / neg
5-Hydroxyindoleacetate	C10H9NO3	191.05823	pos / neg
5-Hydroxylysine	C6H14N2O3	162.09989	pos / neg
5-Methoxyindoleacetate	C11H11NO3	205.07334	
5-Methyl-2'-deoxycytidine	C10H15N3O4	241.10624	pos / neg
5-Methylcytidine	C10H15N3O5	257.10116	pos / neg
5-Methylcytosine	C5H7N3O	125.05890	pos
5-Methyltetrahydrofolate (5MeTHF)	C20H25N7O6	459.18661	pos / neg
5-Methylthioadenosine (MTA)	C11H15N5O3S	297.08955	pos / neg
5-Oxoproline	C5H7NO3	129.04258	pos / neg
5, 6-Dihydrouracil	C4H6N2O2	114.04292	pos
6-Aminohexanoate	C6H13NO2	131.09462	pos
6-Hydroxynicotinate	C6H5NO3	139.02693	pos / neg
6-Oxolithocholate	C24H38O4	390.27699	pos / neg
6-Phosphogluconate	C6H13O10P	276.02462	
7-Dehydrocholesterol	C27H44O	384.33919	

Molecular species	Formula	Exact mass	Detected polarity
7-Methylguanine	C6H7N5O	165.06505	pos / neg
8-Oxodeguanosine monophosphate (8-oxo-dGMP)	C10H16N5O15P3	363.05745	
8-Oxoguanosine monophosphate (8-oxoGMP)	C10H16N5O16P3	379.05236	
Acetyl coenzyme A (Acetyl-CoA)	C23H38N7O17P3S	809.12575	pos / neg
Acetyl-*N*-formyl-5-methoxykynurenamine (AFMK)	C13H16N2O4	264.11045	
Acetylcarnitine	C9H18NO4	204.12357	pos
Acetylcholine	C7H16NO2	146.11755	
Acrolein	C3H4O	56.02621	
Adenine	C5H5N5	135.05449	pos
Adenosine	C10H13N5O4	267.09674	pos / neg
Adenosine 3'-monophosphate (3'-AMP)	C10H14N5O7P	347.06307	
Adenosine diphosphate (ADP)	C10H15N5O10P2	427.02940	pos / neg
Adenosine monophosphate (AMP)	C10H14N5O7P	347.06307	pos / neg
Adenosine triphosphate (ATP)	C10H16N5O13P3	506.99573	pos / neg
Adipate	C6H10O4	146.05790	pos / neg
Adrenate (22:4n6)	C22H36O2	332.27151	
Agmatine	C5H14N4	130.12183	pos
Alanine	C3H7NO2	89.04767	

Molecular species	Formula	Exact mass	Detected polarity
Aldosterone	C21H28O5	360.19365	pos / neg
Allantoin	C4H6N4O3	158.04398	pos / neg
Allocholate	C24H40O5	408.28755	
Anthranilate	C7H7NO2	137.04767	pos / neg
Arabinose	C5H10O5	150.05281	pos / neg
Arginine	C6H14N4O2	174.11166	pos / neg
Ascorbate (Vitamin C)	C6H8O6	176.03208	pos / neg
Asparagine	C4H8N2O3	132.05348	pos / neg
Aspartate	C4H7NO4	133.03750	pos / neg
Azelate (Nonanedioate)	C9H16O4	188.10485	neg
Benzoate	C7H6O2	122.03677	pos / neg
Betaine	C5H11NO2	117.07897	
Betaine aldehyde	C5H14NO2	120.10244	pos
Biliverdin	C33H34N4O6	582.24781	
Biopterin	C9H11N5O3	237.08618	pos / neg
Biotin	C10H16N2O3S	244.08816	pos / neg
Caffeate	C9H8O4	180.04225	pos / neg
Calcitriol	C27H44O3	416.32904	
Campesterol	C28H48O	400.37049	
Caprate (10:0)	C10H20O2	172.14632	pos
Caproate (6:0)	C6H12O2	116.08372	pos / neg

Molecular species	Formula	Exact mass	Detected polarity
Caprylate (8:0)	C8H16O2	144.11502	neg
Carnitine	C7H16NO3	162.11300	
Catechol	C6H6O2	110.03677	
Cellotetraose	C24H42O21	666.22182	
Cholate	C24H40O5	408.28755	pos / neg
Cholesterol	C27H46O	386.35484	
Choline	C5H14NO	104.10753	pos
Ciliatine (2-Aminoethylphosphonate)	C2H8NO3P	125.02417	pos / neg
cis-Aconitate	C6H6O6	174.01643	
Citrate	C6H8O7	192.02699	pos / neg
Citrulline	C6H13N3O3	175.09568	pos / neg
Cortexone	C21H30O3	330.21948	
Corticosterone	C21H30O4	346.21439	pos
Cortisol	C21H30O5	362.20930	
Cortisone	C21H30O5	362.20930	
Creatine	C4H9N3O2	131.06947	pos
Creatinine	C4H7N3O	113.05890	pos
Cyclic cytidine 3',5'-monophosphate (cCMP)	C9H14N3O8P	323.05130	
Cysteine	C3H7NO2S	121.01974	pos / neg
Cysteine-glutathione disulfide	C13H22N4O8S2	426.08789	pos / neg

Molecular species	Formula	Exact mass	Detected polarity
Cytidine	C9H13N3O5	243.08551	pos / neg
Cytidine diphosphate (CDP)	C9H15N3O11P2	403.01817	pos / neg
Cytidine diphosphocholine	C14H26N4O11P2	488.10731	pos / neg
Cytidine monophosphate	C9H14N3O8P	323.05184	pos / neg
Cytidine monophosphate-*N*-acetylneuraminate (CMP-Neu5Ac)	C20H31N4O16P	614.14724	pos
Cytidine triphosphate (CTP)	C9H16N3O14P3	482.98450	pos / neg
Cytosine	C4H5N3O	111.04325	pos
D-(+)-Glucono-1, 5-lactone	C6H10O6	178.04718	pos
D-Alanyl-D-alanine	C6H12N2O3	160.08478	pos / neg
D-Glucosamine 1-phosphate	C6H14NO8P	259.04569	
D-Glyceraldehyde	C3H6O3	90.03168	
D-Mannitol	C6H14O6	182.07902	pos / neg
D-Xylose	C5H10O5	150.05281	pos
Dehydroascorbate	C6H6O6	174.01643	
Deoxyadenosine	C10H13N5O3	251.10183	pos
Deoxyadenosine monophosphate (dAMP)	C10H14N5O6P	331.06762	pos / neg
Deoxyadenosine triphosphate (dATP)	C10H16N5O12P3	491.00082	
Deoxycholate	C24H40O4	392.29264	pos / neg

Molecular species	Formula	Exact mass	Detected polarity
Deoxycytidine diphosphate (dCDP)	C9H15N3O10P2	387.02325	pos / neg
Deoxycytidine monophosphate (dCMP)	C9H14N3O7P	307.05692	pos / neg
Deoxycytidine triphosphate (dCTP)	C9H16N3O13P3	466.98959	pos / neg
Deoxyguanosine	C10H13N5O4	267.09674	pos / neg
Deoxyguanosine diphosphate (dGDP)	C10H15N5O10P2	427.02940	pos / neg
Deoxyguanosine monophosphate (dGMP)	C10H14N5O7P	347.06307	pos / neg
Deoxyuridine diphosphate (dUDP)	C9H14N2O11P2	388.00673	neg
Deoxyuridine monophosphate (dUMP)	C9H13N2O8P	308.04040	pos / neg
Deoxyuridine triphosphate (dUTP)	C9H15N2O14P3	467.97306	pos / neg
Desmosterol	C27H44O	384.33919	
Diethanolamine	C4H11NO2	105.07897	pos
Dihydrobiopterin	C9H13N5O3	239.10183	
Dihydrofolate	C19H21N7O6	443.15478	pos
Dihydroxyacetone phosphate	C3H7O6P	169.99747	pos / neg
Dimethylarginine (ADMA)	C8H18N4O2	202.14296	
Dimethylglycine	C4H9NO2	103.06332	pos / neg
DL-Glyceraldehyde 3-phosphate (G3P)	C3H7O6P	169.99747	pos / neg
Docosahexaenoate (DHA; 22:6n3)	C22H32O2	328.24021	
Docosapentaenoate (n3 DPA; 22:5n3)	C22H34O2	330.25586	
Docosapentaenoic acid (22:5)	C22H32O2	328.24021	pos

Molecular species	Formula	Exact mass	Detected polarity
Docosatrienoate (22:3n3)	C22H38O2	334.28716	neg
Dopamine	C8H11NO2	153.07897	
Eicosadienoate (20:2)	C20H36O2	308.27151	
Eicosapentaenoate (EPA; 20:5n3)	C20H30O2	302.22456	
Ergocalciferol	C28H44O	396.33867	
Ergosterol	C28H44O	396.33920	
Ergothioneine	C9H15N3O2S	229.08849	
Erythrose	C4H8O4	120.04225	pos
Erythrose 4-phosphate (E4P)	C4H9O7P1	200.00858	
Estradiol	C18H24O2	272.17762	
Estrone	C18H22O2	270.16197	
Ethanolamine	C2H7NO	61.05276	
Ethylmalonate	C5H8O4	132.04225	neg
Farnesyl diphosphate	C15H28O7P2	382.13102	
Flavin adenine dinucleotide (FAD)	C27H33N9O15P2	785.15712	neg
Folate	C19H19N7O6	441.13967	pos / neg
Fructose	C6H12O6	180.06338	pos / neg
Fructose 6-phosphate	C6H13O9P	260.02971	pos / neg
Fructose bisphosphate (F1,6P)	C6H14O12P2	339.99604	neg
Fucose	C6H12O5	164.06847	
Fumarate	C4H4O4	116.01095	neg

Molecular species	Formula	Exact mass	Detected polarity
Gentisate	C7H6O4	154.02660	neg
Glucarate (Saccharate)	C6H10O8	210.03756	
Gluconate	C6H12O7	196.05829	pos / neg
Glucose	C6H12O6	180.06338	pos / neg
Glucose 1-phosphate	C6H13O9P	260.02917	pos / neg
Glucose 6-phosphate	C6H13O9P	260.02971	pos / neg
Glucuronate	C6H10O7	194.04264	
Glutamate	C5H9NO4	147.05315	pos / neg
Glutamine	C5H10N2O3	146.06914	pos / neg
Glutarate (Pentanedioate)	C5H8O4	132.04225	neg
Glutathione, oxidized (GSSG)	C20H32N6O12S2	612.15194	pos / neg
Glutathione, reduced (GSH)	C10H17N3O6S	307.08380	pos / neg
Glycerol	C3H8O3	92.04734	pos
Glycerol 3-phosphate	C3H9O6P	172.01367	pos / neg
Glycerophosphorylcholine (GPC)	C8H21NO6P	258.11064	pos
Glycine	C2H5NO2	75.03203	
Glycocholate	C26H43NO6	465.30902	
Glycodeoxycholate	C26H43NO5	449.31410	pos / neg
Guanidinoacetate	C3H7N3O2	117.05382	
Guanine	C5H5N5O	151.04941	
Guanosine	C10H13N5O5	283.09166	pos / neg

Molecular species	Formula	Exact mass	Detected polarity
Guanosine diphoshate (GDP)	C10H15N5O11P2	443.02432	pos / neg
Guanosine monophosphate (GMP)	C10H14N5O8P	363.05799	pos / neg
Guanosine triphosphate (GTP)	C10H16N5O14P3	522.99065	pos / neg
Guanosine-2', 3'-cyclic monophosphate (2', 3'-Cyclic GMP)	C10H12N5O7P	345.04743	pos / neg
Gulono-1, 4-lactone	C6H10O6	178.04773	pos / neg
Heme	C34H32FeN4O4	616.08734	pos
Heptanoate (7:0)	C7H14O2	130.09937	
Hexanoylglycine	C8H15NO3	173.10519	pos / neg
Histamine	C5H9N3	111.07964	pos
Histidine	C6H9N3O2	155.06947	pos / neg
Homoarginine	C7H16N4O2	188.12732	pos / neg
Homocitrulline	C7H15N3O3	189.11133	pos / neg
Homogentisate	C8H8O4	168.04225	neg
Homovanillate (HVA)	C9H10O4	182.05790	
Hydroxocobalamin	C62H90CoN13O15P	1346.57495	pos
Hyodeoxycholate	C24H40O4	392.29264	neg
Hypotaurine	C2H7NO2S	109.01975	pos / neg
Hypoxanthine	C5H4N4O	136.03851	neg
Imidazole lactate	C6H8N2O3	156.05349	
Indoleacetate	C10H9NO2	175.06332	

Molecular species	Formula	Exact mass	Detected polarity
Indolelactate	C11H11NO3	205.07389	pos / neg
Indolepropionate	C11H11NO2	189.07897	
Inosine	C10H12N4O5	268.08076	pos / neg
Inosine 3′: 5′-cyclic monophosphate (cIMP)	C10H11N4O7P	330.03599	pos / neg
Inosine diphosphate (IDP)	C10H14N4O11P2	428.01288	pos / neg
Inosine monophosphate (IMP)	C10H13N4O8P	348.04709	pos / neg
Isobar: Deoxycholate and Chenodeoxycholate	C12H11N7	253.10759	
Isocitrate	C6H8O7	192.02700	pos / neg
Isoleucine	C6H13NO2	131.09462	pos / neg
Isovalerate	C5H10O2	102.06807	
Itaconate (Methylenesuccinate)	C5H6O4	130.02660	neg
Kynurenate	C10H7NO3	189.04259	pos / neg
L-Adrenaline	C9H11NO4	197.06826	pos / neg
L-Arabitol	C5H12O5	152.06847	pos / neg
L-Cystathionine	C7H14N2O4S	222.06742	
L-Cysteate	C3H7NO5S	169.00449	pos / neg
L-Dihydroorotate	C5H6N2O4	158.03221	pos / neg
L-Homocystein	C4H9NO2S	135.03540	pos / neg
L-Homoserine	C4H9NO3	119.05824	

Molecular species	Formula	Exact mass	Detected polarity
L-Hydroxyproline	C5H9NO3	131.05824	pos / neg
L-Kynurenine	C10H12N2O3	208.08479	
L-Methionine *S*-oxide	C5H11NO3S	165.04596	pos / neg
L-Threonine phosphate	C4H10NO6P	199.02457	
Lactate	C3H6O3	90.03169	neg
Lanosterol	C30H50O	426.38614	
Lathosterol	C27H46O	386.35485	
Laurate (12:0)	C12H24O2	200.17762	neg
Leucine	C6H13NO2	131.09462	pos
Linoleate (18:2n6)	C18H32O2	280.24022	neg
Linolenate [α or γ; (18:3n3 or 6)]	C18H30O2	278.22457	
Lysine	C6H14N2O2	146.10552	pos / neg
Malate	C4H6O5	134.02152	pos / neg
Maleate	C4H4O4	116.01095	pos / neg
Maltohexaose	C36H62O31	990.32746	
Maltopentaose	C30H52O26	828.27465	pos / neg
Maltose	C12H22O11	342.11620	pos / neg
Maltotetraose	C24H42O21	666.22183	neg
Maltotriose	C18H32O16	504.16901	pos / neg
Mannose	C6H12O6	180.06338	pos / neg
Mannose-6-phosphate	C6H13O9P	260.02971	

Molecular species	Formula	Exact mass	Detected polarity
Margarate (17:0)	C17H34O2	270.25586	
Melatonin	C13H16N2O2	232.12063	pos / neg
Mercaptopyruvate	C3H4O3S	119.98811	
Mesaconate (Methylfumarate)	C5H6O4	130.02660	
Methionine	C5H11NO2S	149.05105	pos / neg
Methyl *cis*-10-heptadecenoate	C18H34O2	282.25533	
Methyl palmitate	C17H34O2	270.25586	pos
Methyl stearate	C19H38O2	298.28716	
Mevalonate	C6H12O4	148.07355	pos / neg
Monomethyl glutarate	C6H10O4	146.05790	pos
myo-Inositol	C6H12O6	180.06338	pos / neg
Myristate (14:0)	C14H28O2	228.20892	neg
Myristoleate (14:1n5)	C14H26O2	226.19327	neg
N-(2-Furoyl)glycine	C7H7NO4	169.03750	
N-Aacetylaspartate (NAA)	C6H9NO5	175.04807	pos / neg
N-Acetyl-5-hydroxytryptamine	C12H14N2O2	218.10498	
N-Acetyl-aspartyl-glutamate (NAAG)	C11H16N2O8	304.09065	pos / neg
N-Acetyl-D-mannosamine	C8H15NO6	221.08993	
N-acetyl-L-Alanine	C5H9NO3	131.05824	
N-Acetylasparagine	C6H10N2O4	174.06405	pos / neg
N-Acetylcysteine	C5H9NO3S	163.03031	pos / neg

Molecular species	Formula	Exact mass	Detected polarity
N-Acetylglucosamine (GlcNAc)	C8H15NO6	221.08939	pos / neg
N-Acetylglucosamine 6-sulfate	C8H15NO9S	301.04674	
N-Acetylglutamate (NAG)	C7H11NO5	189.06371	pos / neg
N-Acetylglutamine	C7H12N2O4	188.07970	
N-Acetylglycine	C4H7NO3	117.04259	neg
N-Acetylhistidine	C8H11N3O3	197.08003	pos / neg
N-Acetylisoleucine	C8H15NO3	173.10519	
N-Acetylleucine	C8H15NO3	173.10519	pos / neg
N-Acetylmethionine	C7H13NO3S	191.06161	
N-Acetylneuraminate	C11H19NO9	309.10597	pos / neg
N-Acetylornithine	C7H14N2O3	174.10043	pos / neg
N-Acetylphenylalanine	C11H13NO3	207.08954	pos / neg
N-Acetylproline	C7H11NO3	157.07389	pos / neg
N-Acetylputrescine	C6H14N2O	130.11061	
N-Acetylthreonine	C6H11NO4	161.06880	
N-Acetyltryptophan	C13H14N2O3	246.10043	pos / neg
N-Acetyltyrosine	C13H17NO4	251.11575	pos
N-Acetylvaline	C7H13NO3	159.08954	pos / neg
N-Carbamoylaspartate	C5H8N2O5	176.04331	
N-Formyl-L-methionine	C6H11NO3S	177.04596	
N-Formylanthranilate	C8H7NO3	165.04204	pos / neg

Molecular species	Formula	Exact mass	Detected polarity
N-Methylserotonin	C11H14N2O	190.11006	
N-α-Acetyl-L-arginine	C8H16N4O3	216.12223	pos / neg
N-*ω*-Methyltryptamine	C11H14N2	174.11515	
*N*2-Acetyl-L-lysine	C8H16N2O3	188.11608	
*N*2,*N*2-Dimethylguanosine	C12H17N5O5	311.12296	
*N*4-Acetylcytidine	C11H15N3O6	285.09608	
*N*6-(L-1, 3-Dicarboxypropyl)-L-lysine (L-Saccharopine)	C11H20N2O6	276.13212	pos / neg
*N*6-Acetyl-L-lysine	C8H16N2O3	188.11608	
*N*6-Ccarbamoylthreonyladenosine	C15H21N7O7	411.15023	
*N*8-Acetylspermidine	C9H21N3O	187.16845	
N^{G},$N^{G'}$-Dimethyl-L-arginine di(*p*-hydroxyazobenzene-*p*′-sulfonate) salt (SDMA)			pos / neg
Nicotinamide	C6H6N2O	122.04801	pos
Nicotinamide adenine dinucleotide (NAD^+)	C21H28N7O14P2	664.11693	pos
Nicotinamide adenine dinucleotide phosphate ($NADP^+$)	C21H30N7O17P3	745.09109	pos / neg
Nicotinamide ribonucleotide (NMN)	C11H15N2O8P	334.05659	
Nicotinamide-*N*-oxide	C6H6N2O2	138.04292	pos

Molecular species	Formula	Exact mass	Detected polarity
Nicotinate	C6H5NO2	123.03203	pos / neg
Nicotinate mononucleotide	C11H16NO9P	337.05572	
Nicotinurate	C8H8N2O3	180.05349	pos / neg
Nonadecanoate (19:0)	C19H38O2	298.28716	
Norepinephrine	C8H11NO3	169.07334	neg
Norleucine	C6H13NO2	131.09462	
O-Acetyl-L-Homoserine	C6H11NO4	161.06880	pos
O-Acetylserine	C5H9NO4	147.05315	pos
Oleamide	C18H35NO	281.27185	
Oleate (18:1n9)	C18H34O2	282.25586	
Ophthalmate	C11H19N3O6	289.12737	pos / neg
Ornithine	C5H12N2O2	132.08987	pos / neg
Orotate	C5H4N2O4	156.01710	
Oxaloacetate	C4H4O5	132.00587	
p-Hydroxybenzaldehyde	C7H6O2	122.03678	
Palmitate (16:0)	C16H32O2	256.24022	pos
Palmitoleate (16:1n7)	C16H30O2	254.22457	
Pantoprazole Sulfide *N*-Oxide	C16H15F2N3O4S	383.07458	pos / neg
Pantothenate	C9H17NO5	219.11066	
Pantothenol	C9H19NO4	205.13140	
Pelargonate (9:0)	C9H18O2	158.13067	

Molecular species	Formula	Exact mass	Detected polarity
Pentadecanoate (15:0)	C15H30O2	242.22457	neg
Phenethylamine	C8H11N	121.08914	
Phenyl-β-glucopyranoside	C12H16O6	256.09468	
Phenylacetylglycine	C10H11NO3	193.07389	pos / neg
Phenylalanine	C9H11NO2	165.07897	pos / neg
Phenyllactate (PLA)	C9H10O3	166.06299	neg
Phosphate	H3PO4	97.97689	pos / neg
Phosphocreatine	C4H10N3O5P	211.03526	pos / neg
Phosphoenolpyruvate (PEP)	C3H5O6P	167.98237	pos / neg
Phosphoethanolamine	C2H8NO4P	141.01909	pos / neg
Pimelate (Heptanedioate)	C7H12O4	160.07355	pos / neg
Pipecolate	C6H11NO2	129.07897	pos / neg
Pregnenolone	C21H32O2	316.24022	pos
Progesterone	C21H30O2	314.22457	
Proline	C5H9NO2	115.06332	pos / neg
Pseudouridine	C9H12N2O6	244.06953	pos / neg
Purine	C5H4N4	120.04359	pos / neg
Putrescine	C4H12N2	88.10004	
Pyridoxal	C8H9NO3	167.05824	pos / neg
Pyridoxal 5-phosphate	C8H10NO6P	247.02457	pos / neg
Pyridoxamine	C8H12N2O2	168.08987	pos / neg

Molecular species	Formula	Exact mass	Detected polarity
Pyridoxate	C8H9NO4	183.05315	
Pyridoxine	C8H11NO3	169.07389	pos / neg
Pyrophosphate (PPi)	P2H4O7	177.94323	neg
Pyruvate	C3H4O3	88.01604	
Quinaldate	C10H7NO2	173.04767	pos
Quinolinate	C7H5NO4	167.02185	pos / neg
Raffinose	C18H32O16	504.16901	pos / neg
Retinal	C20H28O	284.21402	pos
Retinol	C20H30O	286.22968	
Ribitol (Adonitol)	C5H12O5	152.06847	
Riboflavin (Vitamin B2)	C17H20N4O6	376.13827	pos / neg
Ribose	C5H10O5	150.05282	pos
Ribose 5-phosphate	C5H11O8P	230.01915	pos / neg
S-Adenosyl-L-methionine (SAM)	C15H22N6O5S	398.13723	
S-Adenosylhomocysteine (SAH)	C14H20N6O5S	384.12158	
S-Methylglutathione	C11H19N3O6S	321.09945	pos / neg
Sarcosine (*N*-Methylglycine)	C3H7NO2	89.04767	
scyllo-Inositol	C6H12O6	180.06338	
Sebacate (Decanedioate)	C10H18O4	202.12050	pos / neg
Sedoheptulose	C7H14O7	210.07394	pos
Serine	C3H7NO3	105.04259	pos / neg

Molecular species	Formula	Exact mass	Detected polarity
Serotonin (5HT)	C10H12N2O	176.09496	
Sorbitol (Glucitol)	C6H14O6	182.07903	
Spermidine	C7H19N3	145.15789	pos
Spermine	C10H26N4	202.21573	pos
Sphingosine	C18H37NO2	299.28241	pos
Squalene	C30H50	410.39123	
Stachydrine	C7H13NO2	143.09462	
Stachyose	C24H42O21	666.22183	pos / neg
Stearate (18:0)	C18H36O2	284.27151	neg
Stigmasterol	C29H48O	412.37049	
Succinate	C4H6O4	118.02660	pos / neg
Succinyl coenzyme A (Succinyl-CoA)	C25H40N7O19P3S	867.13071	pos / neg
Sucrose	C12H22O11	342.11620	pos / neg
Taurine	C2H7NO3S	125.01466	
Taurochenodeoxycholate	C26H45NO6S	499.29674	
Taurocholate	C26H45NO7S	515.29165	neg
Taurocyamine	C3H9N3O3S	167.03646	pos / neg
Taurodeoxycholate	C26H45NO6S	499.29674	neg
Taurolithocholate	C26H45NO5S	483.30182	
Testosterone	C19H28O2	288.20892	pos
Tetradecanedioate	C14H26O4	258.18310	

Molecular species	Formula	Exact mass	Detected polarity
Tetrahydrofolate	C19H23N7O6	445.17043	pos / neg
Thiamin (Vitamin B1)	C12H17N4OS	265.11230	pos / neg
Thiamine diphosphate (TDP)	C12H19N4O7P2S	425.04496	pos / neg
Threitol	C4H10O4	122.05790	
Threonate	C4H8O5	136.03717	
Threonine	C4H9NO3	119.05824	pos / neg
Thymidine	C10H14N2O5	242.09026	pos / neg
Thymidine diphosphate (dTDP)	C10H16N2O11P2	402.02292	pos / neg
Thymidine triphosphate (dTTP)	C10H17N2O14P3	481.98926	pos / neg
Thymine	C5H6N2O2	126.04292	
Tigloylglycine	C7H11NO3	157.07389	pos / neg
trans-4-Hydroxyproline	C5H9NO3	131.05824	pos / neg
trans-Cinnamate	C9H8O2	148.05243	
Tryptamine	C10H12N2	160.10004	
Tryptophan	C11H12N2O2	204.08987	pos / neg
Tyramine	C8H11NO	137.08406	pos
Tyrosine	C9H11NO3	181.07389	pos / neg
Uracil	C4H4N2O2	112.02727	pos / neg
Urate	C5H4N4O3	168.02834	
Urea	CH4N2O	60.03236	
Uridine	C9H12N2O6	244.06953	pos

Molecular species	Formula	Exact mass	Detected polarity
Uridine diphosphate (UDP)	C9H14N2O12P2	404.00219	pos / neg
Uridine diphosphate galactose (UDP-galactose)	C15H24N2O17P2	566.05447	neg
Uridine diphosphate glucose (UDP-glucose)	C15H24N2O17P2	566.05501	neg
Uridine diphosphate *N*-acetylglucosamine (UDP-GlcNAc)	C17H27N3O17P2	607.08102	neg
Uridine monophosphate (UMP)	C9H13N2O9P	324.03586	pos / neg
Uridine triphosphate (UTP)	C9H15N2O15P3	483.96852	neg
Uridine-2', 3'-cyclic monophosphate (2', 3'-Cyclic UMP)	C9H11N2O8P	306.02530	
Urocanate	C6H6N2O2	138.04292	pos
Ursodeoxycholate (Ursodiol)	C24H40O4	392.29264	
Valerate	C5H10O2	102.06807	
Valine	C5H11NO2	117.07897	pos
Vitamin B12	C63H88CoN14O14P	1354.56738	pos
Vitamin K1	C31H46O2	450.34923	
Vitamin K2	C31H40O2	444.30228	
Xanthine	C5H4N4O2	152.03342	pos / neg
Xanthurenate	C10H7NO4	205.03750	pos / neg
Xylitol	C5H12O5	152.06847	pos / neg

Molecular species	Formula	Exact mass	Detected polarity
Xylonate	C5H10O6	166.04773	pos / neg
Xylose	C5H10O5	150.05282	
Xylulose	C5H10O5	150.05282	
Xylulose 5-phosphate (X5P)	C5H11O8P	230.01915	
α-Hydroxyisovalerate	C5H10O3	118.06299	
α-Tocopherol	C29H50O2	430.38106	
β-Alanine	C3H7NO2	89.04767	pos
β-Aminoisobutyrate	C4H9NO2	103.06332	
β-Hydroxyisovalerate	C5H10O3	118.06299	
β-Hydroxypyruvate	C3H4O4	104.01095	
β-Sitosterol	C29H50O	414.38614	
γ-Aminobutyrate (GABA)	C4H9NO2	103.06332	
γ-Butyrolactone	C4H6O2	86.03678	pos
γ-Glutamylcysteine	C8H14N2O5S	250.06179	
γ-Linolenic acid	C18H30O2	278.22457	neg

Vita

VITA

Miho Irie was born in Saga, Japan on September 17, 1985. She received her Bachelor of Agriculture degree from Kagoshima University, Japan in March, 2009. She immediately continued her study in master degree and received her Master of Science degree from Kyushu University in March, 2011.

In April, 2011, the author joined the Phd program at Graduate School of Bioresource and Bioenvironmental Science, Kyushu University.